Revitalizing CMUTs

Kawasaki, S.

DOI
10.4233/uuid:0d57b4ce-42c2-423e-a4e0-b62b6a842a54

Publication date
2024

Document Version
Final published version

Citation (APA)
Kawasaki, S. (2024). *Revitalizing CMUTs*. [Dissertation (TU Delft), Delft University of Technology]. https://doi.org/10.4233/uuid:0d57b4ce-42c2-423e-a4e0-b62b6a842a54

REVITALIZING CMUTS

REVITALIZING CMUTS

Dissertation

for the purpose of obtaining the degree of doctor
at Delft University of Technology
by the authority of the Rector Magnificus prof.dr.ir. T.H.J.J. van der Hagen
chair of the Board for Doctorates
to be defended publicly on
Wednesday 28 February at 15:00 o'clock

by

Shinnosuke KAWASAKI

Master of Science in Electrical Engineering,
Delft University of Technology, Delft, the Netherlands,
born in Kanagawa, Japan.

This dissertation has been approved by the promotors.

Composition of the doctoral committee:

Rector Magnificus,	Chairperson
Prof. dr. ir. R. Dekker	Delft University of Technology, promotor
Dr. V. Giagka	Delft University of Technology, copromotor

Independent members:

Prof. dr. ir. P. M. Sarro	Delft University of Technology
Prof. dr. ir. N. de Jong	Delft University of Technology
Prof. dr. A. S. Savoia	Università Roma Tre
Dr. ir. M. A. P. Pertijs	Delft University of Technology
Prof. dr. P. J. French	Delft University of Technology, reserve member

Other member:

Dr. H. Huiberts	Philips Research

This thesis work was supported by ULIMPIA, a labelled PENTA project endorsed by EUREKA under PENTA cluster number E!9911.

Keywords: Ultrasound, MEMS, CMUT, ultrasound power transfer, pre-charged CMUTs, microfluidic particle separation, ultrasound neurostimulation

Printed by: Ipskamp printing

Front & Back: Satomi Minoshima.

ISBN 978-94-6473-390-7

An electronic version of this dissertation is available at
http://repository.tudelft.nl/.

It's the best thing in life to take the one thing you love most
and have it work out that you can make a living that way

Alex Honnold, 'Free Solo'

CONTENTS

SUMMARY

CMUTs (Capacitive Micromachined Ultrasonic Transducers) are causing a technological revolution. Research over the last decade showed that CMUTs can sufficiently replace traditional ultrasound technology based on the bulk PZT, along with other benefits such as lower assembly cost, broader bandwidth and monolithic integration capability with ASICs. Furthermore, devices can be fabricated from with non-toxic materials and eliminate the environmental impact that is associated to PZT. As a result, in recent years we are seeing low-cost consumer level ultrasound imaging technology becoming available for point of care diagnostics devices from startup companies. However, surprisingly, CMUT technology adoption is still lagging behind what we would expect. Thus, in this thesis three novel CMUT applications are investigated to show-case the untapped potentials of CMUTs which should lead to further traction for the CMUT field. The three applications that were investigated in this work were, a) Power reception and data transfer for implantable devices (Chapter 2, 3 and 4), b) Ultrasound nerve stimulation (Chapter 5), and c) particle separation for lab-on-a-chip devices (Chapter 6).

In Chapter 1, the growing market of portable ultrasound technology is introduced and different transducer types are compared to give the reader an overview of the MEMS ultrasound field. In Chapter 2, a semi-analytical reduced order model of a collapse-mode CMUT is extended with a built-in charge layer. This work shows that the charging can induce a dipole within the charge trapping layer which is strong enough to keep the CMUT in collapse. In Chapter 3, the power reception characteristics are studied, which shows that in an optimally loaded condition, the CMUT can harvest 42 % of the energy that impinges on the surface of the CMUT. This efficiency is comparable to conventional PZT technology. In Chapter 4, a communication scheme is presented that can transfer information from the implantable device to the external ultrasound transducer based on backscattering. In Chapter 6, the application of CMUTs for particle separation in Lab-on-a-chip devices is explored.

By reading this work it is my wish that the reader could understand the hugely prosperous future of CMUTs.

SAMENVATTING

CMUTs (Capacitive Micromachined Ultrasound Transducers) staan aan de basis van een technologische revolutie in medische diagnostiek and monitoring. Onderzoek gedurende de laatste tien jaar heeft erin geresulteerd dat de werking van CMUTs nu zo goed is dat ze zich kan meten met traditionele PZT gebaseerde technologie. Daarnaast hebben ze nog een aantal andere voordelen zoals lagere assemblagekosten, grotere bandbreedte en de mogelijkheid tot monolithische integratie met ASICs. Bovendien bevatten ze geen giftige materialen waardoor ze minder schadelijk zijn voor het milieu dan PZT-transducers. Als gevolg hiervan zien we recentelijk de ontwikkeling van goedkope ultrasound imaging apparatuur voor point-of-care diagnostiek. Verassend genoeg verloopt de introductie en adoptie van CMUT-technologie desondanks langzamer dan verwacht. Daarom worden in dit proefschrift drie CMUT-applicaties uitgewerkt die het potentieel van de CMUT-technologie illustreren in de hoop een brede acceptatie van CMUT technologie te versnellen: a) draadloze vermogens- and dataoverdracht voor implanteerbare devices (Hoofdstukken 2,3, en 4), b) ultrasound zenuwstimulatie (Hoofdstuk 5) en deeltjesscheiding in lab-on-a-chip devices (Hoofdstuk 6) In Hoofdstuk 1 wordt de groeiende markt voor draagbare ultrasound technologie geïntroduceerd en worden de verschillende transducer types vergeleken om een overzicht te geven van de ontwikkelingen op het gebied van MEMS-ultrasound. In Hoofdstuk 2 wordt een semi-analytisch “reduced order” model van een “collapse-mode” CMUT uitgebreid met een ingebouwde ladingslaag. Aangetoond wordt dat het mogelijk is een dipool laag te induceren die sterk genoeg is om de CMUT in collapse te houden. In Hoofdstuk 3 worden de eigenschappen van de CMUT voor vermogensoverdracht bestudeerd. Bij een optimale impedantie aanpassing is een efficiëntie van 42 %aangetoond. Dit is vergelijkbaar met PZT-technologie. In Hoofdstuk 4 wordt een communicatietechniek voor implanteerbare devices gepresenteerd gebaseerd op de energie die door een CMUT wordt gereflecteerd. In Hoofdstuk 5 wordt zenuwstimulatie met behulp van een CMUT-ultrasound cuff-device. In Hoofdstuk 6, tenslotte, wordt de toepassing van CMUTs voor deeltjesscheiding in lab-on-a-chip devices onderzocht.

PREFACE

The first capacitive micromachined ultrasonic transducer (CMUT) was developed three decades ago and it is fascinating to think that I am about the same age as the technology that I am currently studying and yet there is still so much more to learn about. There is no way to express how privileged my experience at Philips research was to work with one of the most mature CMUT technologies in the word. But working on this technology for the last four years I came to realize that the hype for CMUTs within Philips Research is becoming a thing of the past, and I notice that the valley of death is silently creeping towards us. I plan to change that with this thesis. Giving CMUTs another boost of energy by looking for innovative applications not only in the field of ultrasound imaging but for a broader market: Ultrasound neuromodulation, implantable technology and microfluidic devices. Each of these innovative applications have huge potential for CMUTs because CMUTs can be miniaturized, mass produced and biocompatible. Thus after reading this thesis, I hope you will be convinced that CMUTs are the future and that it is possible to revitalize CMUTs!

Shinnosuke Kawasaki
Eindhoven, March 2022

1

INTRODUCTION

MEMS (Microelectromechanicalsystem) ultrasound is undergoing a technological revolution. Research over that last decade shows that MEMS ultrasound technology can replace traditional ultrasound technology based on the conventional bulk PZT technology along with benefits such as lower assembly cost, broader bandwidth and thinner devices that can be monolithically integrated with ASICs. Furthermore, devices could be designed with non-toxic materials and edecrease the environmental impact. As a result, in recent years we are seeing low-cost consumer level ultrasound imaging technology becoming available for point of care diagnostics devices from startup companies. However, to our surprise, CMUT technology adoption is still lagging behind what we would expect. Thus, in this thesis several novel collapse-mode CMUT applications are presented to show-case the untapped potentials of a CMUT which should lead to further traction of the CMUT.

1

1.1. ULTRASOUND AND ITS EMERGING APPLICATIONS

Since the first introduction of ultrasound imaging of the brain by Dr. Karl Dussik in 1942, ultrasound has been used to visualize tissue regions within our body that are otherwise invisible to our naked eye [1]. The hardware that enabled this breakthrough was lead zirconate titanate (PZT), which was first discovered in the 1910s which had the unique property of directly converting mechanical pressure to electrical current and vice versa. The performance of these materials has been improved over the years, resulting in superb electromechanical performance that make them the gold standard for ultrasound imaging till this day. Concurrently, the avialabilty of higher computing power in the 1960s drastically improved the image quality over the following 20 to 30 years, resulting in different imaging modalities such as pulsed wave doppler imaging [2], tissue harmonic imaging [3] and elastography [4].

Currently, PZT based technology is mainly targeting the high-end professional ultrasound market where better image qualities are essential for an accurate diagnosis. However, in recent years there has been an emerging low-end ultrasound market which accommodates newer customer/patient demands such as handheld ultrasound systems connected to a smart phone, which can allow on-site visualization in resource limited settings [5], [6], or an ultrasound patch device that can continuously monitor the status of a specific visceral organ [7], [8]. For the handheld ultrasound market, there is a forecast by Yole that this type of medical equipment will increase in numbers of shipment by 17.4 % CAGR from 2019 to 2025 (see Fig. 1.1). While the other ultrasound imaging equipment also shown in this figure, will grow with a rather moderate increase of less than 7 %.

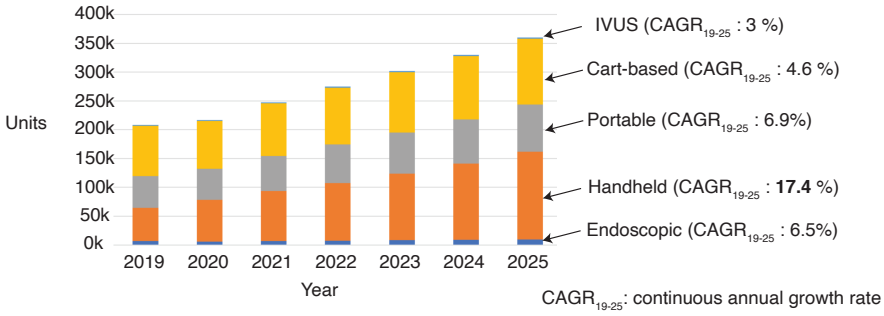

Figure 1.1: Medical imaging equipment shipments 2019-2025. (Yole, Medical Wearables: Market Technology Analysis 2019).

These newer low-end ultrasound markets call for different requirements compared to the conventional high-end ultrasound market. For example, connectivity to the inter-

net, portability, miniaturization, lower price, biocompatibility and manufacturing scalability to name a few. Unfortunately, the current manufacturing process based on PZT ultrasound transducer is not well equipped to tackle these emerging issues. Some limitations being the inherent labor cost that is associated to the manual assembly of PZT transducers, or the use of toxic metal (lead) which limits the in-body use [9], or the fact that lead has a high environmental footprint [10].

Alternatively, Micromachined ultrasonic transducers (MUTs) are currently under development. MUTs have a suspended membrane over a vacuum gap and through the vibration of this membrane, ultrasound can be transmitted or received from the medium on top of the membrane. Due to this thin membrane structure, MUTs have a broader bandwidth compared to conventional PZT transducers. Furthermore, they have a lower acoustic impedance which makes them preferable for use with soft body tissues that also have a similar acoustic impedance and thus requires no need for a backing layer. MUTs are fabricated through standard IC based fabrication processes which makes them CMOS compatible and thus, better integration with peripheral electronics at a lower cost.

Depending on the actuation mechanism, MUTs can be categorized either as CMUTs (Capacitive Micromachined Ultrasound Transducers) or PMUTs (Piezoelectric Micromachined Ultrasound Transducers). CMUTs are actuated electrostatically with one electrode embedded in the vibrating membrane and an opposing electrode beneath the vacuum gap. In contrast, PMUTs are actuated with a piezoelectric material deposited on the vibrating membrane which could be PZT, aluminum nitride (AlN), scandium doped aluminum nitride (ScAlN) or polymer based piezoelectric layers. Comparing these two technologies, CMUT technology has sufficiently matured resulting in several consumer products [11], while PMUTs require additional research efforts for full maturity [12].

1.1.1. COLLAPSE-MODE CMUTS

A CMUT has a top electrode and a bottom electrode separated via a vacuum gap and a dielectric insulation layer. To increase the transmit and receive sensitivity of these CMUTs, it is essential to have a high electric field between the top and bottom electrode (several MV/cm), which is accomplished by applying a bias voltage (several tens of volts to 200 V), across a several hundred nanometer gap to bring the top membrane closer to the bottom membrane. When the two membranes are not touching, the CMUT is in non-collapse mode operation, and when the two membrane are in contact it is in collapse-mode operation. In Philips Research, where this thesis took place, the main focus was on the development of collapse-mode CMUTs [13].

Table 1.1: Comparison between PZT transducers and Collapse-mode CMUTs.

	PZT transducers	Collapse-mode CMUTs
DC bias	+) Not required	-) From several tens of volts up to 200 V
Frequency Range	+) 1 kHz to 50 MHz	+) Sub MHz to 50 MHz
Design Parameters	PZT material, thickness, backing and coating material	Dielectric layer material Diameter of the membrane Gap height Thickness of the membrane Layer stress
Electronic Integration	-) Costly	+) Cost effective monolithic integration with ASIC
Manufacturing	+) Mechanical dicing and assembly	++) Standard IC based fabrication
Miniaturization	-) Challenging <40 µm element size	+) Element diamter 10 µm to 400 µm
Design	-) Limited in element shape. More flexible for curved transducers.	+) Arbitrary element shapes. Curve could be done to a certain extent by thinning down the wafer or by using more advanced techniques like F2R*.
Maturity	++) >50 years	+) ≈ 10 years

Table 1.1 summarizes the differences between a collapse-mode CMUT and a PZT transducer. As shown in the table, a CMUT requires a DC bias voltage whereas the PZT does not. The overall addressable frequency range is comparable between the PZT transducers and CMUTs but the individual device has a broader bandwidth for a CMUT because of its low acoustic impedance membrane structure. The exact operation frequency of a CMUT is typically controlled by changing the geometry and the process parameter (i.e. membrane diameter, layer stack and gap height) which provides a large design freedom. Meanwhile, for a PZT, the frequency range is controlled by thinning the PZT to different thicknesses, comparably cheaper to do and simple. Yet for devices that require higher frequency the thickness of the PZT layer becomes several tens of micron thinning and assembly becomes increasingly difficult. On the other hand, for CMUTs, higher frequency devices are easier to fabricate because the sacrificial wet etch process that is needed to lift off the membrane becomes easier for smaller diameter membranes. The electrical integration of a CMUT can be done by monolithically processing the CMUT on top of the ASIC or by wirebonding the electrical pads at the edge of the die to another substrate. In comparison, PZT transducers require a complicated assembly step, which requires an electrical contact at each side of the PZT and by gluing it to an additional substrate with a proper backing layer and an acoustic lens on the front. If the CMUT is mass produced, the assembly costs begins to outweigh the initial development cost of making a CMUT, and thus making the CMUT becomes a cost effective solution compared to a PZT device for high volume production. To summarize, CMUTs have a large

design freedom, they can be produced in large volume and at low cost, they can allow for a high level of integration, can be easily miniaturized to work at high frequency, are lead free and have a higher biocompatibility compared to PZT.

1.1.2. OBJECTIVE OF THIS THESIS

According to the previous section, the collapse-mode CMUT has many more attractive qualities compared to the PZT. Nonetheless, the technology adoption of CMUTs has not advanced as much as we would expect. The presence of PZT technology as the gold standard for ultrasound imaging may be preventing the newer technology to be adopted. The objective of this thesis is to show several advanced applications of CMUTs going beyond the traditional imaging domain that can only be accomplished with CMUTs. Thus, hoping that this will generate momentum, revitalizing CMUTs.

The three types of CMUT used in this work is shown in Table. 1.2. The three CMUTs can be categorized based on their operation frequency as low frequency (1-5 MHz), mid-frequency (3-8 MHz) up to high frequency (10-50 MHz). As the frequency goes higher, the membrane diameter becomes smaller.

Table 1.2: Three types of CMUT used for this work.

	(a)	(b)	(c)
	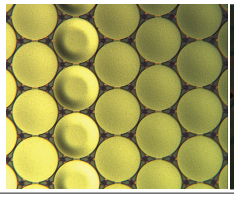	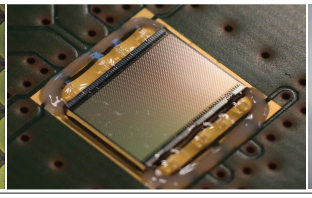	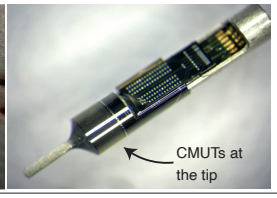
Frequency	low frequency (1 to 5 MHz)	mid frequency (3 to 10 MHz)	high frequency (10 to 50 MHz)
Membrane diameter	315 µm	135 µm	40 µm
Main stream application	General Ultrasound imaging	High resolution Ultrasound imaging	IVUS catheter
Novel Application proposed in this work	Acoustic particle sorting for lab-on-a-chip devices (Chapter 6)	zero-bias CMUT (Chapter 2) Ultrasound energy harvester/ Ultrasound backscatter communication for implantable devices (Chapter 3, 4)	Ultrasound nervestimualtion (Chapter 5)
Unique property of each CMUT exploited in this work	Collapse region leading to high coupling of the utlrasound to the substrate	Al_2O_3layer used for the insulation dielectric layer	Rollable format due to the F2R technology platform

Each CMUT shown in Table 1.2 has a main stream application which was the reason for them to be fabricated in the first place; general ultrasound imaging for low frequency CMUTs, high resolution imaging for mid frequency CMUTs and intravascular ultrasound imaging (IVUS) for high frequency CMUTs. In this work, we repurpose these technolo-

gies for novel applications. Therefore, the performance of the devices are not fully optimized for the novel application that is proposed in this work. As a result this work must be thought of as a collection of feasibility studies. However, due to the unique modular design aspect of CMUTs and its vast design freedom, it is possible to transfer the knowledge that is gained in one type of CMUT to the other with minimal adaption.

The first novel applications of CMUTs investigated in this work (chapter 2,3 and 4) was to use CMUTs as ultrasound energy harvesters for implantable devices. This exploits the fact that CMUTs can be designed with arbitrary dielectric layers in between the top and bottom electrode. In this work, Al_2O_3 was found to have unique charging capabilities (typically unwanted for MEMS devices) that could be used to substitute the external bias voltage that is required for CMUTs. For space limited applications of CMUT such as implantable devices or portable ultrasound, this technology will be extremely useful.

The second novel application of CMUTs investigated in this work was to use CMUTs for ultrasound nervestimulation. Ultrasound is recently attracting attention in the neuromodulation community as a technique to complement electrical stimulation or magnetic transcranial stimulation for its more targeted stimulation due to the short wavelength of ultrasound (i.e. 1 mm for 1.5 MHz ultrasound). In this work, using the unique rollable property of CMUTs developed for IVUS catheters, we investigated the possibility of using an array of CMUTs wrapped around the nerve to create spatially specific neurommodulation within the nerve.

The third novel application of CMUTs investigated in this work was to use CMUTs for acoustic particle sorting for silicon based lab-on-a-chip devices. Acoustic particle sorting is a biocompatiable, label-free method to sort particles for lab-on-a-chip applications. In the past, while working with CMUTs, it was found that ultrasound energy not only couples into the medium above the CMUT, but also into the silicon substrate itself, most likely through the large collapsed region at the center of the CMUT. From this insight, we tested if CMUTs operated in air can couple more ultrasound into the silicon substrate, thus enabling particle sorting within microfluidic channels that are also in the same substrate.

1.2. OUTLINE OF THIS THESIS

In this thesis, in Chapter 2, the concept of pre-charged CMUT is introduced and a theoretical frame work is presented in order to quantify the amount and type of charge that is embedded within the charged CMUT. In Chapter 3, energy harvesting using pre-charged CMUT was tested and characterized. In Chapter 4, a microwatt telemetry protocol was developed using the pre-charged CMUTs, which shows that communication is possible.

In Chapter 5 high frequency CMUTs for ultrasound nerve stimulators were characterized and tested in an in-vivo model. Finally, in Chapter 6, CMUTs for acoustic particle sorting applications are investigated for integration with lab-on-a-chip devices.

BIBLIOGRAPHY

[1] T. L. Szabo, *Diagnostic Ultrasound Imaging: Inside Out: Second Edition*. 2004, pp. 1–549, ISBN: 9780123964878. DOI: 10.1016/C2011-0-07261-7.

[2] M. Meola, J. Ibeas, G. Lasalle, and I. Petrucci, "Basics for performing a high-quality color Doppler sonography of the vascular access", *Journal of Vascular Access*, vol. 22, no. 1, pp. 18–31, Nov. 2021, ISSN: 17246032. DOI: 10.1177/11297298211018060.

[3] L. Ziegler and R. T. O'Brien, "HARMONIC ULTRASOUND: A REVIEW", *Veterinary Radiology <html_ent glyph="@amp;" ascii="&"/> Ultrasound*, vol. 43, no. 6, pp. 501–509, Nov. 2002, ISSN: 1058-8183. DOI: 10.1111/j.1740-8261.2002.tb01040.x.

[4] S. G. Carlier, C. L. de Korte, E. Brusseau, J. A. Schaar, P. W. Serruys, and A. F. W. Van Der Steen, "Elastography", *European Journal of Cardiovascular Prevention {\&} Rehabilitation*, vol. 9, no. 5, pp. 237–245, 2002, ISSN: 17418275. DOI: 10.1177/174182670200900503.

[5] Y. Baribeau, A. Sharkey, O. Chaudhary, *et al.*, "Handheld Point-of-Care Ultrasound Probes: The New Generation of POCUS", *Journal of Cardiothoracic and Vascular Anesthesia*, vol. 34, no. 11, pp. 3139–3145, 2020, ISSN: 15328422. DOI: 10.1053/j.jvca.2020.07.004.

[6] D. M. Becker, C. A. Tafoya, S. L. Becker, G. H. Kruger, M. J. Tafoya, and T. K. Becker, "The use of portable ultrasound devices in low- and middle-income countries: A systematic review of the literature", *Tropical Medicine and International Health*, vol. 21, no. 3, pp. 294–311, 2016, ISSN: 13653156. DOI: 10.1111/tmi.12657.

[7] M. Z. Nasrabadi, H. Tabibi, M. Salmani, M. Torkashvand, and E. Zarepour, "A comprehensive survey on non-invasive wearable bladder volume monitoring systems", *Medical and Biological Engineering and Computing*, vol. 59, no. 7-8, pp. 1373–1402, 2021, ISSN: 17410444. DOI: 10.1007/s11517-021-02395-x.

[8] C. Wang, X. Chen, L. Wang, *et al.*, "Bioadhesive ultrasound for long-term continuous imaging of diverse organs", *Science*, vol. 377, no. 6605, pp. 517–523, Jul. 2022, ISSN: 0036-8075. DOI: 10.1126/science.abo2542.

[9] K. Shen and M. M. Maharbiz, "Design of Ceramic Packages for Ultrasonically Coupled Implantable Medical Devices", *IEEE Transactions on Biomedical Engineering*, vol. 67, no. 8, pp. 2230–2240, 2020, ISSN: 15582531. DOI: 10.1109/TBME.2019.2957732.

[10] A. M. Manjón-Sanz and M. R. Dolgos, "Applications of Piezoelectrics: Old and New", *Chemistry of Materials*, vol. 30, no. 24, pp. 8718–8726, 2018, ISSN: 15205002. DOI: 10.1021/acs.chemmater.8b03296.

[11] J. M. Rothberg, T. S. Ralston, A. G. Rothberg, *et al.*, "Ultrasound-on-chip platform for medical imaging, analysis, and collective intelligence", *Proceedings of the National Academy of Sciences of the United States of America*, vol. 118, no. 27, 2021, ISSN: 10916490. DOI: 10.1073/pnas.2019339118.

[12] C. Visser, A. S. Savoia, N. Mihajlović, *et al.*, "POSITION-II A pilot line for the next generation of smart catheters and implants", Tech. Rep., 2022.

[13] Johan H. Klootwijk, Peter Dirksen, Marcel Mulder, and Elisabeth M.L. Moonen, *Capacitive micromachined ultrasound transducer*, Jun. 2015.

2

REDUCED ORDER SEMI-ANALYTICAL MODELLING OF A PRE-CHARGED COLLAPSE-MODE CMUT

All models are wrong but some are useful.

George E.P.Box

2.1. INTRODUCTION

In this chapter a theoretical model of the the collapse-mode CMUT with a built-in charge layer is introduced. This will allow us to design better layer stacks for the device. There are several levels of complexity one could use to describe the behaviour of the CMUT. The simplest model is the mass spring damper system, which models the CMUT membrane as a stiff circular piston connected to a spring and a damper. The limitation of this model is that it is not detailed enough to explain devices with a large displacement profile such as a collapse-mode CMUT. On the other extreme there is FEA (finite element

Parts of this chapter have been published in IEEE UFFC journal titled Modeling and characterization of pre-charged collapse-mode CMUTs.

2

analysis), which unfortunately requires large computation time and resources making it difficult to iterate through different layer stacks. Furthermore, it does not provide the insights that could be gained through an analytical model [1]. As a result we will use a reduced order semi-analytical model which is in between the two extremes ([2], [3]) but which has sufficient accuracy. This chapter begins by modeling the CMUT similarly to the works of H. Köymen et al.[4] where they have modelled built-in charge with a surface charge of the opposite polarity at both sides of the charging layer and a spatially fixed volume charge uniformly distributed within the charging layer. Then this will be solved using the Galerkin discretization approach. Finally, by comparing the simulation model and the measurement results the amount of charge within the charge trapping layer will be quantified. In this work only the static displacement profile is taken into account while the dynamic operation of the CMUT was beyond the scope of this work but, which can be readily extended from the formulas that are derived in this work.

2.2. MODELING THE PRE-CHARGED COLLAPSE-MODE CMUT

A schematic representation of the pre-charged collapse-mode CMUT is shown in Fig. 2.1(a). In this model the CMUT is modeled as a vibrating axisymmetric clamped membrane. The charged layer is embedded in between the top and bottom electrode separated by a passivation layer. In Fig. 2.1(a), t_m is the thickness of the top membrane, ρ_m is the mass density of the top membrane, t_g is the height of the vacuum gap, a is the radius of the CMUT, and w is the displacement of the membrane. Fig. 2.1(b) examines the force acting on the top membrane which are 1) the electrostatic pressure from the built-in charge and the external voltage, 2) contact force which is the reactive force that occurs where the top membrane touches the bottom membrane, 3) the biaxial residual stress and 4) the atmospheric pressure.

According to [3], the governing dynamic equation not including the trapped charge is,

$$\rho_{tp} t_m \frac{\partial^2 w(r,t)}{\partial^2 t} + D\nabla_r^4 w(r,t) = \underbrace{-\frac{\varepsilon_0 V(t)^2}{2(t_{\text{eff}} + w(r,t))^2}}_{①} + \underbrace{\frac{H_{ab}}{2}\operatorname{erfc}\left(\frac{t_g + w(r,t)}{\sigma\sqrt{\pi}}\right)}_{②} + \underbrace{\frac{\tau t_m}{r}\frac{\partial}{\partial r}\left(r\frac{\partial w(r)}{\partial r}\right)}_{③} \underbrace{- P_{atmos}}_{④} \tag{2.1}$$

$$\nabla_r^4 = \left(\frac{\partial^2}{\partial r^2} + \frac{1}{r}\frac{\partial}{\partial r}\right)^2 \tag{2.2}$$

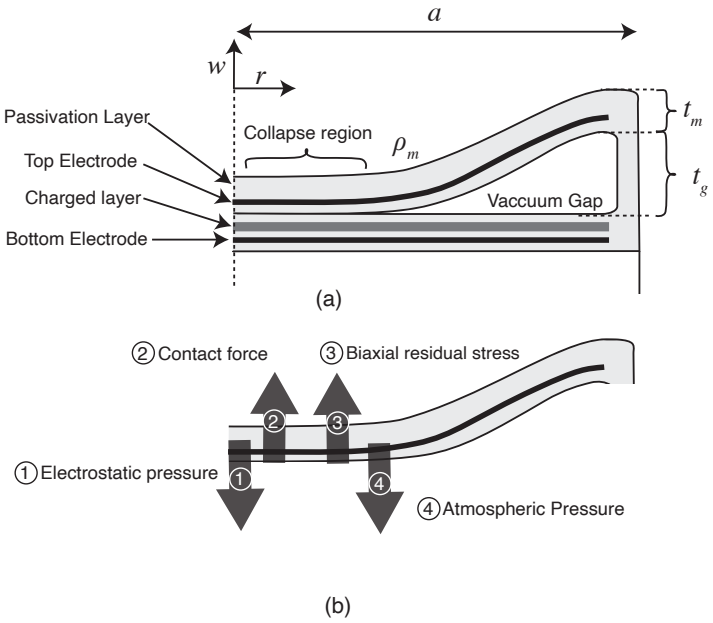

Figure 2.1: (a) schematic diagram of the cross section and variables of the CMUT (b) the forces acting on the top membrane.

The four different forces acting on the membrane are denoted with a dashed line beneath the equation. In this equation D is the flexural rigidity of the top membrane, $V(t)$ is the external voltage applied to the top membrane, σ is the surface roughness, H_{ab} is the indentation hardness, τ is the biaxial residual stress, erfc is the complementary error function, and t_{eff} is the distance between the top and bottom electrodes corrected for the dielectric constants and defined as,

$$t_{eff} = t_g + \sum \frac{t_i}{\varepsilon_i} \tag{2.3}$$

where $\frac{t_i}{\varepsilon_i}$ is the thickness of the dielectric layers between the top and bottom electrode divided by its corresponding dielectric constant. For further detail, readers are referred to [3], [5]. In this work we adapt this equation by adding the electrostatic force from the built-in charge. This will require some modification to the term concerning the electrostatic force of Eq. 2.1.

Fig. 2.2 is a small cross section of the CMUT at an arbitrary radius r. In this figure, the dielectric layer thickness is denoted as t with a subscript from 1 to 4. The charge trapping layer has a dielectric constant of ε_{charge} and is sandwiched between SiO_2 layers.

The charge distribution is defined similarly to [4], where a uniform monopolar volume charge of $\rho_m(r)$ exists inside the charging layer, as well as an electret with a downward polarization that is defined by a surface charge of the opposite polarity of $\sigma_0(r)$ on both sides of the charging layer. Furthermore, to explicitly show that the charge density can have an axisymmetric distribution, the surface charge and the volume charge is shown as a function of the radius r. Due to the multiple different dielectric constants used in this layer stack, there is no simple solutions that could be directly used to calculate the electrostatic force. However, for a slightly more simple model as shown in Fig. 2.2(b) where there is only one dielectric layer on one side of the electrode and the other side is a vacuum gap, G.M.Sessler [6] derived the electrostatic pressure on the top electrode for a generalized charge distribution within the dielectric layer. Thus, by converting the layer stack and the charge distribution in Fig. 2.2(a) to Fig. 2.2(b) the electrostatic force on the top membrane can be derived. By comparing these two figure we see that,

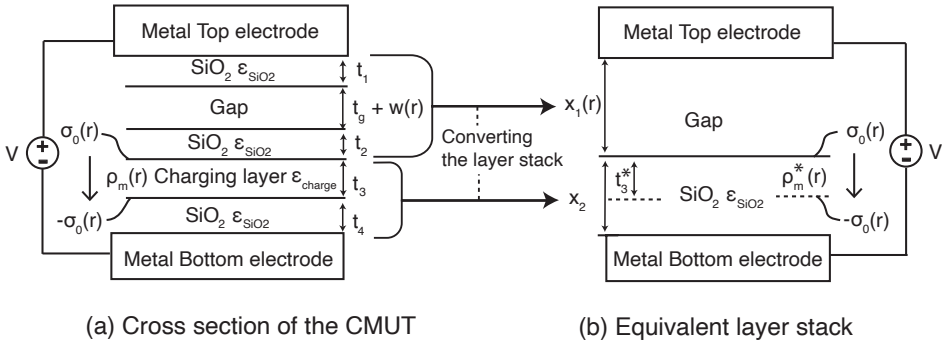

Figure 2.2: Cross section diagram of the charged CMUT device connected to a voltage source. (a) The actual layer stack and the location of the charge (fixed volume charge and surface charge). (b) The layer stack proposed in G.M.Sessler with only a vacuum gap and a dielectric layer. The charge distribution is also shown in the figure.

$$x_1(r) = t_g + w(r) + \frac{t_1 + t_2}{\varepsilon_{SiO_2}} \quad , \quad x_2 = t_4 + t_3 \frac{\varepsilon_{SiO_2}}{\varepsilon_{charge}} \tag{2.4}$$

where t_1, t_2 and $t_g + w(r)$ are referred to vacuum permittivity and t_3, t_4 are referred to the relative permittivity of SiO_2. For convenience we will define $t_3^* = t_3 \frac{\varepsilon_{SiO_2}}{\varepsilon_{charge}}$ in the following derivation. Since the total amount of charge is constant $\rho_m^*(r)t_3^* = \rho_m(r)t_3$ should be satisfied. Thus, the charge distribution is scaled as $\rho_m^*(r) = \rho_m(r)\frac{\varepsilon_{charge}}{\varepsilon_{SiO_2}}$. The charge

distribution after converting it to its equivalent layer stack is,

$$\rho^*(r,x) = \begin{cases} \sigma_0(r)\delta(x) - \sigma_0(r)\delta(x - \mathrm{t}_3^*) + \rho_m^*(r), & \text{if } 0 \le x \le \mathrm{t}_3^* \\ 0 & \text{otherwise} \end{cases} \tag{2.5}$$

where $\delta(x)$ is a dirac delta function used to express the surface charge. Again, referring to [[6], Eq. 14 and Eq. 34] the electrostatic pressure $P_e(r)$ acting on the top membrane for a generalized charge distribution is,

$$P_e(r) = -\frac{\varepsilon_0}{2s(r)^2}\left(V - V_{eff}(r)\right)^2 \tag{2.6}$$

where,

$$V_{eff}(r) = \frac{x_2\sigma_1(r)}{\varepsilon_0\varepsilon_{SiO_2}} \tag{2.7}$$

and

$$\sigma_1(r) = \frac{1}{x_2}\int_0^{x_2}(x_2 - x)\rho^*(r,x)dx \tag{2.8}$$

where $s(r) = \sum x_i(r)/\varepsilon_i = \mathrm{t}_{eff} + w(r)$. From Eq. 2.6, the force from the internal charges act effectively as if a DC bias voltage of $V_{eff}(r)$ is subtracted from the external voltage V. The only obscure value in this equation is $\sigma_1(r)$ which is the contribution of the surface and volume charge. By inserting Eq. 2.5 to Eq. 2.8 and solving the integration,

$$\sigma_1(r) = \mathrm{t}_3\left(1 - \frac{\mathrm{t}_3^*}{2x_2}\right)\cdot\rho_m(r) + \frac{\mathrm{t}_3^*}{x_2}\cdot\sigma_0(r) \tag{2.9}$$

From this result, $\sigma_1(r)$ is characterized as a sum of the volume charge (1st term) and the surface charge (2nd term). Finally, we include the electrostatic pressure with the internal charge (Eq. 2.6) into the membrane dynamics equation (Eq. 2.1) as,

$$\begin{aligned}\rho_{tp}t_m\frac{\partial^2 w(r,t)}{\partial^2 t} + D\nabla_r^4 w(r,t) = &-\frac{\varepsilon_0}{2(\mathrm{t}_{\mathrm{eff}} + w(r,t))^2}\left(V(t) - V_{eff}(r)\right)^2 \\ &+ \frac{H_{ab}}{2}\mathrm{erfc}\left(\frac{t_g + w(r,t)}{\sigma\sqrt{\pi}}\right) + \frac{\tau t_m}{r}\frac{\partial}{\partial r}\left(r\frac{\partial w(r)}{\partial r}\right) - P_{atmos}\end{aligned} \tag{2.10}$$

Eq. 2.10 can be numerically solved by non-dimensionalizing the equation and using the Galerkin Approach similarly to the works of [2], [3], [5] and by considering 6 or more vibrational modes. In this derivation we omitted the derivation of the electric field between the top and bottom electrode to keep the derivation short. A detailed derivation of the electric field can be found in the Appendix A.1. Finally this equation can be extended

to CMUT operation in water if mutual and self acoustic loading is incorporated [7], [8].

2.2.1. CHARGE DISTRIBUTION

In this work, charges will be injected into the charging layer by applying a sufficiently high voltage to bring the CMUT into collapse mode and by tunneling charges through the region where the top and bottom membrane are in contact. Consequently, the injected charges will be distributed with an axial symmetric distribution, which can readily be implemented in the model. For simplicity, in this work the charge distribution will be defined as a constant density with a radius of r_{charge} as follows,

$$\sigma_0(r) = \begin{cases} \sigma_0, & \text{if } 0 \le r \le r_{charge} \\ 0 & \text{otherwise} \end{cases} \tag{2.11}$$

$$\rho_m(r) = \begin{cases} \rho_m, & \text{if } 0 \le r \le r_{charge} \\ 0 & \text{otherwise} \end{cases} \tag{2.12}$$

where, r_{charge} is the contact radius during the charging process.

2.3. QUALITATIVE CHANGES TO THE C-V CURVE

A typical capacitance to voltage (C-V) curve of a CMUT is shown in Fig. 2.3. If we follow the hysteresis curve, starting near 0 V, the CMUT is in non-collapse mode which has a low capacitance because there is a gap between the top and bottom membrane. As the voltage is increased, the CMUT goes into collapse, which causes the top membrane to touch the bottom membrane resulting in a large increase in the capacitance. The voltage is then decreased until the top membrane snaps back from the collapse-mode resulting in a lower capacitance. This cycle can be repeated for the negative voltage which normally results in a symmetrical C-V curve as shown in the figure.

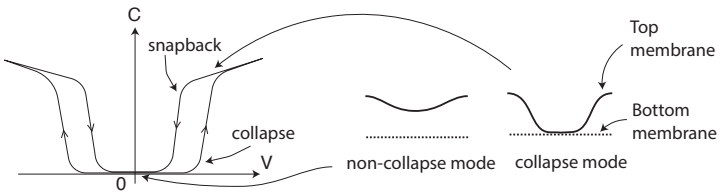

Figure 2.3: A typical C-V curve when there is no charge inside the dielectric layer.

When charges are trapped inside the CMUT, the Capacitance to Voltage (C-V) curve

shifts with respect to the 0 V axis. The root cause can be seen in Eq. 2.6, where there is a second term $V_{eff}(r)$ that is subtracted from the external voltage V. In the previous section it was defined that charges will distribute only between $0 < r < r_{charge}$. Thus, for $r_{charge} > 0$, $V_{eff}(r) = 0$ from Eq. 2.7, 2.9.

In this section we qualitatively describe in which direction the C-V curve will shift depending on the type of charge that is distributed between $0 < r < r_{charge}$ of the CMUT. If $V_{eff}(r) > 0$, the internal voltage acts against the external voltage V, thus requiring a larger voltage to bring the CMUT into collapse, which will shift the C-V curve to the right. If $V_{eff}(r) < 0$ the internal voltage acts alongside the external voltage V shifting the C-V curve to the left. Therefore, the sign of $V_{eff}(r)$ indicates in which direction the C-V curve will shift. In this section, the following four cases are considered, whereas the actual charging can be considered as a combination of these four cases.

Case 1 ($\sigma_0 = 0$, $\rho_0 < 0$)**:** Only electrons.

Case 2 ($\sigma_0 > 0$, $\rho_0 = 0$)**:** Only a downward polarization.

Case 3 ($\sigma_0 < 0$, $\rho_0 = 0$)**:** Only an upward polarization.

Case 4 ($\sigma_0 = 0$, $\rho_0 > 0$)**:** Only holes.

Case 4 is also included in the list, yet it is unlikely that this situation will arise given that the dielectric stack is sandwiched between two metal conductors where no injection of holes exist. Thus, we will examine the three other cases in more detail and study how it will shift the C-V curve. Fig. 2.4(a) shows a schematic drawing of how the charge is positioned in the dielectric layer for the three cases. The sign of V_{eff} is equivalent to finding the sign of σ_1 according to Eq. 2.7 and the definition of σ_1 can be found in Eq. 2.9. Since the coefficients multiplied to the $\rho(r)$ and $\sigma(r)$ are both positive, the sign of V_{eff} can easily be found for each cases as, Case 1 and Case 3: $V_{eff} < 0$ ($\because \sigma_1 < 0$) and for Case 2: $V_{eff} > 0$ ($\because \sigma_1 > 0$). Thus the C-V curve will shift to the left for Case 1 and 3 and it will shift to the right in Case 2 as shown in Fig. 2.4(b).

The magnitude of trapped charge is typically derived through measuring how much the C-V curve is shifted. However, if different types of charges are superimposed and if there is a spatial distribution of charges, this method does not work. For our work we derive the amount of trapped charge by comparing the measured C-V profile with the modelled C-V profile.

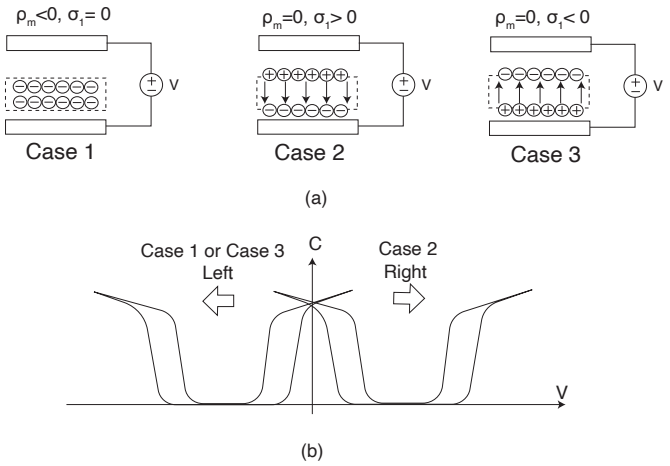

Figure 2.4: (a) A schematic drawing of where and what polarity of charge is trapped for the three cases. (b) For Case 1 and Case 3 the C-V curve will shift to the left and for Case 2 the C-V curve will shift to the right.

2.4. OVERVIEW OF THE FITTING PROCESS

The aim of the fitting process is to derive relevant parameters (i.e. σ_0, ρ_m and r_{charge}) by comparing the semi-analytic reduced order model (ROM) to the measurement results. However, to avoid over fitting the model with all of the measurement results, we tuned the ROM in a sequential manner by giving limited information to the ROM and by checking the model against the measurement results.

The steps that were taken to fit the simulation model and the measurement results are summarized in Fig. 2.5. First, the ROM is implemented in MATLAB with the membrane dynamics Eq. 2.10 , layer stack, geometry of the membrane and gap height. Second, using the membrane profile measured at 0 V, the uniform biaxial residual stress τ is tuned so that the membrane profile matches the measurement result. This serves as the baseline model of the CMUT with no charging. Then, the pull-in voltage and the snap-out voltage is predicted with the ROM and compared to the fast C-V curve measurements. Furthermore, the collapse diameter is also compared between the ROM and the measurement results for bias voltages up to 130 V. Afterwards, the CMUT is charged at two conditions, one with +170 V and the other with -170 V, each for 5 min. The collapse radius at +170 V is used as the input for r_{charge} (see Eq. 2.5). Finally, the surface charge (σ_0) or the volume charge (ρ_m) is tuned to match the C-V curve.

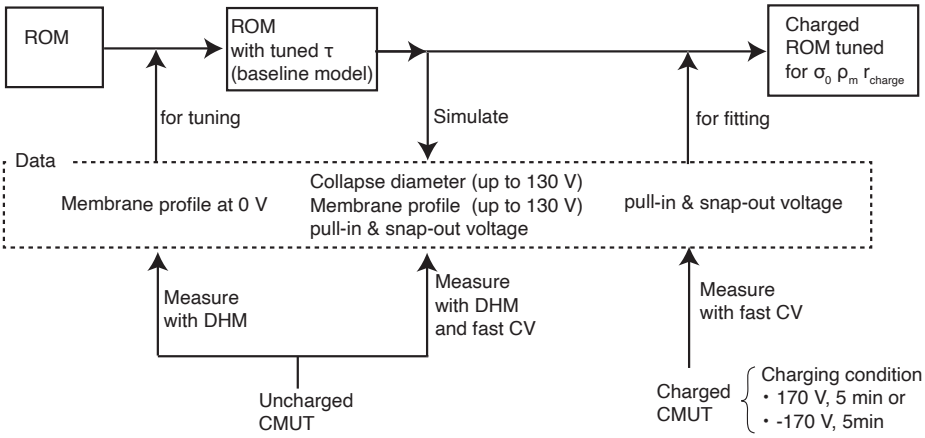

Figure 2.5: Simulation flow diagram

2.5. RESULT AND DISCUSSION

Four CMUT variants (P67, P68, P103 and P177) were tested in this work. Table 2.1 summarizes these different variants.

Table 2.1: Simulation parameters.

	P67	P68	P103	P177	Unit	Description
t_1	0	30	50	75	nm	Insulation thickness see Fig. 2.2
t_2	50	30	50	75	nm	Insulation thicknesssee Fig. 2.2
t_3	200	240	200	250	nm	Charge layer thickness see Fig. 2.2
t_4	50	10	50	50	nm	Insulation layer thickness see Fig. 2.2
t_{eff}	546	544	558	474	nm	Total effective thickness Eq. 2.3
t_m	2500	2500	3000	3100	nm	Total thickness of the top membrane
t_g	500	500	500	400	nm	Gap height
D	$2.4{\cdot}10^{-7}$	$2.4{\cdot}10^{-7}$	$4.1{\cdot}10^{-7}$	$4.5{\cdot}10^{-7}$	$Pa{\cdot}m^3$	Flexural rigidity
ρ_{tp}	3290	3290	3290	3290	kg/m^3	Combined mass density of the top plate
a	67.5				µm	Plate Radius
ε_0	$8.85{\cdot}10^{-12}$				F/m	Vacuum Permittivity
ε_{SiO_2}	4.3				-	Relative Permittivity of SiO_2
ε_{charge}	8.8				-	Relative Permittivity of Al_2O_3
P_{atmos}	$1.01325 \cdot 10^5$				Pa	Atmospheric pressure
H_{ab}, n = a, b	$2{\cdot}10^9$				Pa	Indentation hardness
σ	4				nm	Combined surface roughness standard deviation
modes	6				-	The number of vibrational modes used

2.5.1. TUNING THE REDUCED ORDER MODEL

The exact value of the uniform biaxial residual stress parameter for a given layer stack depends on the fabrication process and is not known. In other works it has been shown that this value could be in the order of several hundreds of MPa [9]. In this work, the

membrane profile at 0V was compared between the measurement and the simulation for each variant to tune τ. Fig. 2.6, shows the result of tuning along with the required uniform biaxial residual stress parameter τ. The results showed that the values were typically a negative stress of several hundred of MPa(i.e. P67:−650 MPa, P68:−550 MPa, P103:−650 MPa, P177:−200 MPa). Some values are quite large but this is due to the fact that the tuning process is also tuning the non-idealities in the model. To give an example, the actual CMUT device may not have a perfectly clamped rim. Given this circumstance the values shown here are within reasonable range [9].

Fig. 2.7 shows several measurements from the DHM (Digital Holographic Microscope) and the simulated membrane profile between 0 V to 130 V. Only a few profiles are shown in this figure for clarity. The simulations and the measurements are in good agreement and show that the model accurately predicts the deflection profile. P103 seemed to have a gap height that was 30 nm or so less than the expected 500 nm gap height. This could be due to some imperfect fabrication process or a calibration error during the measurement. The displacement at the center (r = 0) is plotted against the voltage for each variant in Fig. 2.8. The pull-in voltage is accurately predicted by the ROM. The collapse diameter was defined as the diameter in which the membrane profile was 10 nm higher than the lowest deflection point along the collapse region. The collapse diameter is compared with the membrane profile in Fig. 2.9, which also compares well with the simulation and the measurement.

Fig. 2.11 shows the measured fast C-V curves for all variants, when the CMUT was not charged (blue solid line), charged at +170 V for 5 min (pink solid line), and charged at -170 V for 5 min (black solid line). For the CMUTs that are not charged the general shape of the C-V curve follows what was shown in Fig. 2.3, where the C-V curve is symmetrical around the center and has a different pull-in voltage and a snap-out voltage leading to a hysteresis behaviour. However, for P68, P103 and P177 there is an abrupt change in the capacitance that we see at 0 V, and it is not clear to why this happens. From Section 2.3 we qualitatively showed that depending on the type of charge, the C-V curve can shift either to the left or to the right. However, it is only when there is downwards polarization which results in the C-V curve to shift to the right assuming that no injection of holes can occur in the Al_2O_3 layer. Thus, our work clearly indicates that there is polarization behaviour of the Al_2O_3 layer. Ferroelectric-like behaviour such as this was reported by Peng et. al. [10] and they have associated the effect to oxygen vacancies that move due to the external electric field. Another interesting observation that can be made from this C-V curve is that the amount of C-V curve shifting to the left or to the right is nearly the same for all CMUTs. This shows that the polarization behaviour of the Al_2O_3 layer is

dominant compared to the fixed volume electron charges which tends to pull the C-V curve to the left. Thus, in the consecutive process of fitting the C-V curve, only the polarization will be taken into account and the fixed volume charges will be ignored ρ_m = 0 C/m^3. In the same figure the simulated C-V curve for all variants are shown with a dashed line on top of the corresponding measurement result. The capacitance is simulated from the membrane profile and does not include the transient movement of the membrane which typically is referred to as mechanical capacitance. The collapse radius at 170 V is simulated and is used for the charge radius in each variant (i.e. for P67 and P68 : r_{charge} = 40 µm and for P103 and P177 : r_{charge} = 32 µm). This can be seen in Fig. 2.10 where the electric field is plotted as a heat map for each variation. The positive direction of the electric field is defined to be downwards in this figure. Then the polarizing surface charge σ_0 is tuned either to the positive or to the negative to have the best fit with the measured C-V curve. The required surface charge for each variant is shown in the same figure. For P67, P68 and P103 the amount of charge was nearly ±0.02 C/m^2 and for P177 this was significantly lower approximately ± 0.005 C/m^2. This difference is due to the lower electrical field that existed for P177 during the charging process due to the thicker insulation layer between the top and bottom electrode. The amount of trapped charge is similar to the maximum charge density that has been reported in literature [11], [12] which is ≈ 0.016 C/m^2.

2.5.2. CHANGING CHARGE RADIUS

For our simulations we estimated r_{charge} through simulating the collapse radius at 170 V. Then we used this as the input for fitting the surface charge σ_0 which lead to an accurate prediction of the membrane profile. To examine how sensitive the CV curve is for different r_{charge}, in Fig. 2.12 the C-V curve was simulated using the parameters for P67. At r_{charge} = 60 µm the C-V curve is simply a parallel shifted version of the original CV curve. When r_{charge} is smaller, the required voltage to bring the CMUT into collapse-mode becomes lower and the snap-out voltage and the pull-in voltage becomes closer as shown in the same figure. This is because the total amount of charge is smaller when r_{charge} is smaller and thus the repelling force that the internal charge induces is smaller leading to a lower collapse voltage.

2.5.3. DISCHARGING OF CMUTS

The tunneling behaviour of electrons through insulation material such as SiO_2 has been extensively studied for floating gate memories [13]. The main mechanism of charge tunneling through SiO_2 is referred to as Fowler Nordheim (FN) tunneling. This occurs when

the electric field in the oxide exceeds 5 to 6 MV/cm. This also explains why P177 does not charge as much compared to the other variant, because if we see Fig. 2.10 the electric field on the top and bottom SiO_2 layer is slightly less than 5MV/cm which is insufficient to initiate electron tunneling. Once the device is charged it is essential that the amount of internal charge is not too high as to initiate natural discharging of the device through FN tunneling. Fig. 2.13 and Fig. 2.14 show a color plot of the electric field for P67 and P68 respectively, which stayed in collapsed after the initial charging process. Several values of the electric field are indicated in the figure. The most important electric field in terms of the natural discharging process is the electric field across the SiO_2 layer between the metal layer and the charging layer. For both cases the electric field through the SiO_2 is sufficiently low (< 2.5 MV/cm) to prevent them from naturally discharging. In other words, the only way that the electrical field weakens will be due to diffusion/relocation of the charges within the charging layer.

2.6. CONCLUSION

In this work the ROM previously presented in [3] was extended with a charging layer between the top and bottom layer. The important parameters that govern the effect of chargingere the distribution of the charge (r_{charge}) and the type of charge (surface charge σ_0 or volume charge ρ_m). It was found that for the CMUTs that were fabricated for this work, the polarization of the Al_2O_3 layer was the dominant charging mechanism, yet this will change depending on the material of the charging layer or even the deposition conditions of the same material. Furthermore, it was also shown that the embedded charge will not easily discharge because the electric field within the insulation layer (< 2.5 MV/cm) does not exceed the FN regime (5- 6 MV/cm). For future work, life time tests should be conducted to see how long the charges can be retained within the charging layer and the discharging process should be fitted with the model that is presented in this work. Perliminary results already indicate that the life time will be nearly 3 years at body temperature [14]. In addition, this model can also be used to simulate the dynamic behaviour of the CMUT and simulate acoustic pressure generated from the CMUT. It would be an important future work to understand how this compares to traditional CMUTs where the bias voltage is applied externally with no trapped charge.

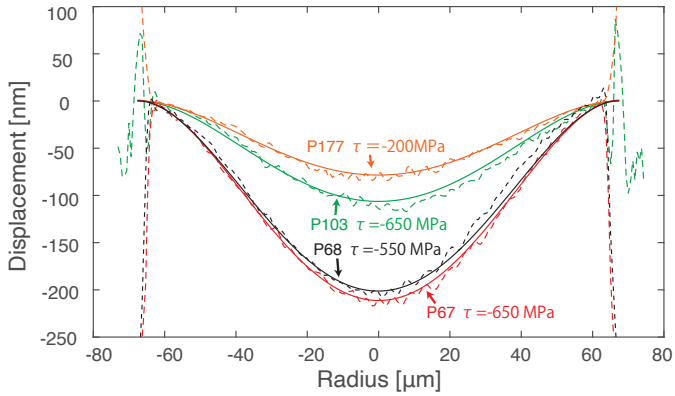

Figure 2.6: Membrane profile at 0 V external bias to tune τ. The dashed line is the measurement result of the membrane profile measured with a DHM and the solid line is the simulated membrane profile with the indicated tuning parameter τ.

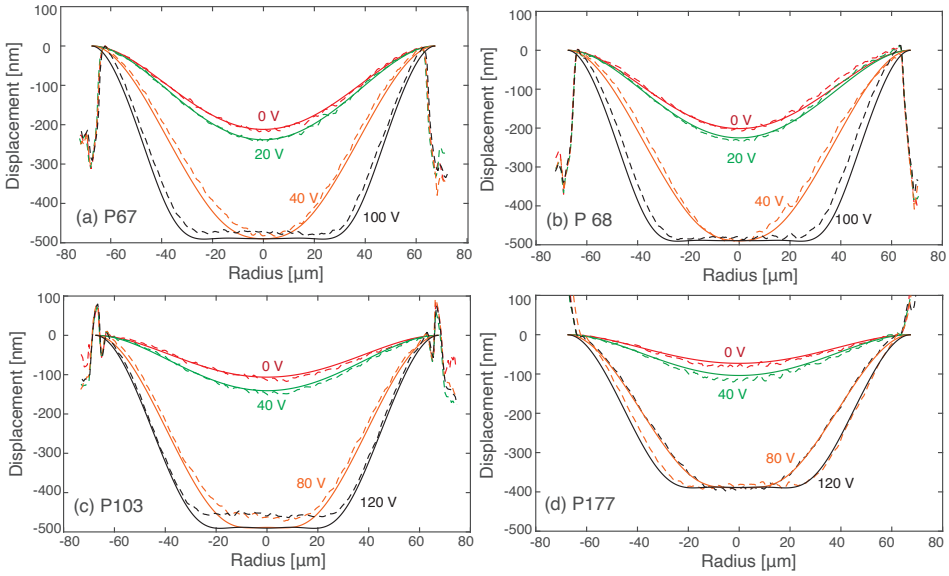

Figure 2.7: Result of fitting the membrane profile. The dashed line is the measurement result and the solid line is the simulation result.

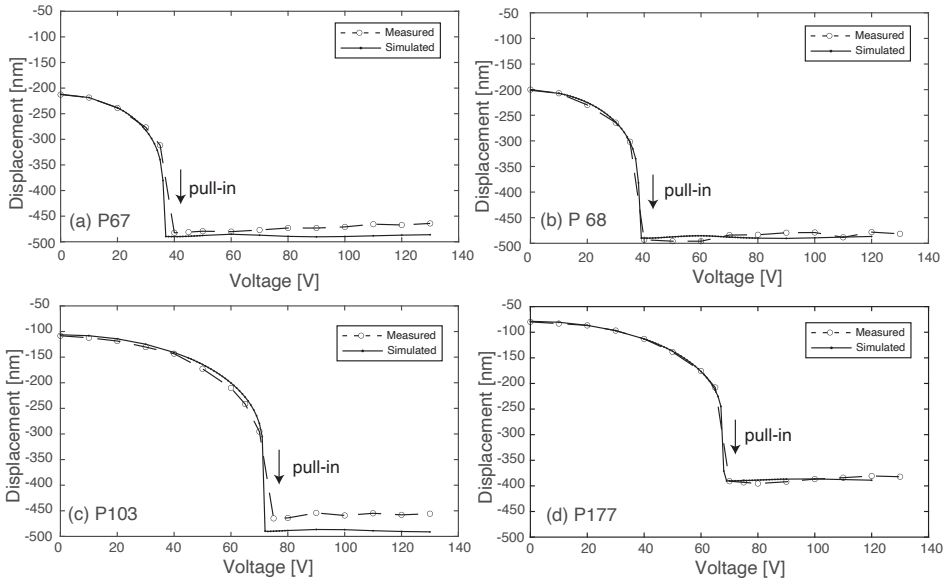

Figure 2.8: Transversal Displacement of the CMUT at the center (r = 0 µm).

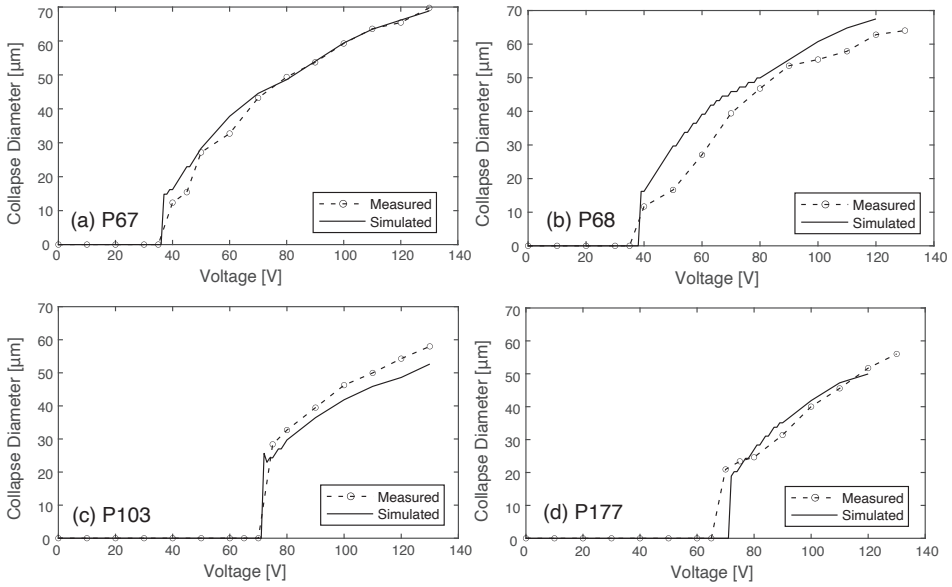

Figure 2.9: Collapse diameter as a function of voltage for all variants.

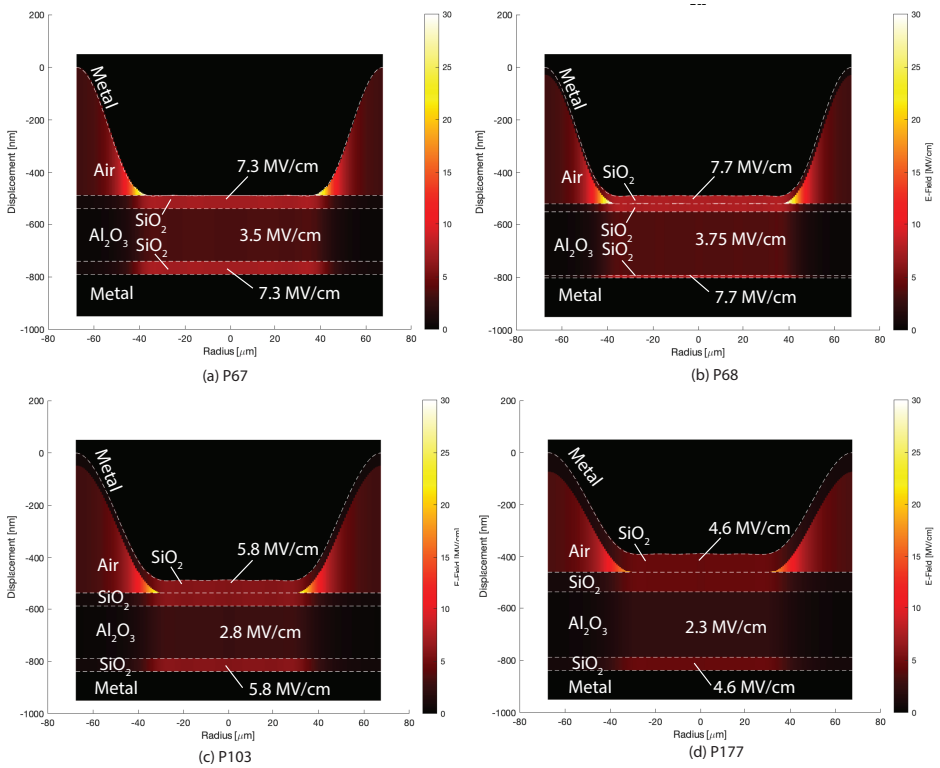

Figure 2.10: Electric Field at 170 V during the charging process. (a) P67 (b) P68 (c) P103 (d) P177

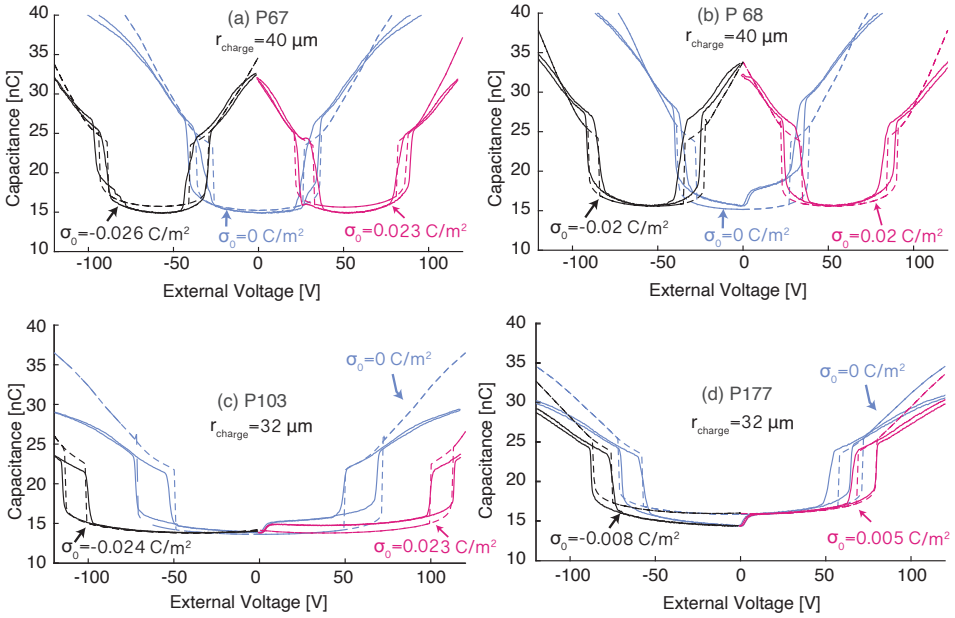

Figure 2.11: Comparison between the CV curve simulated (dashed-line) and measured (solid line) with fast C-V for uncharged CMUT and charged CMUT (+/-170 V for 5 min) The surface charge σ_0 is defined as indicated in each figure and was tuned so that the pull-in voltage and the snap-out voltage showed a good match. ρ_m = 0 C/m^3 for all figures

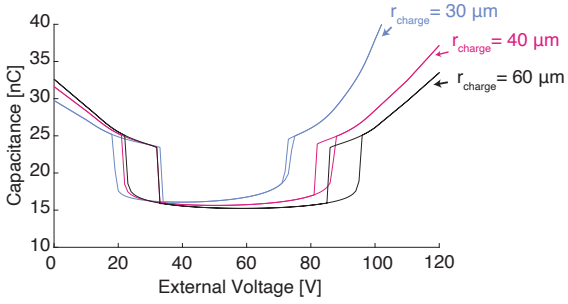

Figure 2.12: The simulated CV curve for P67 with r_{charge} = 30 µm, 40 µm, 60 µm. The other parameters are shown in Table 2.1

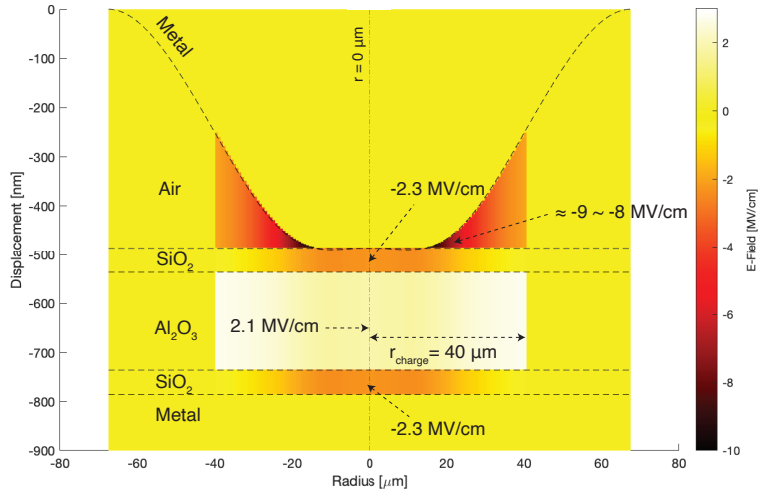

Figure 2.13: P67 Electric field after charging. $r_{charge} = 40\,\mu\text{m}$, $\sigma_0 = 0.023\,\text{C/m}^2$, $\rho_m = 0\,\text{C/m}^3$.

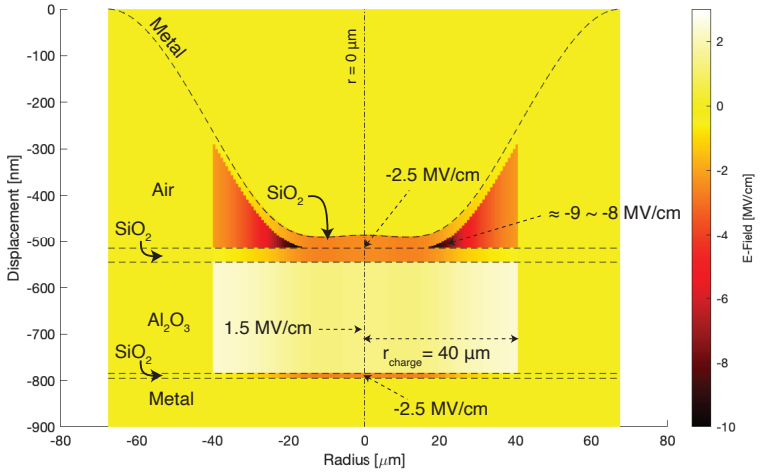

Figure 2.14: P68 Electric field after charging. $r_{charge} = 40\,\mu\text{m}$, $\sigma_0 = 0.02\,\text{C/m}^2$, $\rho_m = 0\,\text{C/m}^3$.

BIBLIOGRAPHY

[1] J. Wang, X. Liu, Y. Yu, *et al.*, "A review on analytical modeling for collapse mode capacitive micromachined ultrasonic transducer of the collapse voltage and the static membrane deflections", *Micromachines*, vol. 12, no. 6, 2021, ISSN: 2072666X. DOI: 10.3390/mi12060714.

[2] G. W. Vogl and A. H. Nayfeh, "A reduced-order model for electrically actuated clamped circular plates", *Journal of Micromechanics and Microengineering*, vol. 15, no. 4, pp. 684–690, 2005, ISSN: 09601317. DOI: 10.1088/0960-1317/15/4/002.

[3] M. Pekař, S. H. van Nispen, R. H. Fey, S. Shulepov, N. Mihajlović, and H. Nijmeijer, "A fluid-coupled transmitting CMUT operated in collapse mode: Semi-analytic modeling and experiments", *Sensors and Actuators, A: Physical*, vol. 267, no. 2017, pp. 474–484, 2017, ISSN: 09244247. DOI: 10.1016/j.sna.2017.09.055. [Online]. Available: http://dx.doi.org/10.1016/j.sna.2017.09.055.

[4] H. Koymen, A. Atalar, S. Guler, I. Koymen, A. S. Tasdelen, and A. Unlugedik, "Unbiased Charged Circular CMUT Microphone: Lumped-Element Modeling and Performance", *IEEE Transactions on Ultrasonics, Ferroelectrics, and Frequency Control*, vol. 65, no. 1, pp. 60–71, Jan. 2018, ISSN: 0885-3010. DOI: 10.1109/TUFFC.2017.2773490. [Online]. Available: https://ieeexplore.ieee.org/document/8107590/.

[5] V. Nispen, "Model-Based Analysis of a Capacitive Micromachined Ultrasonic Transducer Operated in Collapse Mode Master thesis", 2017.

[6] G. M. Sessler, "Electric Fields and Forces due to Charged Dielectrics", *Journal of applied physics*, vol. 43, no. November 2003, pp. 405–408, 1972. DOI: 10.1063/1.1661128.

[7] S. Satir and F. L. Degertekin, "A nonlinear lumped model for ultrasound systems using CMUT arrays", *IEEE Transactions on Ultrasonics, Ferroelectrics, and Frequency Control*, vol. 62, no. 10, pp. 1865–1879, Oct. 2015, ISSN: 0885-3010. DOI: 10.1109/TUFFC.2015.007145. [Online]. Available: http://ieeexplore.ieee.org/document/7296775/.

[8] A. Bozkurt and F. Y. Yamaner, "P3R-6 A Lumped Circuit Model for the Mutual Radiation Impedance of Acoustic Array Elements", in *2006 IEEE Ultrasonics Symposium*, IEEE, 2006, pp. 2385–2388, ISBN: 1-4244-0201-8. DOI: 10.1109/ULTSYM.2006.295. [Online]. Available: http://ieeexplore.ieee.org/document/4152151/.

[9] M. S. Salim, M. F. Abd Malek, R. B. Heng, K. M. Juni, and N. Sabri, "Capacitive Micromachined Ultrasonic Transducers: Technology and Application", *Journal of Medical Ultrasound*, vol. 20, no. 1, pp. 8–31, 2012, ISSN: 09296441. DOI: 10.1016/j.jmu.2012.02.001. [Online]. Available: http://dx.doi.org/10.1016/j.jmu.2012.02.001.

[10] Y. Peng, G. Han, F. Liu, *et al.*, "Ferroelectric-like Behavior Originating from Oxygen Vacancy Dipoles in Amorphous Film for Non-volatile Memory", *Nanoscale Research Letters*, vol. 15, no. 1, 2020, ISSN: 1556276X. DOI: 10.1186/s11671-020-03364-3.

[11] J. J. Gielis, B. Hoex, M. C. Van De Sanden, and W. M. Kessels, "Negative charge and charging dynamics in Al2O3 films on Si characterized by second-harmonic generation", *Journal of Applied Physics*, vol. 104, no. 7, 2008, ISSN: 00218979. DOI: 10.1063/1.2985906.

[12] X. Zhang, B. W. Liu, Y. Zhao, C. B. Li, and Y. Xia, "Influence of annealing temperature on passivation performance of thermal atomic layer deposition Al2O3 films", *Chinese Physics B*, vol. 22, no. 12, pp. 2–7, 2013, ISSN: 16741056. DOI: 10.1088/1674-1056/22/12/127303.

[13] C. Zhao, C. Z. Zhao, S. Taylor, and P. R. Chalker, "Review on Non-Volatile Memory with High-k Dielectrics: Flash for Generation Beyond 32 nm", pp. 5117–5145, 2014. DOI: 10.3390/ma7075117.

[14] M. Saccher, S. Kawasaki, and R. Dekker, "The long-term reliability of pre-charged CMUTs for the powering of deep implanted devices", in *IEEE International Ultrasonics Symposium, IUS*, 2021. DOI: 10.1109/IUS52206.2021.9593683.

3

ULTRASOUND POWER RECEPTION WITH A PRE-CHARGED COLLAPSE-MODE CMUT

Something in the concept of be opportunistic
and ones trash is ones gold type of thing

TBD

3.1. INTRODUCTION

Over the last decade, Implantable Medical Devices (IMDs) are becoming smaller, smarter, and more energy efficient [1]. Yet, one of the significant challenges for these devices that remains till now is the large volume of the battery. For example, cardiac pacemakers and vagus nerve stimulators have a battery and the pulser positioned at the infraclavicular area [2], [3]. The lead at the stimulus location is connected to the battery by a cable that runs through the body. The complexity of the lead, cable, and battery increases the potential for infection during the surgery. Therefore, significant research interest has been devoted to the development of wireless power transfer techniques that could recharge

Parts of this chapter have been published in IEEE wireless power transfer conference **324**, 289 (2021).

the IMD from outside of the body, relaxing the requirement for the battery. Thus, enabling the development of smaller and leadless implants [4], [5].

Several methods have been investigated to wirelessly transfer power into the human body which are, ultrasound, radiofrequency (RF) [6], and inductive coupling [7]. Among them, ultrasound offers the best trade-off to power deep miniaturized IMDs due to its low attenuation through body tissue and its short wavelength, allowing precise focusing of energy to deep locations within the body [8].

The lead zirconate titanate (PZT) transducer is still the main candidate for receiving ultrasound energy. However, PZT is not biocompatible and will require a hermetic encapsulation for long term use within the body [9]. In addition, PZT is typically bulky and requires a specialized assembly process to integrate it with miniature IMDs such as dicing or wire bonding. This leads to an increase in the device's overall size, and limits the production volume o§f such devices.

Another alternative technology to receive ultrasound energy are micro-electro-mechanical systems (MEMS) based ultrasound transducers such as the broadband piezoelectric ultrasonic energy harvester (PUEH) [10]. PUEH uses microfabricated PZT diaphragm arrays to receive ultrasound power. Thus, they can be integrated more easily with ASICs compared to bulk PZT. B. Herrera et al. presented an AlN based piezo micromachined ultrasonic transducer (PMUT) replacing PZT material for a more biocompatible alternative. However, the reported efficiency was less than one percent [11]. Therefore, further investigation needs be done to establish a biocompatible, highly efficient ultrasound transducer technology that can be monolithically integrated with an ASIC for the next generation of miniature IMDs. The pre-charged CMUTs fabricated in this work is biocompatible because they are passivated with a several micron thick Si_3N_4 layer. Furthermore, the fabrication of these devices is done with standard IC-based fabrication process, which allows them to be monolithically integrated with an ASIC.

In this work, we propose a pre-charged collapse-mode CMUT. Fig. 3.1(a) is the schematic cross section of a CMUT in its unbiased state. A collapse-mode CMUT operates by applying a sufficient amount of bias voltage $\approx 100\,V$ to bring the CMUT membrane into contact with the bottom substrate (see Fig. 3.1(b)). At this state by applying an AC voltage the suspended donut region vibrates to generate an acoustic wave into the medium above the CMUT.

However, the use of a high external bias voltage is not ideal for the operation of CMUTs within the body. In Fig. 3.1(c) the external bias voltage is substituted with an internal charge storage layer embedded at the dielectric immediately above of the bottom electrode. The amount of trapped charge is sufficient to keep the CMUT permanently in

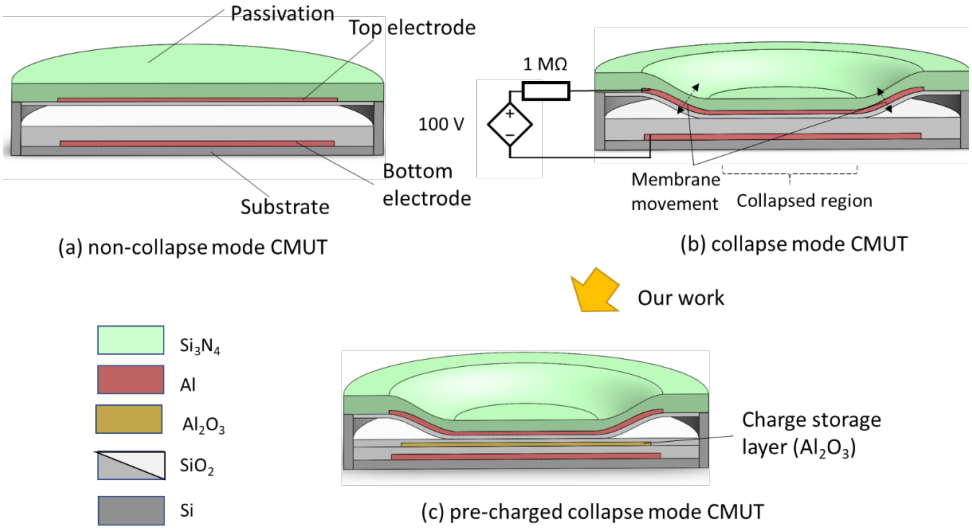

Figure 3.1: Comparison of CMUT working at different operating modes (a) CMUT unbiased state (b) collapse-mode CMUT and (c) pre-charged collapse mode CMUT

collapse-mode [12].

An additional feature of these pre-charged CMUTs is their broadband performance which is not possible with bulk PZT transducers. The broadband performance is beneficial for an IMD for several reasons. First, depending on the depth of the implantation, the operation frequency can be adjusted; for a deeper implant a lower frequency can be used, and for a miniature implant that requires accurate focusing, a higher frequency can be used. Secondly, by shifting the frequency, destructive interference at the CMUT can be avoided [10]. Finally, a communication link that exploits the broadband property of the pre-charged CMUT will allow communication strategies analogous to RF communication to be developed in the future.

In this work, first the CMUT was characterized through impedance measurements (Sec. 3.2) and impulse response measurements (Sec. 3.3). Subsequently, the efficiency was measured at low acoustic pressure for frequencies of 2.15 MHz and 5.85 MHz (Sec. 3.4) and for high acoustic pressure up to 0.6 MPa peak to peak at 2 MHz (Sec. 3.5). The efficiency was as high as 47 % showing that this pre-charged CMUT can be a suitable candidate for miniature IMDs in the future.

3.2. CHARACTERIZATION OF THE CMUT

The layer stack of the CMUT device is shown in Fig. 3.2. The pre-charged CMUT includes a 200 nm thick Al_2O_3 for the charge storage layer between the top and bottom electrode. In this work Al_2O_3 layer was used as the charge storage layer for its known charging capabilities, however it is possible to use other charging dielectrics such as Si_3N_4.

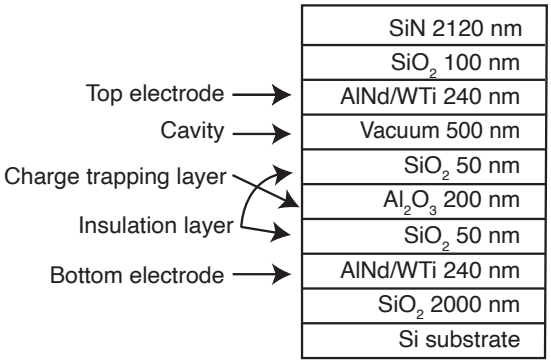

Figure 3.2: Layer stack of the pre-charged collapse mode CMUT

Fig. 3.3 is the optical microscope view of the CMUT, showing part of the 56 rows and 128 columns of CMUTs that were fabricated. The device was mounted on a PCB where every 6 columns were connected in parallel to a single SMB connector. Therefore, one SMB connector was connected to a surface area of 6.3 mm^2 (0.84 mm × 7.56 mm).

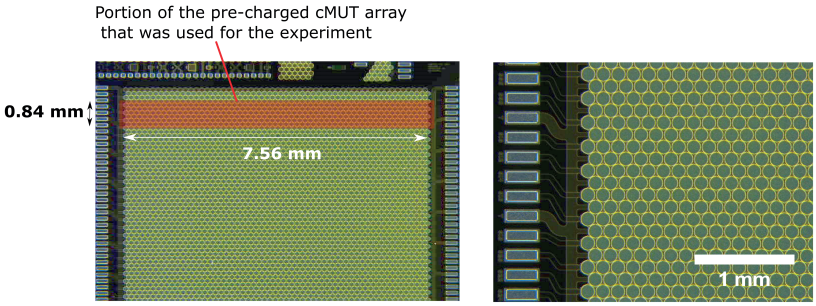

Figure 3.3: Optical Microscope picture of the CMUT

Fig. 3.4 shows the impedance spectrum of 6 elements of these CMUTs measured in air. The impedance spectrum was measured for different bias voltage using an impedance analyzer (Agilent 4294A Precision impedance analyzer) at 10 V steps from 0 V to 170

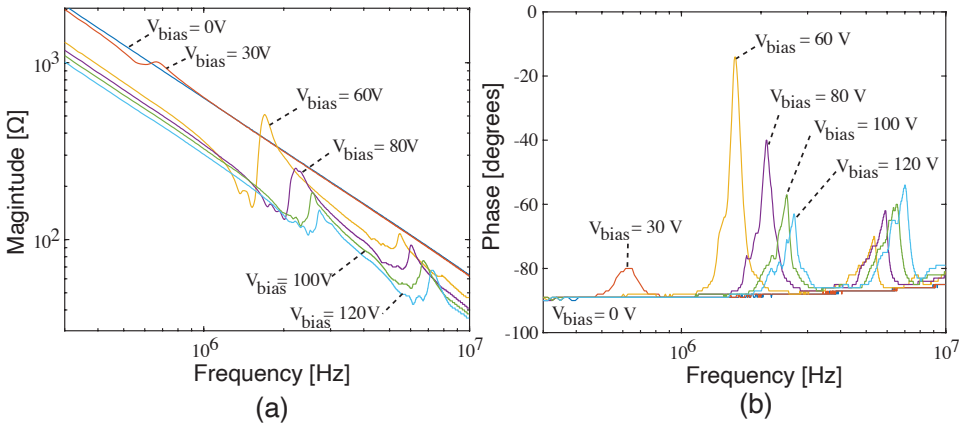

Figure 3.4: Impedance Spectrum of the CMUT in air for different bias voltage.

V. Calibration was done to the point of the SMB connection on the PCB using a short, open and 50 ohm load provided with the calibration kit from the manufacturer. Each impedance spectrum was taken within 10 seconds to avoid excess charging of the CMUT. At V_{bias} = 0 V the impedance of the CMUT shows a purely capacitive behaviour with a constant slope and a -90 degrees phase shift. As the voltage is increased a peak begins to appear below 1 MHz. Then when the bias is at 50 V, two peaks appear in the phase spectrum, along with a large capacitance increase. After collapse, the resonance shifts to 2 MHz and 5 MHz.

Fig. 3.5 shows the resonance frequencies extracted from the previous figure plotted as a function of the bias voltage. Prior to the collapse, the resonance frequency is decreasing. This is a common behaviour that is observed for non-collapse mode CMUTs. In a first order model, the resonance frequency (f_{res}) of the CMUT is determined by the mass and stiffness of the membrane (k) as $f_{res} = \frac{1}{2\pi}\sqrt{\frac{k}{m}}$. When the membrane is pulled closer to the bottom membrane the electric field becomes stronger which can be seen as a decrease in the stiffness of the membrane (spring softening effect [13]) resulting in a lower resonance frequency. Beyond the collapse voltage, two resonance frequencies appear where the 1st order resonance is at 2 MHz and the other at 5 MHz. As the bias voltage is increased, the resonance frequency also increases. Mainly due to the decrease in mass caused by the smaller vibrating donut region. At around 120 V, the 1st order resonance begins to saturate. This may be the effect of the charging of the CMUT which occurs at around 125 V.

Charging of the CMUT is done by applying an electric field across the dielectric stack strong enough to tunnel electrons through the SiO_2 layer into the Al_2O_3 layer. Our inves-

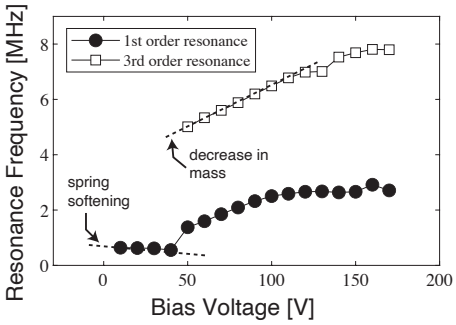

Figure 3.5: Resonance frequency against the bias voltage

tigation begins by determining the appropriate bias voltage and bias duration to charge the CMUTs. Beginning from a pristine CMUT, the bias voltage was increased starting from 50 V in 25 V increments. For each bias voltage, the bias was applied for a total of 10 min. Intermittently, the CMUT was removed from the bias voltage and the impedance spectrum was measured to see if a resonance frequency appeared without bias. Prior to each impedance measurement the two terminals of the CMUT were shorted to remove any stray charges on the top or bottom electrode. Table 3.1 shows the resonance frequency measured with the impedance analyzer. When two resonance frequencies appeared, only the lower resonance frequency is listed in this table. The results for charging voltages of 50 V to 100 V are not shown in this table because there were no charges trapped and the CMUT remained purely capacitive, thus without any resonance frequency. After each bias voltage was applied, in order to pull the CMUT out of collapse-mode a high AC voltage (60V) was applied to bring the CMUT to a non-collapsed state. Since this process does not completely discharge the CMUT, the CMUT still remained in resonance even at 0 V in the following charging step (i.e. charge voltage 175 V and 200 V). However, since the voltage steps are taken large enough, it is assumed that the previous charging is insignificant when the next bias voltage is applied.

From Table 3.1, it can be seen that charge trapping begins at a voltage and charge time of 125 V and 300 s respectively which resulted in a resonance frequency of 647 kHz in the non-collapsed state. Then the voltage and the charge duration was incrementally increased in 25 V steps. In Table 3.1, it can be seen that at 150 V and 30 s the CMUT in permanent collapse-mode which is shown by the large increase in the resonance frequency beyond 1 MHz. As the charge voltage and the charge duration is increased the resonance frequency also increases. In table 3.1 the second column from the right shows the electric field strength. This electric field is calculated within the SiO_2 layer. Many works done

in the past for floating gate MOSFETs have shown that in order to tunnel charges through SiO_2 the electric field must be in the Fowler-Nordheim tunneling regime, which is typically beyond 5 MV/cm. Therefore, the electric field used in this work is strong enough to tunnel charges through the oxide layer.

Table 3.1: Resonance frequency shown as a function of charge time and charge voltage. The shadowed region in red shows when the CMUT was kept in collapse mode after charging the device. The electric field is calculated by dividing the charge voltage by the effective SiO_2 layer thickness of 200 nm.

		Charge Time [second]							
		0	0.1	1	5	30	60	300	600
Voltage [V]	E [MV/cm]	Resonance Frequency [MHz]							
125	6.25	0	0	0	0	0	0	0.647	0.647
150	7.5	0	0.647	0.622	0.573	1.29	1.29	1.39	1.39
175	8.75	0.622	1.394	1.64	1.82	1.94	1.94	2.07	2.07
200	10	0.647	2.04	2.24	2.31	2.36	2.34	2.41	2.39

3.3. BANDWIDTH OF THE CMUT

Until now, the CMUT has been characterized in air. However, when the CMUTs are operated in water, the large damping caused by water broadens the resonance peak decreasing the quality factor. Two methods can be used to measure this bandwidth. The first option is to measure the impedance spectrum of the CMUTs in water. Unfortunately the measured spectrum was too sensitive to parasitic elements (i.e. track inductance) and therefore did not work. As an alternative, the bandwidth of the CMUT was measured acoustically. Fig. 3.6 shows the setup used for the hydrophone measurements. An optical hydrophone (Precision Acoustics) was positioned 2.6 mm in front of the CMUT which is within near field region for the transducer. Then an impulse signal was applied and the acoustic pressure was measured. The impulse signal used for this work was a 25 ns pulse with an amplitude of 25 V as shown in Fig. 3.7. This corresponds to half a wavelength of 20 MHz which is much higher than the frequency of interest, which is important for an impulse response measurement.

Fig. 3.8 summarizes the results from the impulse response measurements. In the first column, the transient waveform of the impulse response is shown and in the second column the corresponding bandwidth is shown. The bandwidth was calculated by taking the Fourier transform of the impulse response and by correcting the result for the input signal and the sensitivity of the hydrophone. Fig. 3.8 (A-a) to (A-e) shows the transient impulse response measured for the uncharged CMUT. A positive impulse signal was applied for each measurements and only the bias voltage was incrementally

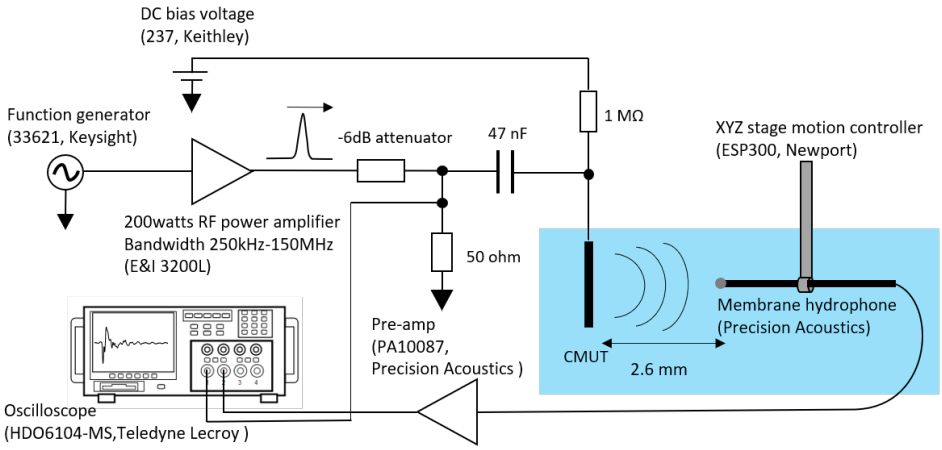

Figure 3.6: Setup to measure acoustic pressure for the CMUT.

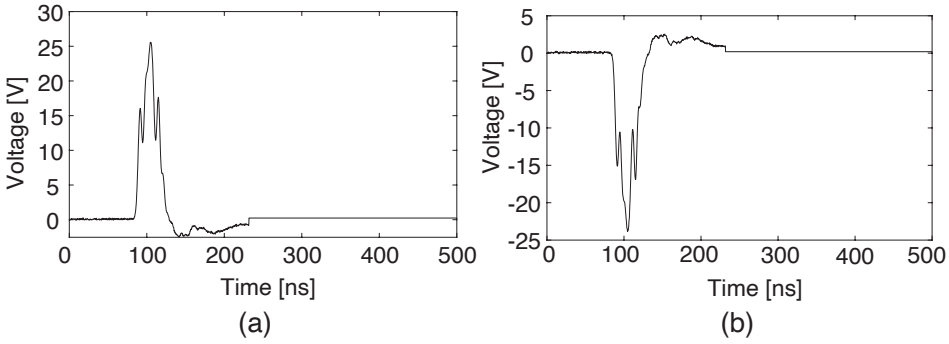

Figure 3.7: Positive and Negative impulse signal

increased from 60 V to 100 V in 10 V steps. Looking at the waveform of the transient signal, a negative peak appears first which is followed by a positive peak. This is because the CMUT was first brought into collapse by the bias voltage and was further pulled into collapse by the additional impulse signal which in turn generates a negative pressure. This method of driving the CMUT is often referred to as an additive pulse, because the external bias voltage and the additional AC voltage have the same polarity. We also see that the peak amplitude increases when the bias voltage increases. This is due to the stronger electric field between the top and bottom electrode.

In comparison, Fig. 3.8(A-f) and (A-g) show the transient response for the pre-charge CMUT when a negative and a positive impulse signal was applied respectively. The

amount of charging within the CMUT was measured prior to the experiment to be nearly equivalent to 80 V using an impedance analysis. Interestingly, the transient pressure is additive for the negative impulse (Fig. 3.8(a)), while for the positive impulse it is subtractive (Fig. 3.8(b)). The mechanism behind this was modeled in Chapter 2. But to briefly explain, the charge layer should be thought as a dipole. The dipole direction is controlled by the initial charging process and acts against the charging voltage. In this work the charging voltage was applied in the same direction as the bias voltage. Therefore, once the charging voltage is removed, the dipole is strong enough to bring the CMUT into collapse but effectively acting as a negative external voltage. As a result, the negative impulse signal is now working additively to the internal charge while the positive impulse signal is acting subtractively. The -6dB bandwidth and the center frequency for each CMUTs are summarized in Table 3.2. In this table, f_1 and f_2 are the left side and the right side of the bandwidth, which is where the dashed line and the spectrum crosses over in Fig 3.8(B). The center frequency (f_c) is the average of the two frequencies. The bandwidth is calculated from $(f_2 - f_1)/f_c$. From Table 3.2, it can be seen that the center frequency increases as the bias voltage increases. Furthermore, the bandwidth is consistently beyond 100 %, which demonstrates the broadband property of CMUTs.

Table 3.2: -6 dB Bandwidth of the CMUT.

Bias Voltage [V]	f_1 [MHz]	f_c [MHz]	f_2 [MHz]	-6dB Bandwidth [%]
60	1.93	4.74	7.54	118
70	2.07	5.0	7.93	117
80	2.1	5.8	9.5	128
90	2.6	6.2	9.75	115
100	2.71	6.31	9.9	114
pre-charged CMUT (negative)	2.2	5.1	7.9	113

3.4. LOW PRESSURE ULTRASOUND POWER TRANSFER

Fig. 3.9 shows the equivalent electrical circuit model when ultrasound is being received by the CMUT. This first order model is sufficient to explain the concept of ultrasound power transfer used in this work.

In this model the ultrasound source is shown as a voltage source. The mechanical branch consists of a resistor (R_m), capacitor (C_m) and an inductor (L_m) connected in series. R_m corresponds to the medium impedance of water, C_m and L_m represent the mechanical resonance behaviour of the CMUT. The electrical branch consists of the electrical capacitance of the CMUT (C_e). According to the maximum power transfer theorem, the load must be the complex conjugate of the source impedance. The first require-

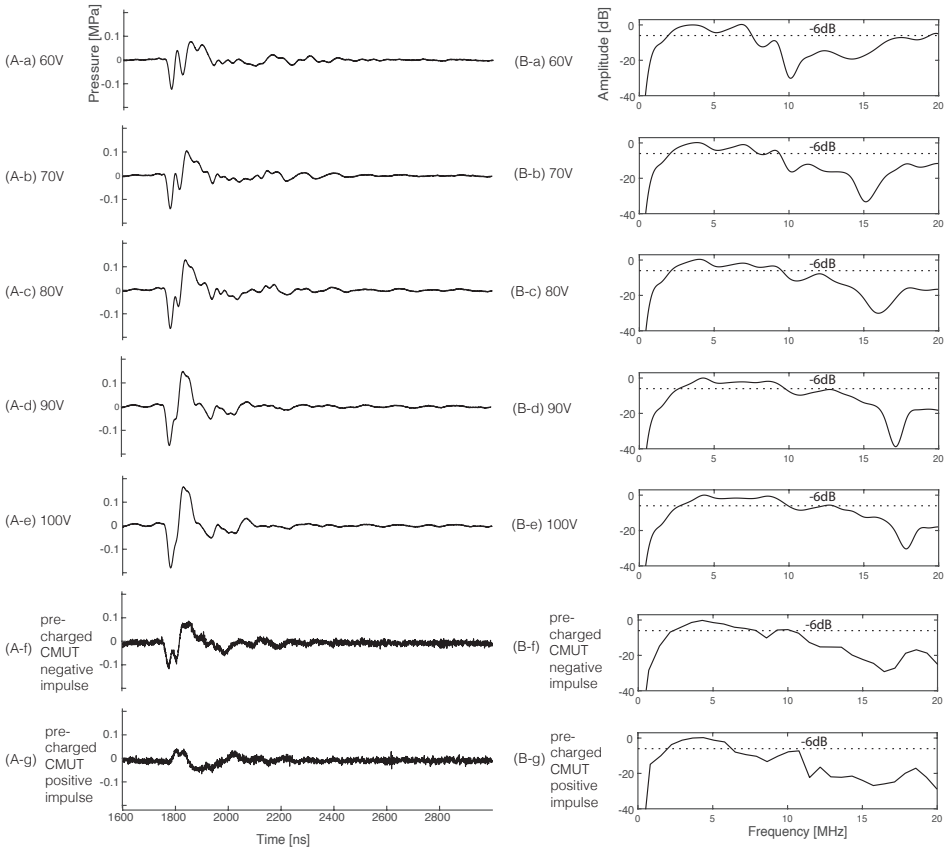

Figure 3.8: A) Transient response and B) Bandwidth of the CMUT for different bias voltages (a) 60 V (b) 70 V (c) 80 V (d) 90 V and (e) 100 V (f) pre-charged CMUT driven with a negative impulse (g) pre-charged CMUT driven with a positive impulse.

ment is to drive the ultrasound source at the resonance frequency of the CMUT where $f_{res} = \frac{1}{2\pi\sqrt{L_m C_m}}$. In this condition L_m and C_m cancel eachother out simplifying the mechanical branch to R_m. Then, by choosing an appropriate matching inductor (L_{match})

$$L_{match} = \frac{1}{(2\pi f_{res})^2 C_m} \tag{3.1}$$

the electrical capacitance C_e can be compensated. Therefore, the parallel connection of L_{match} and C_e effectively becomes an open circuit. As a result the equivalent circuit reduces to a voltage source with a source impedance of R_m and a load impedance of R_{load}. Finally, by choosing, $R_{load} = R_m$ maximum power transfer is achieved.

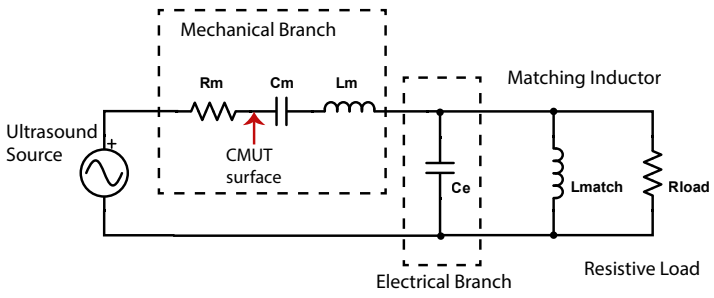

Figure 3.9: Equivalent circuit model during ultrasound power transfer using a CMUT.

In an actual use case, the electrical load is not matched to the ultrasound source. For example, the electrical load may consist of full bridge rectifiers which will introduce non-linear elements that will degrade the efficiency of the power transfer. Under these circumstances, an impedance matching scheme should be used to match the source impedance to the load impedance as much as possible. In this work we restrict ourselves to the ideal scenario in which the electrical impedance can be adjusted to maximize the power transfer.

Figure 3.10 shows the experimental setup to characterize the maximum power transfer. On the left is the PZT ultrasound transducer where two frequencies were tested (i.e. 2.15 MHz and 5.85 MHz). On the right side is the pre-charged CMUT at 70.4 mm distance for 2.15 MHz and 176 mm for 5.85 MHz. The PZT and the CMUT were carefully aligned using micromanipulators so that the natural focus of the PZT was at the surface of the CMUT. A burst signal was applied to the PZT transducer with an amplitude of 40 V and 10 cycles at a pulse repetition frequency of 10 kHz. The electrical capacitance (C_e) of the pre-charged CMUT was extracted from the impedance spectrum, which was 465 pF. Based on this Eq. 3.1, the L_{match} required to tune out Ce at 2.15 MHz and 5.85 MHz was 9.1 µH and 1.3 µH, respectively.

Finally, R_m must be equal to R_{load} for maximum power transfer. This was found by sweeping R_{load} using a potentiometer and by looking for the maximum power point. The power consumed at R_{load} was calculated from:

$$P_{load} = \frac{V_{pp}^2}{8R_{load}} \tag{3.2}$$

where, V_{pp} is the peak to peak voltage seen at the pre-charged CMUT. Fig. 3.11 shows the result of sweeping R_{load}. From this figure it can be seen that the maximum power

harvested at the pre-charged CMUT was 420 µW for 2.15 MHz and 780 µW for 5.85 MHz. The values used for R_{load} and L_{match} are summarized in Table 3.3. The power transfer efficiency was calculated by measuring the incoming power on the pre-charged CMUT by replacing the pre-charged CMUT with a hydrophone and by scanning the pressure profile over the pre-charged CMUT area. The measured intensity profile was integrated over the entire surface area of the pre-charged CMUT to obtain the incoming power. From this measurement, the incoming power was determined to be 975 µW and 1650 µW for 2.15 MHz and 5.85 MHz, respectively. The acoustic to electrical conversion efficiency was 43 % and 47 % for 2.15 MHz and 5.85 MHz respectively.

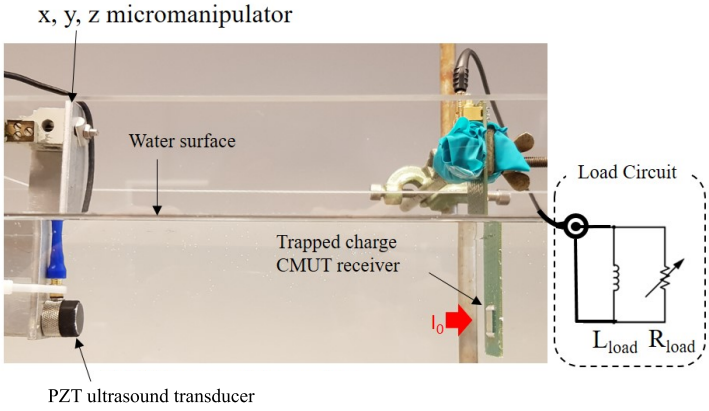

Figure 3.10: Ultrasound power transfer setup

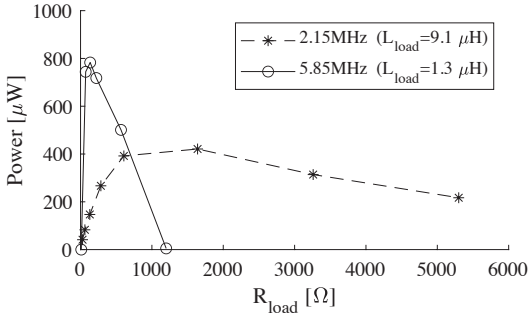

Figure 3.11: Maximum power point measurement with variable R_{load}

3.5. HIGH PRESSURE ULTRASOUND POWER TRANSFER

In this section, the ultrasound pressure was increased to see how this affects the overall efficiency of the device. The experimental setup is shown in Fig. 3.12(a) and a schematic of the setup is shown in Fig. 3.12(b). In this experiment, ultrasound was generated by a transmitter (TX) CMUT (5 mm x 12 mm) which operates in collapse-mode with a bias voltage with an acoustic frequency of 2 MHz generating up to a peak to peak pressure of up to 0.6 MPa, immediately in front of the receiver (RX) pre-charged CMUT. The RX had a surface area of 7.56 mm x 0.95 mm and the distance between the TX and RX was 6 cm which was chosen so that the ultrasound will hit the pre-charged CMUT array with a plane wave. This guaranteed that all of the devices would operated in-phase with the same voltage. To avoid standing wave formation between the TX and the RX, the ultrasound was sent in 10 cycle at 1 kHz burst rate. The output of RX was connected to an adjustable impedance matching block directly connected on the same PCB as shown in Fig. 3.12(a). This block is composed of several inductors and resistors which can be manually reconnected with mechanical switches. The alignment of RX with respect to TX was adjusted by positioning RX so that the maximum output voltage was achieved in an open circuit condition.

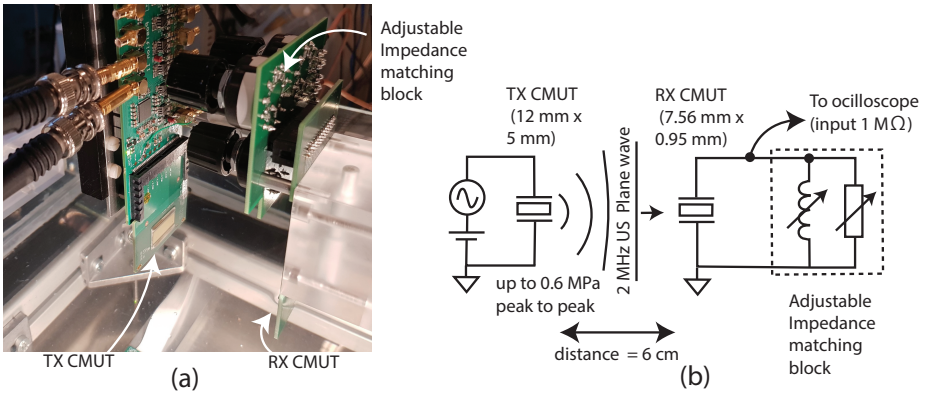

Figure 3.12: High acoustic output pressure power transfer

The adjustable impedance block was tuned similarly to Section 3.4. First the output voltage was measured at RX in open circuit condition for three incident pressure values (see Fig. 3.13(a) the line with circle markers). Next the inductive load was tuned to maximize the output voltage in order to compensate the electrical capacitance of the CMUT (see Fig. 3.13(a) the line with triangle markers). The inductance value at matched condition was 10 µH which is in well agreement with the analytically calculated value of

L_{match} = 9.89 µH, according to Eq. 3.1 (∵ C_e = 640 pF, f_{res} = 2 MHz). Finally, the matching resistor load was adjusted to R_{load} = 360 Ω to achieve maximum power transfer (see Fig. 3.13(a) the line with square markers). In this matched condition, the efficiency of the CMUT was calculated for the three pressure values as shown in Fig. 3.13(b). From the figure it can be seen that, the efficiency decreases as the pressure increases.

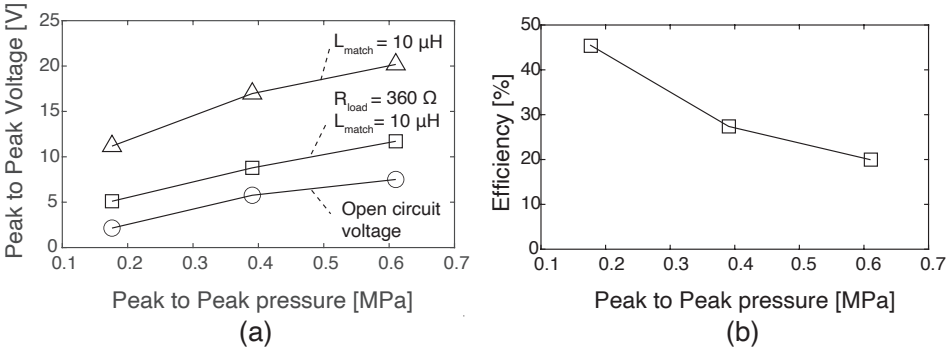

Figure 3.13: (a)The output voltage measured at the receiver for varying loading conditions and (b)the efficiency measured for matched load condition (R_{load} = 360Ω and L_{match} = 10 µH). Both figures are plotted with respect to the incident peak to peak pressure.

Table 3.3: Summary of ultrasound power transfer measurement

f_{US} [MHz]	Distance [mm]	Area [mm^2]	C_e [pF]	R_{load} [Ω]	L_{match} [µH]	Pressure Peak to Peak	Harvested power	Incoming power	Efficiency
2.15	70.4	6.3	465	1640	9.1	0.1 kPa	420 µW	975 µW	43 %
5.85	176	6.3	465	130	1.3	0.14 kPa	780 µW	1650 µW	47 %
2	60	7.2	620	360	10	0.17 MPa	9 mW	20 mW	46 %
2	60	7.2	620	360	10	0.39 MPa	27 mW	97 mW	27 %
2	60	7.2	620	360	10	0.61 MPa	47 mW	237 mW	20 %

3.6. DISCUSSION

Table 3.3 summarizes all of the measurement results in this work. For lower acoustic pressure (= 0.17 MPa), the efficiency of the pre-charged CMUT was found to be 46 %. Therefore, there is a conversion loss of 54 % from the acoustical domain to the electrical domain. We speculate that this loss is mainly due to the limited active surface area of the collapse-mode CMUT. To further explain, Fig. 3.14 shows the layout of the pre-charged CMUT used in this work seen from above. From this figure, the surface area can be divided into 3 parts. The first part is the rigid collapsed region of the CMUT at the center of the membrane which accounts for about 2% to 25 % depending how deep the CMUT

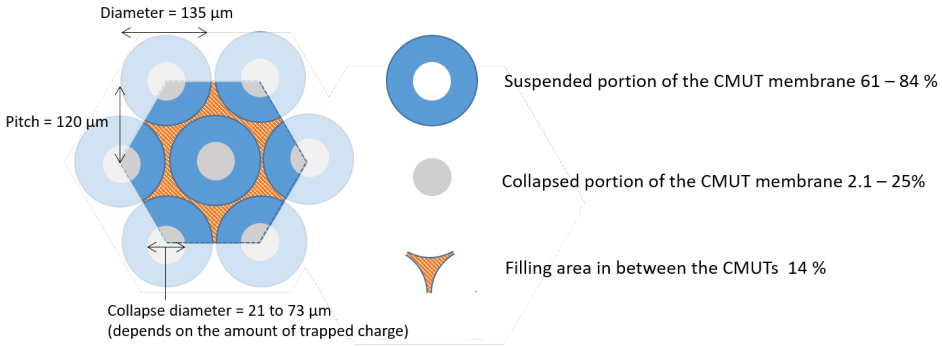

Figure 3.14: Surface area of the CMUT and its ratio of the suspended portion, collapse portion and the filling area of the CMUT

is in collapse. The second part is the filling area in between the CMUT membrane which is 14%. The last part is the suspended donut shaped portion of the membrane which is about 61% to 84%. The active area of the CMUT is the suspended portion and therefore, when ultrasound hits the other part of the CMUT this would incur a 20% to 40 % loss. Additional mechanisms of losses could be, i) scattering of ultrasound within the Si substrate, ii) electrical mismatch and, iii) the non-linear behaviour of the CMUT. For pressures beyond 0.17 MPa peak to peak the efficiency drops due to this non-linear behaviour of the CMUT.

Table 3.4 compares our work to the results from others. The performance of the pre-charged CMUT is comparable to PZT transducers[14], and it outperform most of the other ultrasound technologies. As an exception, there is the exceedingly high efficiency (over 300 %) that was reported by [15] which is due to the small cubed PZT element form factor that can receive ultrasound through multiple surfaces. However, the main limitation of using PZT is that it is lead-based and not bio-compatible. Therefore, for safe usage it is required to use a hermetic encapsulation that is acoustically penetrable as was shown in [16]. Yet this will greatly reduce the acoustic to electric conversion efficiency. Furthermore, this will also make it impossible for the PZT to operate in multiple vibrational modes. In comparison, the pre-charged CMUTs perform as well as the PZT and do not require an hermetic encapsulation because of the bio-compatible materials that are used. In all fairness it should be noted that $BaTiO_3$ is also biocompatible and can have an efficiency as high as 37 % which is an attractive material for IMDs. The additional advantage of pre-charged CMUTs is the flexibility to design small or large transducer arrays, and that they can be mass produced through standard IC-based fabrication techniques. In the future, one could easily imagine a fully monolithic integration of CMUTs

with ASICs which is attractive for mm-size implants. However, there remains one issue for these mm-size implants, which is the relatively large matching inductor that needs to be added externally. In addition, a secondary problem caused by the inductor is that the inductor and the electrical capacitance of the CMUT effectively acts as a band pass filter which has a smaller bandwidth than the mechanical bandwidth of the CMUT. Therefore, removing the need for a matching inductor by designing a CMUT with a smaller electrical capacitance should be a focus for future work.

3.7. APPLICATION EXAMPLES

With several mW of power transferred through water there are numerous things that can be done. To demonstrate some applications using ultrasound power transfer we created several demonstration videos. The first video[1] is an LED powered by using ultrasound over a meter of distance through water. The second video[2] is a RSL10 Bluetooth module (Onsemi) powered by with ultrasound power. The RSL10 module works with few mW and has various sensors (i.e. pressure sensor, temperature sensor, supply readout) which can communicate the information to any smart phone through a Bluetooth connection. Finally, the last video shows an example of using ultrasound to stimulate a nerve extracted from a worm [3]. Here we show a potential application where completely passive nerve stimulation is possible.

3.8. CONCLUSION

In this work we have shown that the ultrasound reception of pre-charged CMUT performance is comparable to PZT performance and will not require an external DC bias voltage nor a hermetic encapsulation because of its biocompatibility, making it exceptionally suitable for IMD applications. This work began by first characterizing the CMUTs using impedance analysis in air to determine the baseline behavior of the CMUTs before charges were trapped inside. Then the CMUT's charging behaviour was characterized which showed that applying an electric field as high as 7 MV/cm to 10 MV/cm will tunnel charges into the Al_2O_3 layer which will initiate charge trapping. The bandwidth of these devices was measured through an impulse response measurement showing that they have more than 100 % bandwidth (-6 dB) which spans from 2 MHz to 8 MHz. Finally, ultrasound power transfer measurements were conducted at both low and high pressure using two separate apparatuses. It was shown through these experiments that

[1] CMUT power transfer: https://www.youtube.com/watch?v=v-0rAPP2ZGE
[2] Ultrasound power transfer in Moore4Medical: https://youtu.be/$_c wph0Kv0i0$
[3] Ultrasound powered nerve stimulation: https://www.youtube.com/watch?v=wAVtjuyzapg

if the incident pressures is lower than 0.17 MPa peak to peak, the acoustic to electric conversion efficiency reaches 46%. For higher pressures, the efficiency decreases due to the non-linear behavior of the CMUT but even at 0.6 MPa peak to peak the efficiency is still 20 %. The ultrasound power that can be received on a surface area of 7.1 mm^2 can easily go up to several mW while still keeping below the FDA limit of 720 mW/cm^2. This conversion efficiency is comparable to conventional PZT technology and substantially out performs most of the other ultrasound technologies reported in literature (see Table 3.4).

Table 3.4: Comparison to state of the art work on ultrasound power transfer.

	Transducer type	lead-based ?	Dimension	I_{rc} [mW/cm^2]	Freq [MHz]	Power output [mW]	Power density [mW/cm^2]	Efficiency [%]	Depth [mm]	Medium	Rectified ?	Source
1	$BaTiO_3$ Plate	No	1.65 x 1.65 x 1.5	290	1.3	NR	110	37.9	105	Castor oil	Yes	[4]
2	AlN diaphragm array	No	8 x 8 x 0.3	77	2	0.001	0.007	0.009	40	Water	No	[11]
3	0-3 $BaTiO_3$ / PLGA composite	No	1 x 1 x 0.012	65	2.3	1	1	1.5	10	Water	No	[17]
4	PZT Plate	Yes	1 x 1 x 1.4	100	1	0.4	40	40	27	Ex-vivo tissue	No	[14]
5	PZT Plate	Yes	0.75 x 0.75 x 0.75	6.62	1.85	0.147	26	390	48	Gel	No	[15]
6	PZT Diaphragm	Yes	4 x 4	74.8	0.088	0.7	17.5	23	20	Water	No	[8]
7	PZT Plate array	Yes	21 x 21 x 2	65	0.35	0.0176	0.004	0.006	23	Water	No	[18]
8	Pre-charged CMUT	No	0.84 x 7.56 x 0.7	15.5	2.15	0.42	6.7	43	70.4	Water	No	
		No	0.84 x 7.56 x 0.7	26.2	5.85	0.78	12.4	47	176	Water	No	**Our work**
		No	0.91 x 7.56 x 0.7	260	2	9	125	46	60	Water	No	**Our work**
		No	0.91 x 7.56 x 0.7	1270	2	26	361	27	60	Water	No	**Our work**
		No	0.91 x 7.56 x 0.7	3100	2	47	653	20	60	Water	No	**Our work**

[1] Dimension : Width x Length x Thickness
[2] I_{rc} : Incident intensity on the transducer
[3] Power Output : Power dissipated at the load
[4] Power density : Power Output / receiver area
[5] Efficiency : Power density / I_{rc}

BIBLIOGRAPHY

[1] A. Ballo, M. Bottaro, and A. D. Grasso, "A Review of Power Management Integrated Circuits for Ultrasound-Based Energy Harvesting in Implantable Medical Devices", 2021. DOI: 10.3390/app11062487. [Online]. Available: https://doi.org/10.3390/app11062487.

[2] D. H. Toffa, L. Touma, T. El Meskine, A. Bouthillier, and D. K. Nguyen, *Learnings from 30 years of reported efficacy and safety of vagus nerve stimulation (VNS) for epilepsy treatment: A critical review*, Dec. 2020. DOI: 10.1016/j.seizure.2020.09.027.

[3] J. Z. Lee, S. K. Mulpuru, and W. K. Shen, *Leadless pacemaker: Performance and complications*, Feb. 2018. DOI: 10.1016/j.tcm.2017.08.001.

[4] J. Charthad, S. Member, T. C. Chang, *et al.*, "A mm-Sized Wireless Implantable Device for Electrical Stimulation of Peripheral Nerves", *IEEE Transactions on Biomedical Circuits and Systems*, vol. 12, no. 2, pp. 257–270, 2018. DOI: 10.1109/TBCAS.2018.2799623.

[5] K. Kim, S. G. Jang, H. G. Lim, H. H. Kim, and S. M. Park, "Acoustic Power Transfer Using Self-Focused Transducers for Miniaturized Implantable Neurostimulators", *IEEE Access*, vol. 9, pp. 153 850–153 862, 2021, ISSN: 21693536. DOI: 10.1109/ACCESS.2021.3127875.

[6] A. Iqbal, P. R. Sura, M. Al-Hasan, I. B. Mabrouk, and T. A. Denidni, "Wireless power transfer system for deep-implanted biomedical devices", *Scientific Reports*, vol. 12, no. 1, p. 13 689, Aug. 2022, ISSN: 2045-2322. DOI: 10.1038/s41598-022-18000-6. [Online]. Available: https://www.nature.com/articles/s41598-022-18000-6.

[7] M. J. Karimi, A. Schmid, and C. Dehollain, *Wireless Power and Data Transmission for Implanted Devices via Inductive Links: A Systematic Review*, Mar. 2021. DOI: 10.1109/JSEN.2021.3049918.

[8] H. Basaeri, D. B. Christensen, and S. Roundy, "A review of acoustic power transfer for bio-medical implants", *Smart Materials and Structures*, vol. 25, no. 12, 2016, ISSN: 1361665X. DOI: 10.1088/0964-1726/25/12/123001.

[9] K. Shen and M. M. Maharbiz, "Design of Ceramic Packages for Ultrasonically Coupled Implantable Medical Devices", *IEEE Transactions on Biomedical Engineering*, vol. 67, no. 8, pp. 2230–2240, 2020, ISSN: 15582531. DOI: 10.1109/TBME.2019.2957732.

[10] Q. Shi, T. Wang, and C. Lee, "MEMS Based Broadband Piezoelectric Ultrasonic Energy Harvester (PUEH) for Enabling Self- Powered Implantable Biomedical Devices", *Nature Publishing Group*, no. December 2015, pp. 1–10, 2016. DOI: 10.1038/srep24946. [Online]. Available: http://dx.doi.org/10.1038/srep24946.

[11] B. Herrera, F. Pop, C. Cassella, and M. Rinaldi, "AlN PMUT-based Ultrasonic Power Transfer Links for Implantable Electronics", *2019 20th International Conference on Solid-State Sensors, Actuators and Microsystems and Eurosensors XXXIII, TRANSDUCERS 2019 and EUROSENSORS XXXIII*, no. June, pp. 861–864, 2019. DOI: 10.1109/TRANSDUCERS.2019.8808320.

[12] J. Munir, Q. Ain, and H. J. Lee, *Reliability issue related to dielectric charging in capacitive micromachined ultrasonic transducers: A review*, Jan. 2019. DOI: 10.1016/j.microrel.2018.12.005.

[13] G. G. Yaralioglu, A. S. Ergun, B. Bayram, E. Hæggström, and B. T. Khuri-Yakub, "Calculation and measurement of electromechanical coupling coefficient of capacitive micromachined ultrasonic transducers", *IEEE Transactions on Ultrasonics, Ferroelectrics, and Frequency Control*, vol. 50, no. 4, pp. 449–456, 2003, ISSN: 08853010. DOI: 10.1109/TUFFC.2003.1197968.

[14] J. Charthad, M. J. Weber, T. C. Chang, and A. Arbabian, "A mm-Sized Implantable Medical Device (IMD) With Ultrasonic Power Transfer and a Hybrid Bi-Directional Data Link", *IEEE Journal of Solid-State Circuits*, vol. 50, no. 8, pp. 1741–1753, 2015, ISSN: 00189200. DOI: 10.1109/JSSC.2015.2427336.

[15] D. K. Piech, B. C. Johnson, K. Shen, *et al.*, "A wireless millimetre-scale implantable neural stimulator with ultrasonically powered bidirectional communication", *Nature Biomedical Engineering*, vol. 4, no. 2, pp. 207–222, 2020, ISSN: 2157-846X. DOI: 10.1038/s41551-020-0518-9. [Online]. Available: https://doi.org/10.1038/s41551-020-0518-9.

[16] K. Shen and M. M. Maharbiz, "Ceramic packaging in neural implants", *Journal of Neural Engineering*, vol. 18, no. 2, 2021, ISSN: 17412552. DOI: 10.1088/1741-2552/abd683.

[17] S. Selvarajan, A. Kim, and S. H. Song, "Biodegradable piezoelectric transducer for powering transient implants", *IEEE Access*, vol. 8, pp. 68 219–68 225, 2020, ISSN: 21693536. DOI: 10.1109/ACCESS.2020.2985993.

[18] L. Jiang, Y. Yang, R. Chen, *et al.*, "Flexible piezoelectric ultrasonic energy harvester array for bio-implantable wireless generator", *Nano Energy*, vol. 56, pp. 216–224, 2019. DOI: 10.1016/j.nanoen.2018.11.052.Flexible.

4

MICROWATT TELEMETRY WITH PRE-CHARGED COLLAPSE-MODE CMUTS

The simple things are also the most extraordinary things, and only the wise can see them.

Paulo Coelho, The Alchemist

4.1. INTRODUCTION

Autoimmune diseases or neuropathic disorders are conventionally treated with pharmacological interventions. In recent years, implantable medical devices, such as neural stimulator, have been shown to be effective for the treatment of such diseases [1]. Compared to pharmacological treatments that target the entire body, neural stimulation can be focused at the target location, enabling a selective therapy with fewer side effects [2]. Several groups have worked on mm-size implantable devices that target deep nerve innervation [3]–[5]. These mm-size deeply implanted medical devices use externally provided ultrasound power to operate.

Ultrasound is safe to use in the body, and has a high penetration depth and short wavelength, which enables a small focal point which is compatible with mm-size im-

Parts of this chapter have been published in IEEE IUS conference.

plants. However, establishing an efficient ultrasound power transfer link is still a challenge because a small angular misalignment leads to a drastic decrease in the available power [6]. The straight-forward approach to power a mm-size implant would be to rely on ultrasound imaging to obtain an accurate visualization of the implant position. However, the implant receiver for ultrasound has a limited angular sensitivity, which requires good alignment and precise beam steering. In addition, the orientation of the receiver cannot be easily interpreted from the ultrasound image. An alternative is to use time-reversal beamforming [7], [8]. This is a simple and computationally efficient method that can accurately focus acoustic energy regardless of tissue scattering or tissue inhomogeneity. However, this method does not provide an absolute measure of the power sent to the implant. As a result, a rapid feedback from the implant to the external transmitter is required to establish a power transfer link. This feedback can be in any form, either RF or ultrasound [9]. However, considering the significant attenuation of RF within the body, several milliwatts of power would be required to transmit a signal that can still be detected outside the body. As a consequence, substantial time would be required for the energy to be harvested at the implant, creating an impractical inherent delay in the feedback loop.

In this work, we present a circuit that uses ultrasound backscattering to feedback information on the received power. This circuit operates in the microwatt range, and it feed backs the voltage information on the storage capacitor of the implant within several milliseconds. Once the focus parameter is fixed, the algorithm tracks the location of the receiver to maintain a tight ultrasound power transfer link, in which case this proposed circuit can be turned off for other functionalities.

4.2. MICROWATT ULTRASOUND TELEMETRY PROTOCOL

Fig. 4.1 shows how the microwatt telemetry protocol works. In this circuit, RX is connected in parallel with a matching inductor, and a full bridge rectifier. The positive terminal of the full bridge rectifier is split into three terminals where the first terminal connects to the storage capacitance, the second terminal connects to the modulation switch and the third terminal connects to the modulation circuit. The details on how this modulation is applied at the circuit level will be explained in the following section. At a high-level, the protocol works by sending a paired interrogation bursts from the ultrasound probe (TX) towards the ultrasound receiver (RX) with a short interval between each signal (PRF = 1 kHz). Both signals are reflected on the surface of RX but only one of the signals is modulated after a time delay (τ) which encodes the voltage on the storage capacitance (V_c). The other signal, which is not modulated, is used as a reference

that samples the acoustic channel. Fig. 4.2 shows the demodulation process that is done on the MATLAB interface of the Verasonics system. Two consecutive signals that are received at the ultrasound probe are subtracted from each other and the pulse width is determined. The pulse width (PW) is related to the total duration of the burst (T_{burst}) and the time delay ($\tau(V_c)$) through the following equation,

$$PW = T_{burst} - \tau(V_c) \tag{4.1}$$

as a result $\tau(V_c)$ can be deterimined because PW and T_{burst} are known values. The key advantage in this protocol is that by using a differential signal, the communication channel will be robust to common-mode interference such as low-frequency artifacts (i.e. breathing, hand movements) and distortion caused by inhomogeneous tissue.

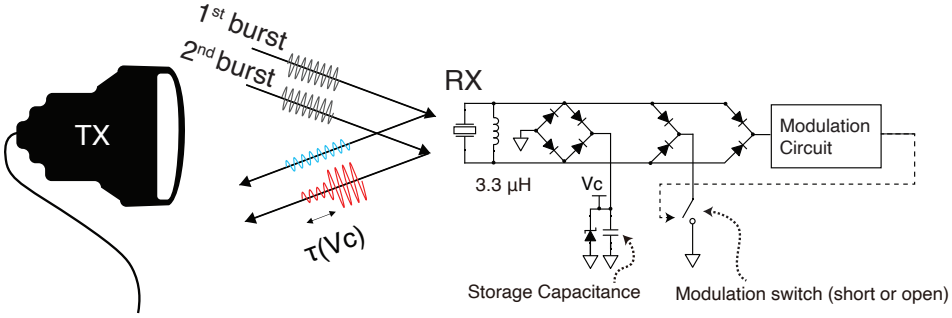

Figure 4.1: Microwatt telemetry circuit.

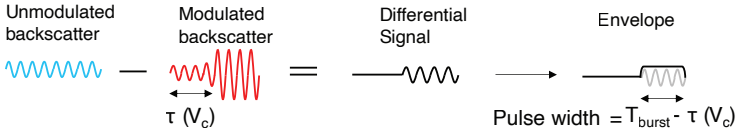

Figure 4.2: Microwatt telemetry circuit detection process.

4.2.1. MICROWATT TELEMETRY CIRCUIT ANALYSIS ON LT-SPICE

The modulation circuit must accomplish two tasks. Firstly, the delay (τ) has to be a function of the storage capacitance (V_c), and secondly, the modulation must be applied to every other burst. Fig. 4.3(a) shows the circuit diagram that was implemented. For the nodes labeled from A to G in this figure, the simulation result using LT-Spice (Linear Technology, USA) is shown in Fig. 4.3(b). In this circuit, the CMUT and the matching

inductor is replaced with a voltage source and a 400 Ω source impedance to emulate the incoming ultrasound. The incoming ultrasound voltage (node A) is a 4 MHz signal with 24 cycles at a 1 kHz PRF. The simulation result is magnified near the first 20 µs when the ultrasound is received at 1 ms and 2 ms. The modulation circuit begins by first using an RC bandpass filter (82 pF and 100 kΩ) to detect the envelope signal (node C) of the input voltage (node B). Subsequently, the envelope signal is rectified with a Schmitt trigger (NXP Semiconductor, 74AUP2G17GW) (node D) and connected to an RC low pass filter (LPF) which delays the signal. The time constant of the LPF is defined by a 100 kΩ resistor and two variable capacitance diode in parallel (NXP Semiconductor, BB202) resulting in a capacitance change from 20 pF to 60 pF. The reverse bias voltage to capacitance relation for a single variable capacitance diode is shown in Fig. 4.4(a) reproduced from the data sheet. The capacitance of the variable capacitance diode is modulated by the storage capacitance voltage (V_c) that is connected via a 1 MΩ resistor. After the envelope signal is delayed, the signal is connected to another Schmitt trigger to be rectified. This signal is then connected to the 1st input of the AND gate (NXP Semiconductor, 74AUP1G08GW). The output of the AND gate (node E) is connected to the gate of the modulation switch to modulate the backscatter signal with the modulated time delay. The modulation is applied to every other burst using a toggle flipflop (NXP Semiconductor, 74AUP1G08GW) that is connected to the 2nd input of the AND gate (node F). As a result, the drain of the modulation switch is shorted to ground after a delay $\tau(Vc)$ for every other ultrasound burst (node G).

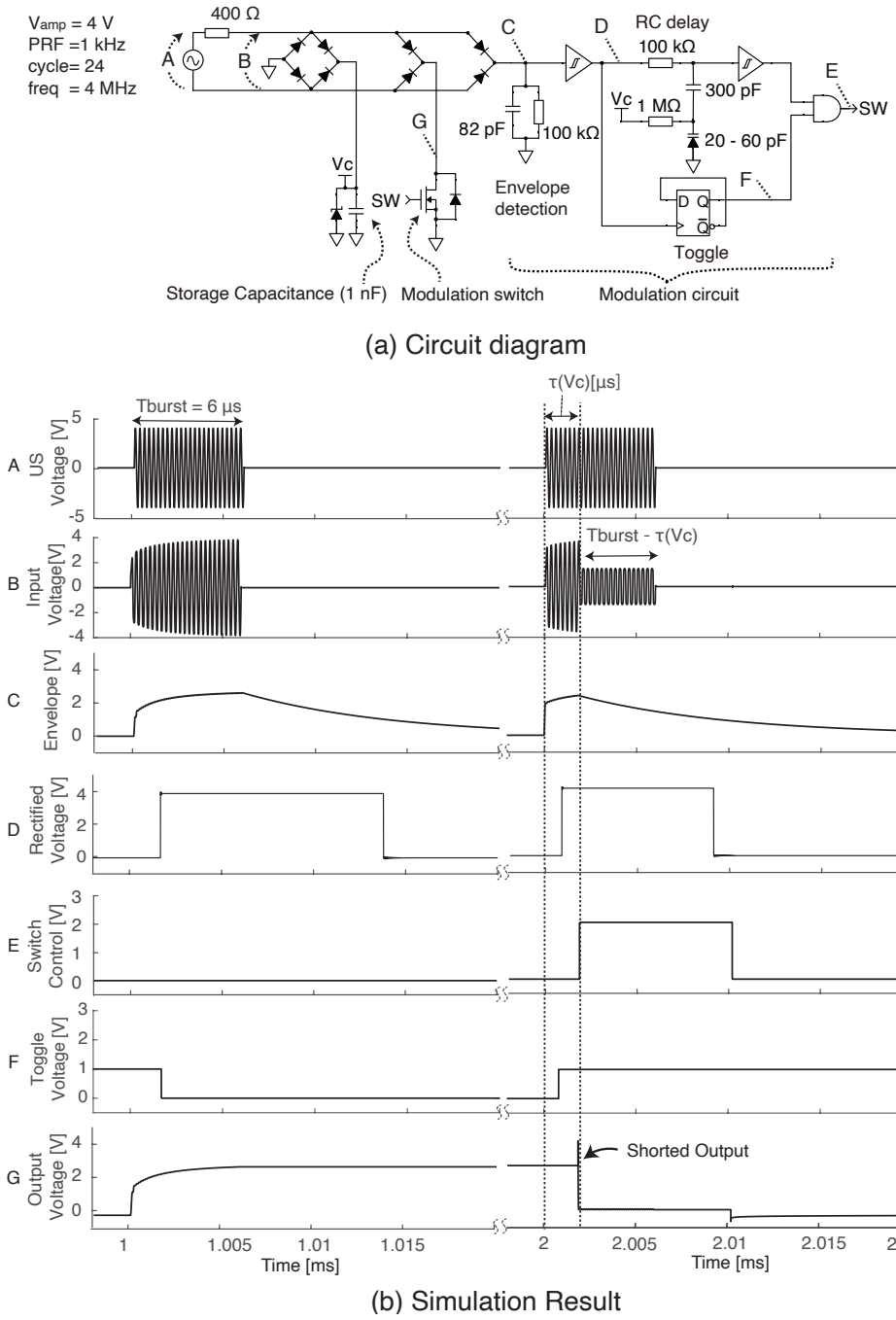

Figure 4.3: (a) Reference signal the signal is not modulated. (b) Modulated signal the MOSFET is turned on and the output voltage is shunted with a time delay τ [µs] which is a function of the storage capacitance voltage (Vc).

In the LT spice simulation, the source voltage amplitude was swept from 4 V to 6 V in several steps and τ was compared to V_c as shown in Fig. 4.4(b) in circle markers. The time delay decreases as the storage capacitance voltage increases. The dotted line shows $0.6{\cdot}100\,\text{k}\Omega{\cdot}2C_{\text{BB202}}(V_c)$ which is the time constant of the LPF multiplied with 0.6 which is a correction factor required to match the simulation result and the analytical result. In this circuit, all of the logic components are powered through the voltage on the storage capacitor and the complete circuit has a total current consumption of around 0.5 µA at 1 V operating voltage, thus only requiring microwatts of power consumption.

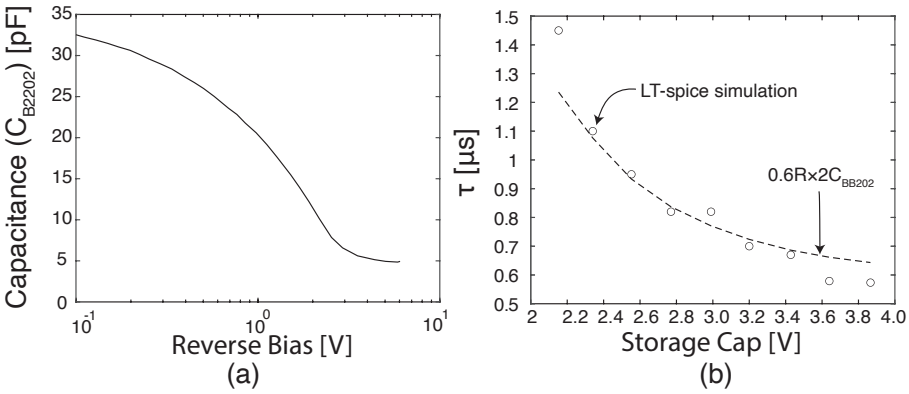

Figure 4.4: (a) The capacitance of the variable capacitance diode with respect to the reverse bias voltage. (b) The time delay τ as a function of the storage capacitance voltage.

4.3. ULTRASOUND BACKSCATTERING SETUP

Fig 4.5 (a,b) shows the experimental setup used to verify the microwatt telemetry protocol. A semicircular shaped gel phantom (Rayher Hobby GmbH) with a 100 mm radius was positioned between the ultrasound transmitter (Philips, L7-4 linear probe) and the capacitive micromachined ultrasonic transducer (CMUT) receiver (RX). The TX was mounted on a linear actuator to adjust the distance between The TX and RX. The RX was mounted on a rotary actuator to adjust rotational alignment between the TX and RX. The TX is 40 mm wide with 128 elements along the width and beam steering can be applied through the Verasonics Vantage system to adjust the focus along the y-z plane. Each element has a width of 0.28 mm and a height of 7 mm with a spacing of 25 µm between each element. The RX consists of 6 CMUT elements in parallel with a total size of 0.84 mm × 7.4 mm. The TX and RX were aligned in the x and y-axis direction using micromanipulator mounted on both sides of the setup. The alignment was tuned by maximizing the output voltage seen at the RX when TX was focused at (y, z) = (0 mm, 100 mm).

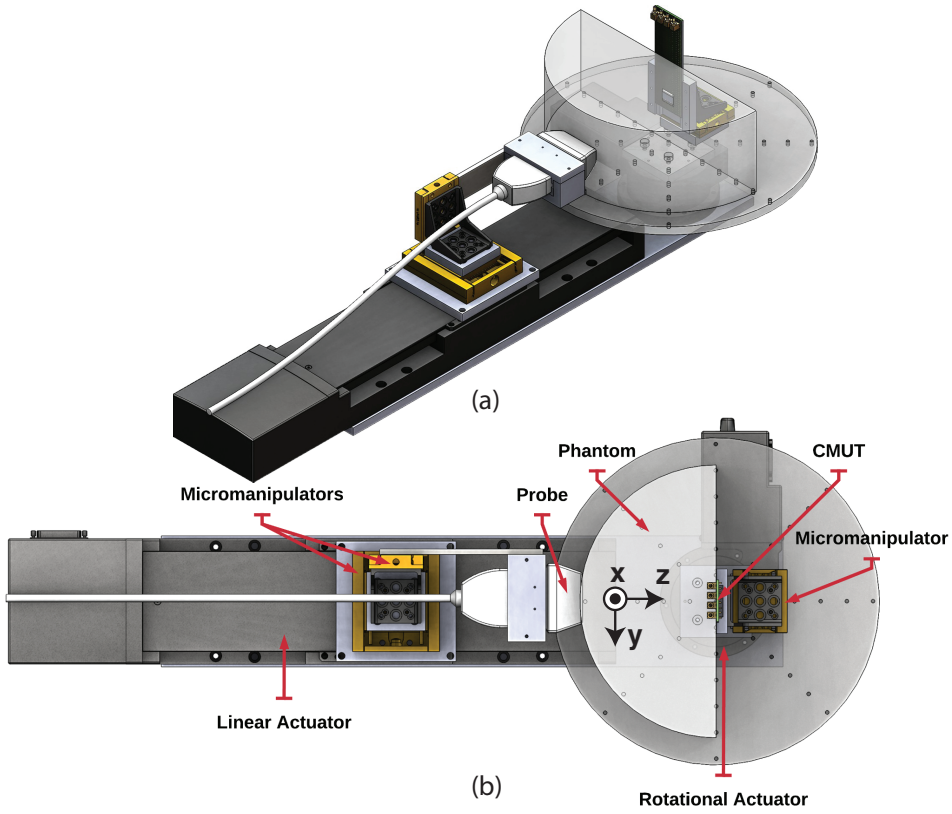

Figure 4.5: (a) Isometric view of the setup. (b) Top view of the setup. The ultrasound probe is mounted on a linear actuator and the CMUT is mounted on a rotary actuator. The gel phantom is shaped in a semicircular shape so the angle between the CMUT and the ultrasound probe could be adjusted while maintaining a constant distance. For aligning the system, the micromanipulators on both the CMUT and the ultrasound probe was used.

Fig. 4.6 shows this through an acoustic simulation result of the ultrasound field along (a) the y-z plane and (b) the x-z plane when The TX is focused at (y, z) = (0, 100 mm) towards the ultrasound receiver, which is also positioned at (y, z)=(0, 100 mm). The width and height of RX is represented with a red line respectively in both figures showing that the focal beam width and height are nearly identical to the width and height of the RX (see Fig. 4.6(a)). The length of the focal depth is quite long as shown in Fig. 4.6(b) and thus the focal depth is not as critical as the azimuth angle. Thus for this work even the slightess misalignment in the azimuth angle in the beam steering parameters will significantly degrade the acoustic power sent to the RX. Yet this setup and the later result will highlight the accuracy that can be achieved with the microwatt telemetry circuit. The microwatt telemetry circuit (Fig. 4.1) built for this work is shown in Fig. 4.8.

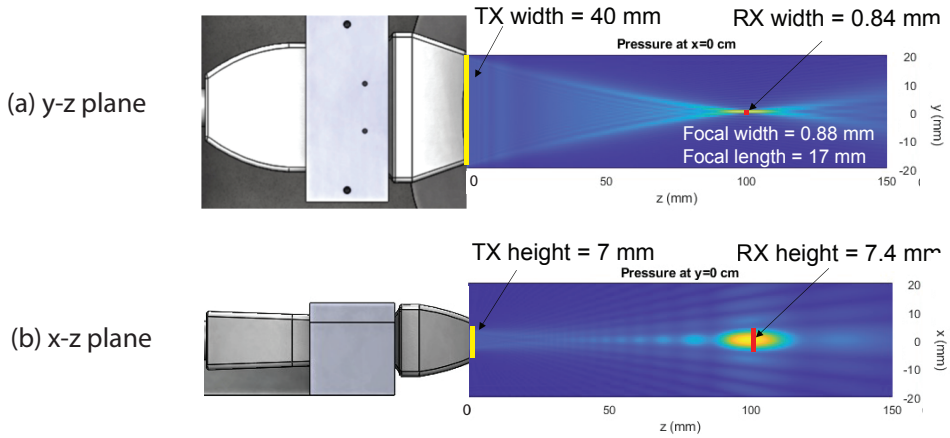

Figure 4.6: Ultrasound beam steered to (x,y,z) = (0 mm,0 mm, 100 mm) simulated on FOCUS. Two cross section along the (a) y-z plane and (b) x-z plane are shown in the figure. The red line corresponding to the size of the RX element.

The angular alignment between the TX and RX is critical in this work. For example, in the experimental setup shown in Fig. 4.6 the gel phantom was rotated and the angular acceptance of the CMUT was measured. The CMUT was optimally loaded with a matching inductor and a resistor. Fig. 4.7shows the result of this experiment. Since the measurement is sensitive to subtle misalignments, the measurement was performed 20 times and the average values were taken. Along with the measurement results the simulations based on FOCUS are also shown in the same figure. Both in the simulations and the measurements, the angular acceptance of the CMUT was approximately ± 10 degrees for a 50 % efficiency.

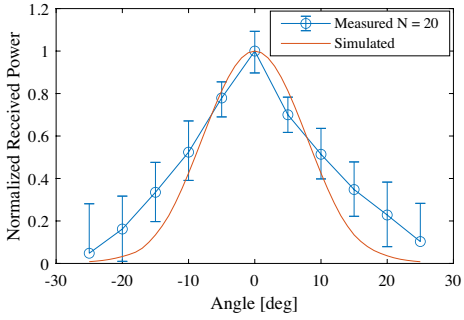

Figure 4.7: Angular acceptance of the CMUT.

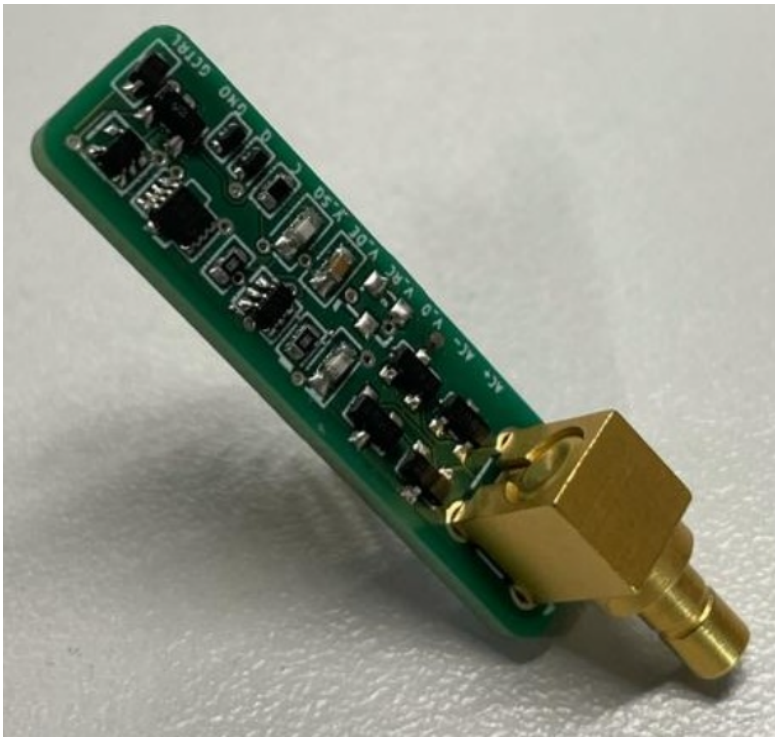

Figure 4.8: Assembled microwatt telemetry circuit.

4.3.1. SIMULATION ON FOCUS OF THE RECEIVED ULTRASOUND POWER

Fast Object-oriented C++ Ultrasound Simulation (FOCUS) is an ultrasound field simulator and some examples of the acoustic field simulation has already been shown in Fig. 4.6 [10], [11]. This simulator works by defining the TX geometry, the acoustic medium, the driving conditions and the grid on which the ultrasound is simulated. Since the simulation is based on the fast near field method, it can simulate a specific region of interest where in this case would be the surface of the RX. Building on this US simulator, the normalized received ultrasound power at the RX for different steering conditions was simulated.

The acoustic simulation was done in the following steps. First, the ultrasound probe was implemented with the appropriate geometry along with the acoustic gel phantom that was discussed in Section 4.3. Then in FOCUS a grid was defined where to caluclate the pressure. The surface of the RX was segmented into 6 rows and 56 columns resulting in a total of N = 336 pixels which is equivalent to the number of CMUT devices used in the RX. The pressure for each pixel is denoted as $P_{RX}(i)$ where i is a integer index number

between 1 to N referencing each pixel that was simulated. The pressure is simulated using continuous wave mode resulting in a complex value which includes both the real part and the imaginary part.

A common approach to calculate the total received power (I_{RX}) is to use the following formula,

$$I_{RX} \propto \sum_{i=1}^{N} P_{RX}(i) P_{RX}^{*}(i) \tag{4.2}$$

where the power is calculated at each pixel by multiplying it with the complex conjugate and is summed together. Unfortunately, this leads to an inaccurate result, because it continuously overestimated the received power mainly because the phase difference between independent CMUTs over the entire surface area of the RX is not taken into consideration. Thus, in this work we use an alternative approach. The acoustic pressure was averaged over the surface of the receiver.

$$P_{avg} = \frac{1}{N} \sum_{i=1}^{N} P_{RX}(i) \tag{4.3}$$

where P_{avg} is the average pressure impinging RX. The average value is representative of all the CMUT devices connected in parallel in the electrical domain. Finally, the averaged acoustic pressure was converted into the total received power by multiplying it with its complex conjugate value as,

$$I_{RX} \propto P_{avg} P_{avg}^{*} \tag{4.4}$$

This result is normalized and used to plot the total received power RX.

4.4. RESULT AND DISCUSSION

In this section, the operation of the microwatt telemetry circuit is discussed. Next, using the microwatt telemetry circuit, the acoustic power that is received at the implant will be mapped for different steering conditions and compared to the simulation result. Using this microwatt telemetry circuit, an active search algorithm was developed and presented in this work to show that accurate tracking of the implant can be conducted.

4.4.1. TESTING THE MICROWATT TELEMETRY CIRCUIT

Fig. 4.9(a,b), shows an example of the voltage signal seen at RX when US bursts (24 cycles, PRF = 1 kHz, f_{US} = 4 MHz) were sent from TX. The modulation can be seen in Fig. 4.9(b) where the backscattering circuit is shunting the output at a certain time after the start of the burst. Fig. 4.10(a) shows the backscattered ultrasound received at the US

probe, for the modulated signal and the unmodulated signal. The waves are severely distorted due to reflections and scattering in the phantom, and it is not straight forward to decipher the modulation at this state with most of the unmodulated signal overlapping the modulated signal. Nonetheless in the same figure, the differential signal and the envelope can be clearly distinguished which determines PW. In Fig. 4.10(b), the relation between the PW and the voltage on the storage capacitor is shown when an increasing pressure was generated from TX. As expected in this figure there is a monotonically increasing relation between the voltage on the storage capacitance and the PW.

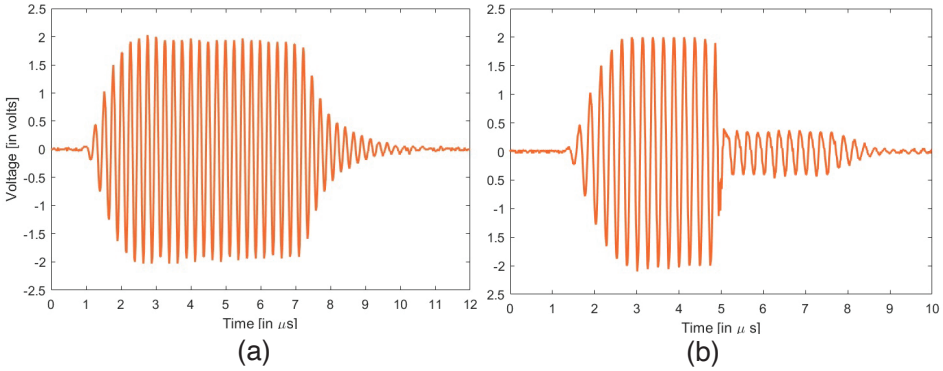

Figure 4.9: (a) Unmodulated and (b) modulated ultrasound voltage measured at the CMUT terminals.

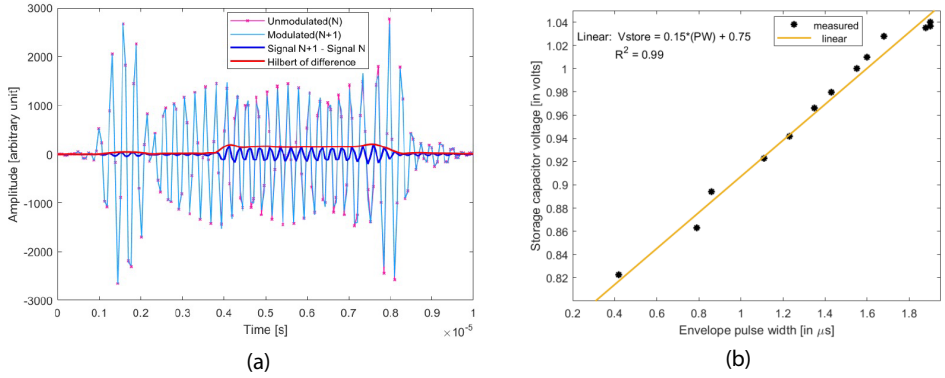

Figure 4.10: (a) Demodulation process of the signal. (b) Calibration of the voltage sensor.

4.4.2. MAPPING OUT THE RECEIVED ULTRASOUND POWER

The power received at the RX is mapped out by steering the beam from −2 mm to 2 mm along the y-axis and 80 mm to 150 mm in the z-axis in 55 steps in both axes. This corresponds to a spatial resolution of 0.07 mm and 1.27 mm along the y and z axes respectively. The measurement results and the simulation results are plotted in the form of a heat map in Fig 4.11(a,b) respectively. For the measurement results, each 2D coordinate on the plot shows the normalized PW for each beam steered coordinate. On the other hand for the simulation results, the normalized received power is plotted for each beam steering condition following the method explained in Section 4.3.1. From the measured heat map, RX can be located to be at a depth of 100 mm to 110 mm which compares well with the actual location of 100 mm. Observing the two figures, the measurement result has more noise compared to the simulation result. Furthermore, the simulated result is more smooth compared to the measurement result. This is due to the limited dynamic range of the backscattering circuit. This can also be seen in Fig. 4.11(c) and Fig. 4.11(d) that show the heat map evaluated at z = 100 mm and y = 0 mm, respectively. In both of these figures, the measurement result follows the simulation profile, as long as the normalized received power is above 0.4. If the normalized received power is lower than this, the measurement circuit does not have enough dynamic range to follow the simulated results. It is also noticeable that the measurement profile is slightly more elongated than the simulation results along the y = 0 cross section (Fig. 4.11(d)). This could be due to small rotational misalignments of the sample along the y axis. In addition, the spatial peak temporal average intensity (ISPTA) used in this work was 30 mW/cm^2, which is below the FDA limit of 720 mW/cm^2 for ultrasound imaging. The microwatt telemetry protocol proposed in this work is simple and expected to work in numerous other settings.

4.5. SEARCH ALGORITHM FOR DETECTING THE IMPLANT

Now let us assume that RX must be accurately located without prior knowledge. The search for the implant will need to be broken down into two phases. The first phase is to roughly detect where RX is through B-mode imaging. Since the implant is typically a highly reflective material, the implant will be visible. Then a region of interest (ROI) is implemented for the second phase, in which a rigorous scan will be executed to find RX using the previously developed microwatt telemetry protocol. The time that it will take is,

(Total time) = (# of pixels to measure) × (Time to measure a single pixel)

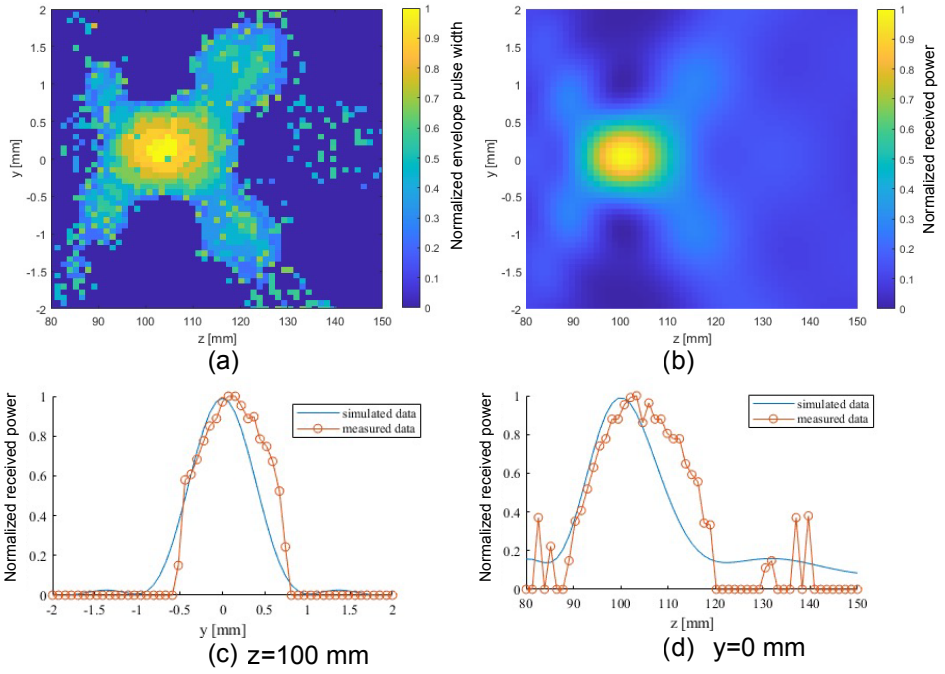

Figure 4.11: Comparison of the (a) measured and (b) simulated ultrasound power reception plotted in a heat map. The ultrasound power received along (c) z = 100 mm (d) y = 0 mm.

The time to measure a single pixel can be broken down into the following steps,

1. Receive two ultrasound burst at 1 kHz PRF : 20 ms
2. Find the pulse width : < 1ms
3. Check if there is modulation : < 1 ms
4. if true: update and save the data and plot on screen: < 1 ms
5. Change the focus to the next point: 50 ms

Fig. 4.12 is another measurement of when ROI was segmented to 30 × 30 = 900 pixels and when a rigorous scan was executed. The time that it took was 70 ms × 30 × 30 ≈ 2 min. This could be improved if the algorithm was to be implemented in a lower level language such as an FPGA instead of the MATLAB interface. However, in resource limited settings, it may be desirable to find the hot spot through a smarter algorithm. In the following part two faster algorithms were tested.

One straight forward search algorithm that was investigated was to incrementally search for the global maximum using the information from the microwatt telemetry protocol. Assuming that the algorithm begins at an arbitrary location within the ROI,

the global maximum was searched by following the gradient of the received ultrasound power and by incrementally searching for higher received power. This is analogous to climbing a mountain by following the uphill direction where the top of the mountain has the highest received power. Unfortunately after implementing this approach it was found to be unreliable because the side lobes of ultrasound signal creates local maxima in which case the algorithm becomes blind to its neighboring peaks.

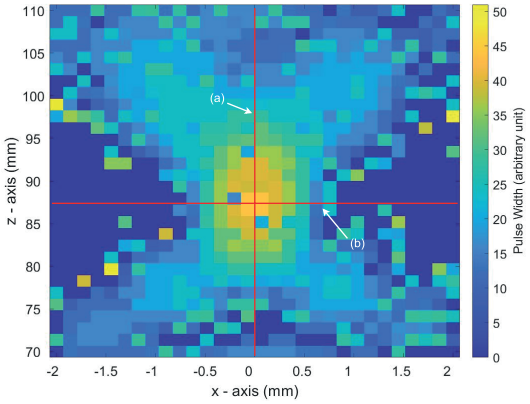

Figure 4.12: Heat map for new coordinate system.

Another approach was to use time/phase reversal beam forming [7]. Fundamentally, this works by generating a first ping from the RX. The ping will arrive at the the TX elements with different time delays, typically forming a parabolic curve since the source can be seen as a point source and we assume a linear TX. By playing back the ping in reverse, the focus can be navigated towards RX. Here, we extend this concept and used the rising edge of the envelope pulse from the microwatt telemetery protocol. The process is shown schematically in Fig. 4.13. First the two consecutive backscattered signals are recorded with the 128 elements of the US probe (see Fig. 4.13(a)). At this state the signals are noisy and cannot be used. Thus, the difference between the two signals is taken and the envelope signal is detected. A parabolic curve is fitted on the rising edge of the envelope signal as shown in Fig. 4.13(b). Next, the ultrasound signal is generated while aligning the rising edge of the ultrasound signal along the inverted parabolic curve to focus the ultrasound signal towards RX (see Fig. 4.13(c)).

Fig. 4.14(a) shows how the focus moved using the time/phase reversal technique. The blue dot is where the modulation was detected and the focus jumped to the red star at the center of the heatmap (shown in the background). The detected delay is shown in Fig. 4.14(b) as a blue dot. The rising edge of the envelope signal was detected at

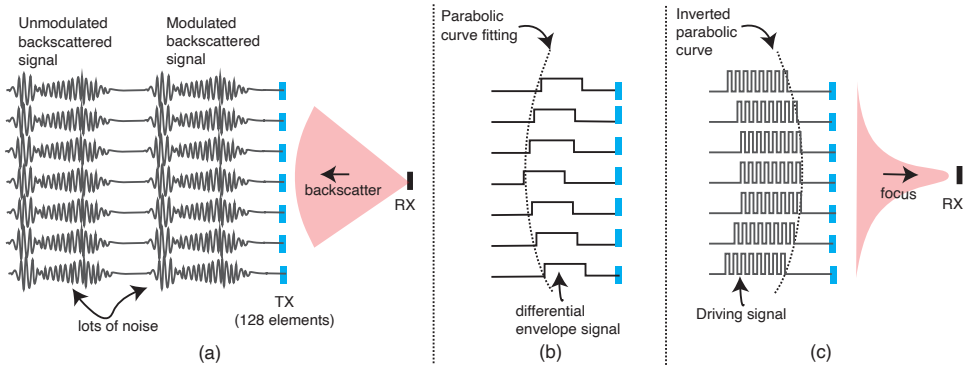

Figure 4.13: Phase reversal beam forming using the microwatt telemetry protocol. (a) Two consecutive backcattered signal received at the ultrasound probe both having a lot of noise. (b) The parabolic curve is fitted on the delay detected from the envelope signal. (c) The parabolic curve is inverted and the ultrasound is transmitted to focus on RX.

each channel through a cross-correlation technique (*finddelay* function in MATLAB) and the first channel was used as the reference channel to compute the phase/time delay observed at each channel. The additional time that was needed for this algorithm was mainly for the curve fitting process which took nearly 0.3 sec. Adding this to the previous 0.13 seconds, the time it takes for this algorithm to reach the hotspot was roughly 0.4 seconds.

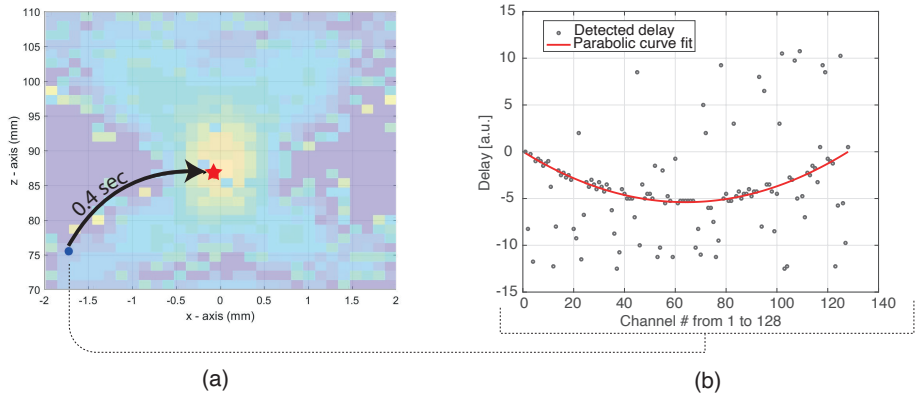

Figure 4.14: (a) Hot-spot tracked by the algorithm (red color dot). (b)The delay detected at 128 elements along the width of the ultrasound probe and the parabolic curve that was fitted along the delay.

4.6. CONCLUSION

In this work, the proposed microwatt telemetry protocol was able to communicate information of the power received at the RX to the ultrasound probe. The resolution of the microwatt telemetry protocol was high enough to navigate the focus to a sub-mm wide RX element at 10 cm depth through a gel phantom. The protocol developed in this work was tested in a 2D setup with a 1D linear array. The RX transducer used in this work was a CMUT array, which can be replaced with any other transducer as long as the reflection coefficient can be modulated sufficiently by changing the electrical loading condition. Two algorithms to locate the implant were tested. The time/phase reversal algorithm shown in this work detected where the implant was located with a 0.4 seconds after the first modulation was detected. Compared to a rigorous scanning technique, which took approximately two minutes, there is a considerable improvement. A short discussion about the influence of angular misalignment on the backscattered communication was also shown in this work. The RX used in this work has an angular acceptance of ± 10 degrees, but the backscattering communication only had a angular tolerance of ±8 degrees. This implies that there may be a case when sufficient power is being sent from the TX to RX but the RX will will not be able to communicate that information back to the TX. To mitigate such issues, it is recommended to increase the receiving aperture of the TX by positioning ultrasound transducer elements at wider distance.

Finally, the fundamental concept of the microwatt telemetry protocol can be extended to any other type of data-set (i.e. temperature data, action potential, heart rate), since the key is to use one of the bursts as a reference and by doing this at a relatively high PRF (> sub-kHz range) to denoise the lower frequency artifacts (i.e. hand movement, breathing).

For future work, the microwatt telemetry protocol will be tested in inhomogeneous mediums with vibrating motions to mimic a real-life use case. Furthermore, considering the time/phase reversal technique, there are situations when the modulation was detected but the delay did not follow a parabolic curve due to significant noise. It seemed that the noise was random and affecting all the channels. The primary noise sources are the : 1) acoustical contact between the ultrasound probe and the phantom and 2) errors in delay detection using the cross-correlation function of MATLAB. Thus, these noise sources must be addressed more specifically in future work to create a more robust time/phase reversal algorithm.

BIBLIOGRAPHY

[1] K. Famm, B. Litt, K. J. Tracey, E. S. Boyden, and M. Slaoui, "A jump-start for electroceuticals", *Nature*, vol. 496, no. 7444, pp. 159–161, 2013, ISSN: 0028-0836. DOI: 10.1038/496159a.

[2] V. Cotero, Y. Fan, T. Tsaava, *et al.*, "Noninvasive sub-organ ultrasound stimulation for targeted neuromodulation", *Nature Communications*, vol. 10, no. 1, p. 952, Dec. 2019, ISSN: 2041-1723. DOI: 10.1038/s41467-019-08750-9. [Online]. Available: http://www.nature.com/articles/s41467-019-08750-9.

[3] D. K. Piech, B. C. Johnson, K. Shen, *et al.*, "A wireless millimetre-scale implantable neural stimulator with ultrasonically powered bidirectional communication", *Nature Biomedical Engineering*, vol. 4, no. 2, pp. 207–222, 2020, ISSN: 2157-846X. DOI: 10.1038/s41551-020-0518-9. [Online]. Available: https://doi.org/10.1038/s41551-020-0518-9.

[4] T. C. Chang, M. J. Weber, J. Charthad, S. Baltsavias, and A. Arbabian, "End-to-end design of efficient ultrasonic power links for scaling towards submillimeter implantable receivers", *IEEE Transactions on Biomedical Circuits and Systems*, vol. 12, no. 5, pp. 1100–1111, 2018, ISSN: 19324545. DOI: 10.1109/TBCAS.2018.2871470.

[5] S. Sonmezoglu, A. Darvishian, K. Shen, M. J. Bustamante, A. Kandala, and M. M. Maharbiz, "A Method and Analysis to Enable Efficient Piezoelectric Transducer-Based Ultrasonic Power and Data Links for Miniaturized Implantable Medical Devices", *IEEE Transactions on Ultrasonics, Ferroelectrics, and Frequency Control*, vol. 68, no. 11, pp. 3362–3370, Nov. 2021, ISSN: 15258955. DOI: 10.1109/TUFFC.2021.3093867.

[6] C. Shi, T. Costa, J. Elloian, Y. Zhang, and K. L. Shepard, "A 0.065-mm ³ Monolithically-Integrated Ultrasonic Wireless Sensing Mote for Real-Time Physiological Temperature Monitoring", *IEEE Transactions on Biomedical Circuits and Systems*, vol. 14, no. 3, pp. 412–424, Jun. 2020, ISSN: 1932-4545. DOI: 10.1109/TBCAS.2020.2971066.

[7] B. C. Benedict, M. M. Ghanbari, S. F. Alarnouti, N. T. Ersumo, and R. Muller, "Time reversal beamforming for powering ultrasonic implants", in *International IEEE/EMBS Conference on Neural Engineering, NER*, vol. 2021-May, 2021, pp. 647–650, ISBN: 9781728143378. DOI: 10.1109/NER49283.2021.9441162.

[8] M. Fink, G. Montaldo, and M. Tanter, *Time-reversal acoustics in biomedical engineering*, 2003. DOI: 10.1146/annurev.bioeng.5.040202.121630.

[9] J. Charthad, M. J. Weber, T. C. Chang, and A. Arbabian, "A mm-Sized Implantable Medical Device (IMD) With Ultrasonic Power Transfer and a Hybrid Bi-Directional Data Link", *IEEE Journal of Solid-State Circuits*, vol. 50, no. 8, pp. 1741–1753, 2015, ISSN: 00189200. DOI: 10.1109/JSSC.2015.2427336.

[10] R. J. McGough, "Rapid calculations of time-harmonic nearfield pressures produced by rectangular pistons", *The Journal of the Acoustical Society of America*, vol. 115, no. 5, pp. 1934–1941, May 2004, ISSN: 0001-4966. DOI: 10.1121/1.1694991.

[11] D. Chen and R. J. McGough, "A 2D fast near-field method for calculating near-field pressures generated by apodized rectangular pistons", *The Journal of the Acoustical Society of America*, vol. 124, no. 3, pp. 1526–1537, Sep. 2008, ISSN: 0001-4966. DOI: 10.1121/1.2950081.

5

SPATIALLY SPECIFIC ULTRASOUND NERVE STIMULATION WITH CMUTS

Study hard what interests you the most in the most undisciplined, irreverent and original manner possible.

Richard P. Feynman

5.1. INTRODUCTION

Currently marketed vagus nerve stimulators are used to treat epilepsy and depression by stimulating the vagus nerve. Vagus nerve stimulation (VNS) works by implanting a cuff electrode directly onto the vagus nerve located at the neck. Since the vagus nerve is a bundle of nerves that includes efferent and afferent nerves connecting to many organs (i.e. heart, lung, spleen, stomach etc.), recently clinical trials have begun to explore VNS as a method to modulate these other organs for therapeutic benefits. Some examples of these clinical trials target chronic heart failure [3] or autoimmune diseases such as Crohn's disease or rheumatoid arthritis. However, the side effects of these therapies

Parts of this chapter have been published in IEEE NER19 and NER21 **324**, 289 (2021) [1], [2]. All animal experiments have been approved by the 'Centrale Commissie Dierproeven' (Central Commission for Animal Experiments) of the Netherlands Government and have been performed at the VU University according to the Netherlands Law on Animal Research (Wet op de Dierproeven) in full agreement with the Directive 2010/63/EU with local approval by and under supervision of the local Animal Welfare Body (and Governmental surveillance).

still remain; these include neck pain, coughing, voice alteration, and dyspnea [4]–[6] . Therefore, the goal of this chapter is to explore a new stimulation technique, which has the potential to induce a therapeutic effect that targets only one of the previously mentioned diseases, while reducing the side effects by localizing the stimulation to individual fascicles within the nerve.

The development of selective stimulation with electrodes can be separated into the non-invasive and invasive electrodes. One option, by the group of T. Stieglitz et al. was to mechanically pierce through a peripheral nerve and to distribute highly selective electrode contacts over the cross section of the nerve, which can create localized activation at the fascicular level [7]. This method was effective in achieving spatially specific stimulation in the sciatic nerve of a pig, yet the challenge would be to implant this device for long term within the vagus nerve which raises much more concerns because the nerve is in charge of vital functions. Another approach by M. Ortega et al. [8], [9] is to create thin and soft electrodes that are as soft as the nerve itself and penetrate the vagus nerve to avoid frictional damage towards the nerve. Due to this soft thread/suture like electrode this is referred to as sutrode (suture + electrode) in there work which may allow spatial stimulation and recording of the vagus nerve. This will sure allow good spatiall recording capability of the nerve. Another option investigated was to use multiple electrodes along the inner walls of a cuff that can be excited independently (i.e. multi-contact electrode). Yet A-fibers are more easily stimulated compared to C-fibers which fundamentally limits the selectivity of this approach. As an alternative approach, we propose to use focused ultrasound (US) to stimulate individual fascicles within the vagus nerve. It has already been shown that US can stimulate neurons [10], [11] .The stimulation mechanism remains to be unclear, but one possible explanation is that the acoustic force from the US deforms the cell membrane and stimulates the mechano-sensitive ion channels, or that the ultrasound is strong enough to puncture a hole in the cell membrane initiating a depolarization of the membrane. Transcranial US neurostimulation has been studied extensively over the past decade due to its compelling characteristic to stimulate certain regions deep within the brain but without invasively penetrating the brain [9]. Similarly, we hypothesize that if US transducers are wrapped around the vagus nerve, individual fascicles within the vagus nerve can be stimulated without penetrating the nerve.

For transcranial applications, the US frequency is commonly below 5 MHz, as higher frequency US will not penetrate through the skull. This limits the spatial resolution of the therapy to several millimeters. Unfortunately, this is already too coarse for spatial VNS stimulation, as the vagus nerve has a diameter of about 2 to 4 mm at the site of stimulation. However, the resolution can be increased if higher frequencies and a larger

number of US transducers are employed. Luckily, operating at higher frequencies is not a limitation for our proposed solution, as the US transducers will be wrapped directly around the vagus nerve.

Only a handful of researchers have conducted in-vivo tests at these frequencies. M. Menz et al. stimulated retinal ganglion cells with US at a frequency of 43 MHz for retinal prosthetic application [12]. This was possible because the retinal cells are directly accessible through the surface of the eye without penetrating the skull. These results indicate that neurons can indeed be activated at higher US frequencies, strengthening our hypothesis that stimulation of neurons within the vagus nerve with such high frequencies should be feasible. In the past, creating a cuff with US transducers so small that could be wrapped around the vagus nerve would be unthinkable. Due to the advent of mechanical and electrical micro systems (MEMS) it is now possible to fabricate thousands of US transducers in a few millimeter square area. This allows for a high-resolution US cuff at a size comparable to conventional VNS cuff electrodes.

In this chapter, we first introduce the concept of a new high-resolution ultrasound based peripheral nerve stimulator. The fabrication method of the flexible array of US transducers is explained and the acoustic measurement results of such devices are discussed. Then the spatial specificity that can be acheived with such device is simulated and confirmed using a schlieren imaging setup. The remainder of this paper illustrates the experimental results of using these US transducer elements to stimulate the sciatic nerve of a rat in an in-vivo setup.

5.2. PART I : SIMULATION AND CHARACTERIZATION

5.2.1. CONCEPT : HIGH FREQUENCY CMUTS

The CMUTs used in this work were manufactured at Philips Research for the development of intravascular ultrasound catheters (IVUS). The imaging capability and bandwidth properties of the device can be seen in the works by [13] which shows that the CMUTs have a -6 dB bandwidth of 25 MHz with a center frequency of 20 MHz at 30 V bias voltage. The device is realized through the Flex-to-Rigid (F2R) process [14] which is a method to connect independent silicon islands through a polyimide (PI) substrate with interconnects embedded within the PI substrate. This allows the independent silicon islands to be electrically accessible while giving it the foldable property through the flexible PI regions. A photograph of the CMUT in its flat state is shown in Fig. 5.1(a) along with the half metal form that was used to create the curvature. Fig. 5.1(b) shows a mask layout of the CMUT device.

In this work we repurpose this technology for ultrasound neurostimulation by wrapping the device in the opposite direction where the CMUTs will be folded inwards having the focus towards the center of the circle. On this test device there are 112 elements out of which 48 of them could be independently addressed with different voltages. These devices are located at the center of the device as shown in the same figure. The remainder of the 64 elements are tied together to a single electrical contact. Fig. 5.1(c) shows the device glued to the circular cuff and Fig. 5.1(d) shows the same device but from a different angle. After gluing the CMUT into the curvature, the device is wirebonded to a PCB. Next, the surface of the CMUT is coated with a 10 µm thick Polydimethylsiloxane (PDMS) layer as the acoustic matching layer.

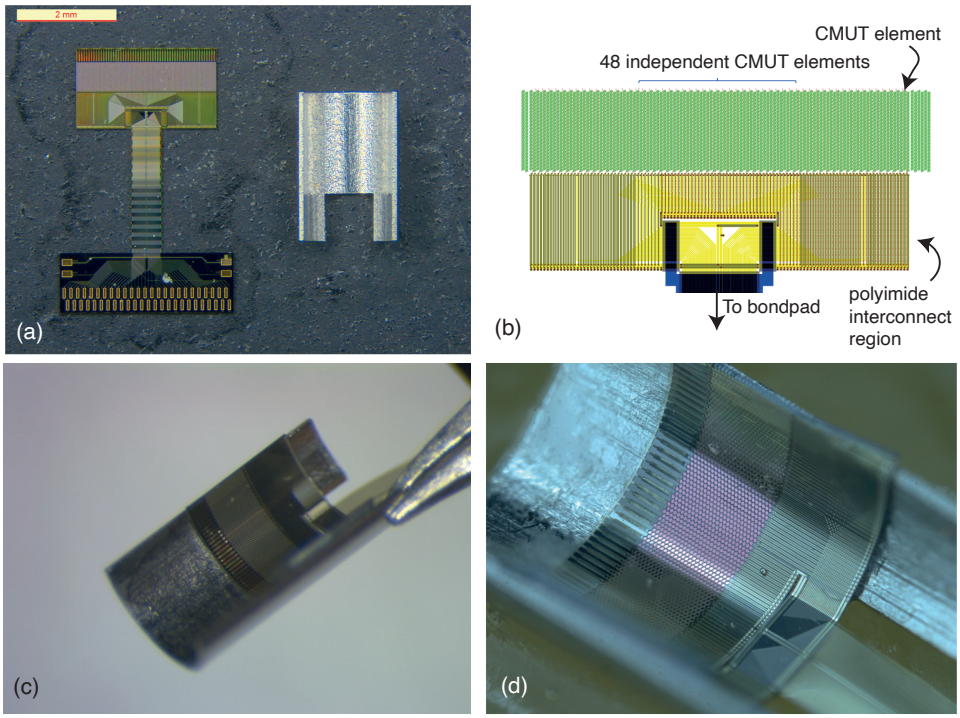

Figure 5.1: (a) CMUT device in flat position (left) and the 2 mm diameter half metal pipe (right). (b) The CMUT device rolled into a cuff.

Fig. 5.2(a) shows an illustrative cross section of a peripheral nerve. A peripheral nerve is composed of the external epineurium, fascicles which have unmyelinated and myelinated axons and blood vessels. Fig. 5.2(b) shows a conceptual image of the ultrasound transducer wrapped around the nerve. In this figure the ultrasound transducer is shown with a black line and the focal spot that appears at the center when the ultrasound trans-

ducers are driven simultaneously. The focal length along the propagation direction of the ultrasound wave is called focal depth (FD) and the focal beam diameter (FBD). Both dimensions are defined with a -3 dB threshold.

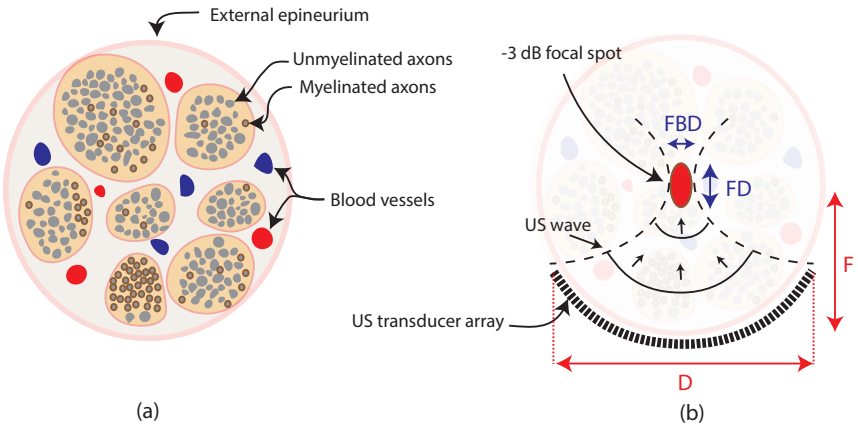

Figure 5.2: Ultrasound stimulation concept using a CMUT array

5.2.2. SIMULATION STUDY

In this section, the high frequency CMUTs were simulated to see how the spatial specificity increases with the frequency and aperture. The simulation was done using Fast Object Oriented C++ Ultrasound Simulator (FOCUS) and the focal spot size was defined as the area within the -3dB region. In order to simulate an acoustic field using FOCUS, the transducer information (i.e. size, amplitude, position, shape, timedelay), the medium information (i.e. attenuation coefficient, non-linearity coefficient) and the simulation settings (i.e. transient simulation, continuous wave simulation, spatial and temporal coordinate grid) must be defined.

The acoustic parameters of a nerve are summarized in Tab. 5.1, For simplicity, in this simulation the nerve was simulated as an homogeneous medium with a single acoustic property. Furthermore, the surrounding medium around the nerve is also assumed to have the same acoustic properties as the nerve and reflection or scattering phenomenon due to different mediums around the nerve are not taken into account. In the simulation one transducer element which consists of 24 CMUT devices was simulated as a single rectangular ultrasound transducer element. The radial curvature of the CMUT was chosen as 1 mm as this would be the typical radius of a cervical vagus nerve of a human. The velocity of the ultrasound transducer was set to 1 m/s. Fig. 5.3 (a) shows an illustration of a 2 mm diameter nerve with 48 ultrasound transducer elements wrapped around the

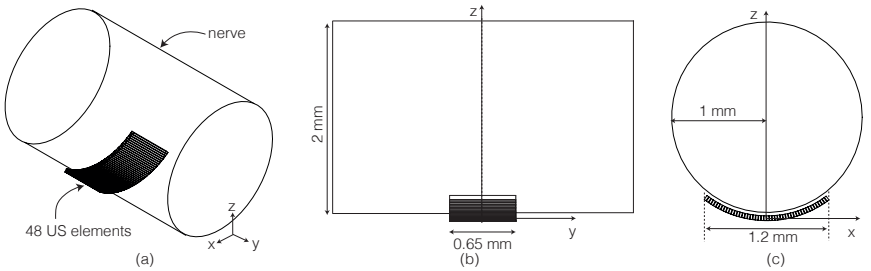

Figure 5.3: Simulation model with a 2 mm diameter nerve wrapped by and US transducer array of 48 elements. (a) Perspective (b) y-z plane (c) x-z plane.

perimeter. Fig. 5.3 (b) and (c) are views of the z-y plane and the x-z plane respectively. The simulation was done in continuous wave mode.

5

Table 5.1: Simulation parameters

Nerve Parameter	Value	Unit	Transducer parameter	Value	Unit
Diameter	2	mm	Amplitude	1	m/s
Speed of sound.	1629.5	m/s	Transducer shape	Rectangular	
Density	1075	kg/m^3	Width	25	µm
Attenuation Constant	13.3	Np/m/MHz	Height	0.65	mm
Acoustic impedance	1.75	MRayls	Element Number	48, 64, or 112	
			kerf	5	µm
			Curvature	1	mm
			Frequency	5 to 40	MHz

Fig. 5.4 shows the simulation results along x = 0 and y = 0 planes when the 48 elements are driven simultaneously at 15 MHz. Fig. 5.4(b) and (c) shows, the pressure and intensity profile evaluated along each plane. The result of the simulation are compared to hydrophone measurements results within the following publication [1]. Fig. 5.5 reprinted from the publication showing the good agreement between the hydrophone measurement and the simulation result. The full article is inclduded in Appendix B. This verified that the simulation method was indeed correct.

In the following section, the spatial specificity for a diverse range of apertures and frequencies was simulated. The number of elements was set to 48, 64 and 112 elements, and the frequency was varied from 5 MHz to 40 MHz in 20 steps. To shorten the simulation time, the computational grid along the x, z axis was limited near the center of the cuff ; $x \in [-0.15\text{mm}, 0.15\text{mm}]$, $z \in [0.5\text{mm}, 1.4\text{mm}]$ and only along the y=0 plane. For each axis, the resolution was set to be less than $1/10^{\text{th}}$ of the minimum wavelength; dx = 1.2 µm, dz = 3.6 µm for sufficient accuracy.

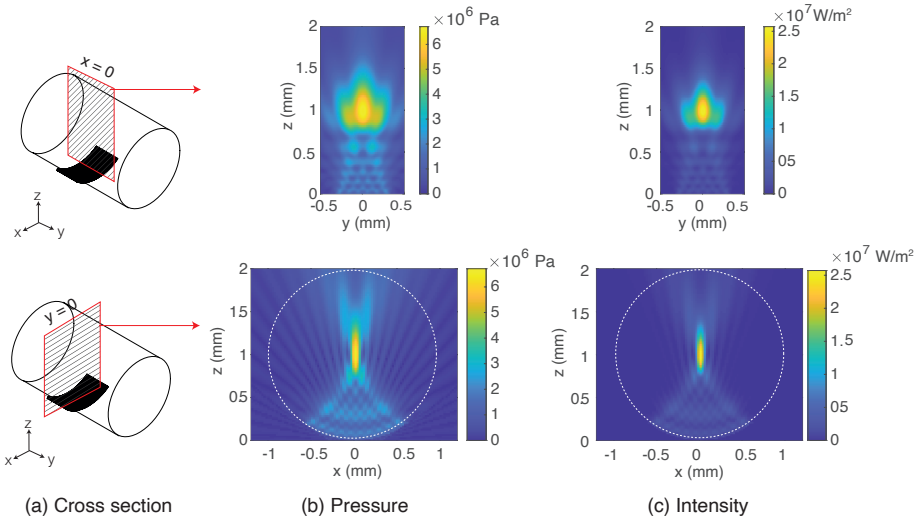

Figure 5.4: (a) Top row and bottom row shows the simulated ultrasound profile evaluated along cross section of x = 0 and y = 0 respectively. (b) Pressure profile (c) Intensity profile.

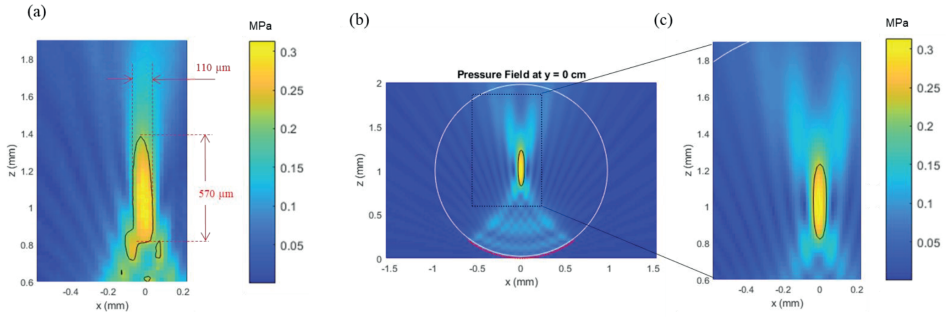

Figure 5.5: Comparison of the experiment and the simulation. (a) The pressure profile measured using an fiber optic hydrophone. (b) The simulation result of the pressure profile. The white line shows the contour of the vagus nerve (ϕ = 2 mm) and the black contour line represents the -3 dB level. The color bar shows the positive peak value of the pressure profile. The red dots represent the position of each CMUT element. (c) A close up image of (b) also corresponding to the same location in (a).

Fig. 5.6(a) shows an example of the simulation along the y = 0 plane at f = 7MHz for 64 elements. From the figure, the -3dB focal spot (i.e. FD, FBD) was extracted. Fig. 5.6(b) combines the results for the focal spot for the entire simulation range. From this figure, it can be seen that the dimension of the focal spot is inversely proportional to the US frequency. In the same figure, the gray shadowed region indicates the fascicle diameter, and the red shadowed region indicates the typical fiber diameter. For 48 elements, FD begins to be comparable to the fascicle diameter at 12 MHz. Thus, as long as the frequency is higher than this, fascicle level specificity can be achieved. For higher number of elements both the FD and FBD are smaller than, or comparable to the fascicle diameter. Finally, from this simulation, it can be seen that by increasing the number of elements to 112 elements and having a frequency beyond 16 MHz it will be possible to achieve spatial specificity at subfascicular level.

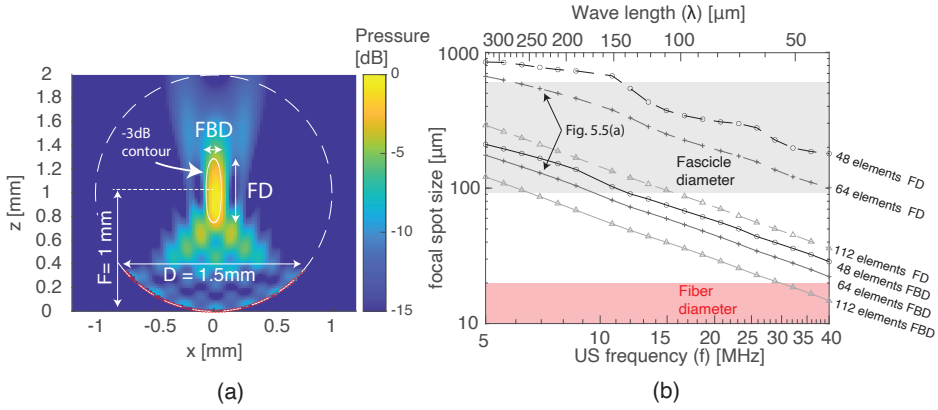

Figure 5.6: (a) left) The -3dB pressure level simulated with FOCUS for 64 elements driven at 7 MHz. right) A zoomed in figure of the -3dB pressure level. (b) The ultrasound frequency and wave length respect to the -3dB focal width and length.

5.2.3. BEAMFORMING

An important aspect that must be confirmed is whether the position of the focal spot can be controlled. Fortunately, it is possible to apply beamforming to control the position of the focal spot. This works by applying a certain time delay to each ultrasound element. For driving the CMUT elements we used the in-house developed 32-channel ultrasound driver system. The detail of how this works is explained in appendix C.2.

Using this hardware restricted the maximum frequency to 14.3 MHz limited the transducer number to 32 elements while there were 48 elements available. Thus, beamforming was investigated by controlling the 16 element on the right side and the 16 elements

on the left side of the transducer array. Furthermore, beamforming was verified in the following publication [2] using an optical setup called the schlieren system. In this system the ultrasound wave propagating through a medium is optically visualized through the change of refractive index caused by ultrasound. This enables rapid visualization of the ultrasound field compared to scanning the ultrasound field with a hydrophone. Using this technique, the wavefront of the ultrasound was visualized using a stroboscopic technique [1]. Readers are referred to the full article in appendix B for a complete explanation of the system. Here we introduce some key results.

Fig. 5.7 shows a comparison of the acoustic field simulated with FOCUS (left column) and the acoustic intensity measured with the schlieren system (right column). The focal spot was steered to four different spots and the intensity profile was extracted by integrating the video over time. The simulation and the measurement results are clearly similar in this comparison, however, the schlieren image has more background noise. Nonetheless, the possibility to steer the beam was demonstrated.

5.2.4. ACOUSTIC INTENSITY FOR US STIMULATION

In many of the US stimulation protocols found in literature, the ultrasound signal is modulated at three different time scales [15] . Fig. 5.8 shows a schematic with these different time scales of the ultrasound signal corresponding to each row. The first row has the largest time scale which defines the total time (TT) of the ultrasound stimulation. It consists of a repetition of shorter bursts with a burst duration (BD) and a burst interval (BI). Then the second row shows a zoomed in schematic within one burst. Each burst consists of a trail of shorter ultrasound pulses. The duration of the pulse is defined as the pulse length (PL) and it is repeated at the pulse repetition frequency (PRF). Finally, each ultrasound pulse is composed of an ultasound signal with a certain frequency and pressure as shown in the bottom row of the same figure.

Depending on each time scale, the intensity is defined separately. The average intensity within one PL is the spatial-peak pulse-average intensity (I_{SPPA} [W/m^2]). Then the average intensity within one BD is the spatial-peak burst-average intensity (I_{SPBA}[W/m^2]). Finally, the average intensity over TT is the spatial-peak temporal-average intensity (I_{SPTA} [W/m^2]).

The I_{SPPA} is related to the acoustic pressure through the following equation.

$$I_{SPPA} = \frac{P^2}{2Z} \tag{5.1}$$

[1] https://doi.org/10.34894/Y4FILA

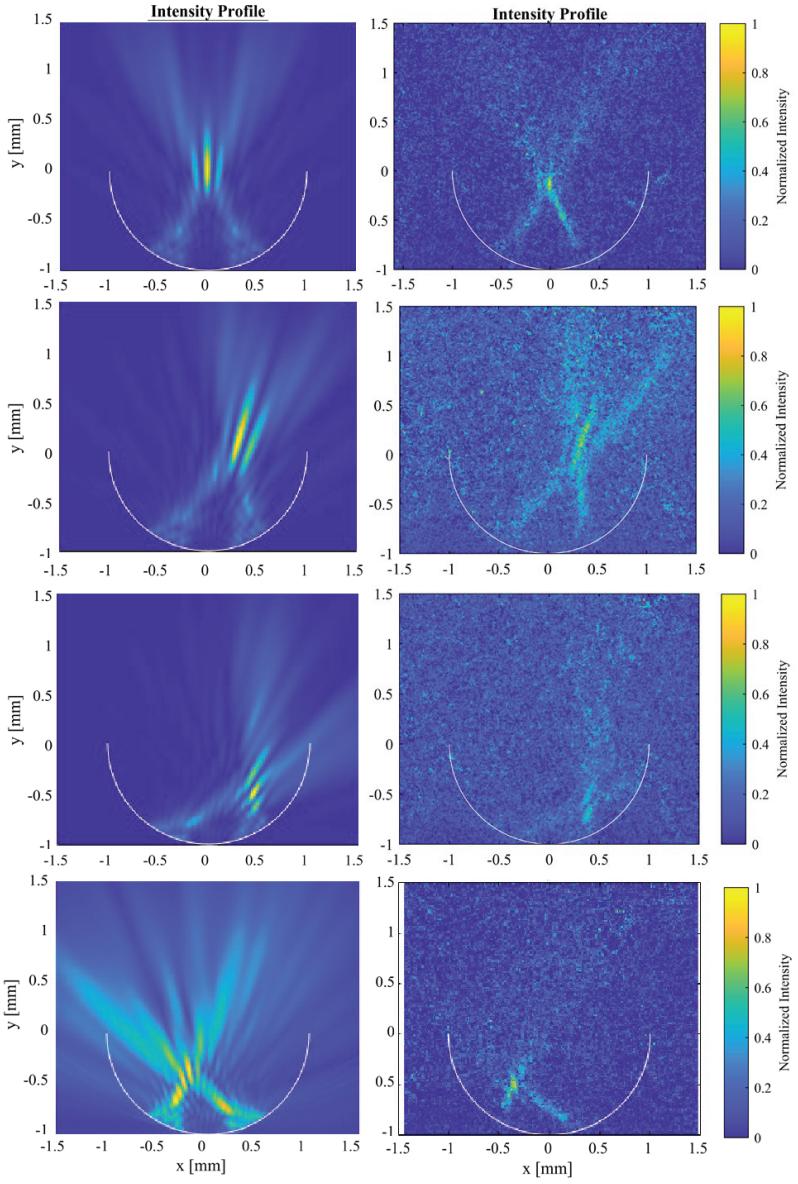

Figure 5.7: Comparison of the simulation result and the measurement result when beam forming is applied.

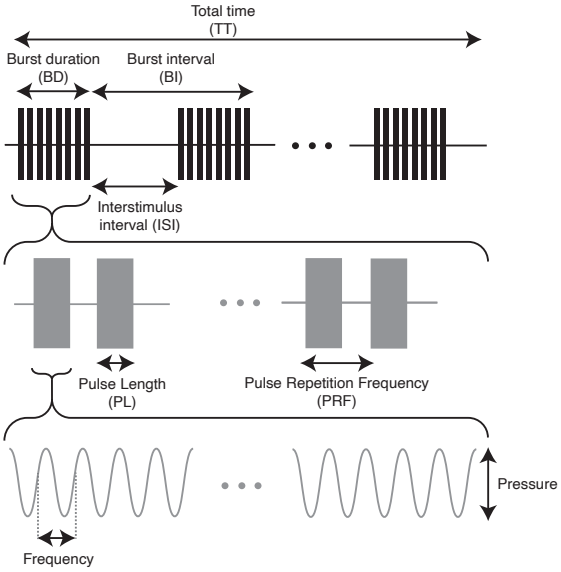

Figure 5.8: Schematic of ultrasound parameters used in ultrasound stimulation at three different time scales.

where P is the amplitude of the ultrasound pressure and Z is the characteristic acoustic impedance of the medium. The other definitions for pressure (i.e. I_{SPBA} and I_{SPTA}) can be derived from the above equation by multiplying I_{SPPA} with the duty ratio. According to Equation 5.1 the pressure of the ultrasound wave must be measured to find the intensity.

Fig. 5.9 shows the experimental setup to measure the acoustic pressure generated by the CMUT and the PZT transducers. In both experimental setups an optical fiber pressure sensor (Precision Acoustics, UK) was positioned at the center of the focal point where the maximum pressure was measured. This was found by moving the hydrophone incrementally using a 3D motor stage. The maximum acoustic pressure at the center of the CMUT array when 32 elements were driven simultaneously, with a DC bias voltage of 35 V and an AC amplitude of 25 V was applied at 15 MHz, 20 MHz, 25 MHz, and 30 MHz resulted in a peak negative pressure of 1.1 MPa, 2.5 MPa, 1.4 MPa, and 1.3 MPa respectively. The spatial peak pulse average intensity that could be achieved with the US driver system was 44 W/cm^2, 207 W/cm^2, 64 W/cm^2 and 60 W/cm^2 respectively.

Considering the PZT ultrasound transducer, four different ultrasound probes were used which had center frequency of 1 MHz, 5 MHz, 10 MHz and 20 MHz. These devices were used as a backup for the ultrasound cuff experiment in Section 5.3. The transducers used for this experiment all had a focal spot at approximately 1 cm distance from the

tip of the transducer. The peak negative pressure and Isppa for different peak to peak voltage is shown Fig. 5.10 (a,b).

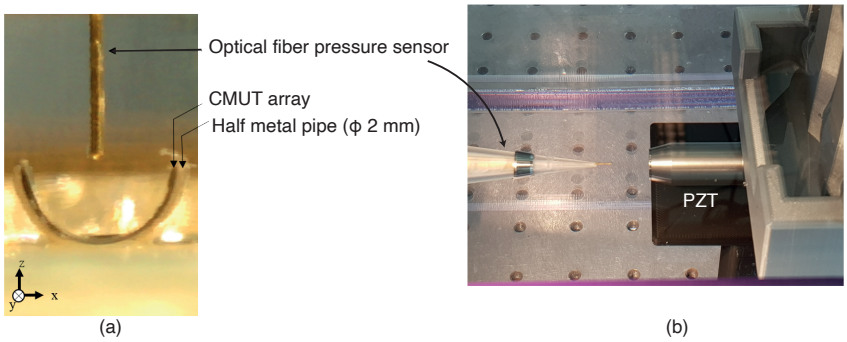

Figure 5.9: Acoustic pressure measurement for (a) CMUT (b) PZT

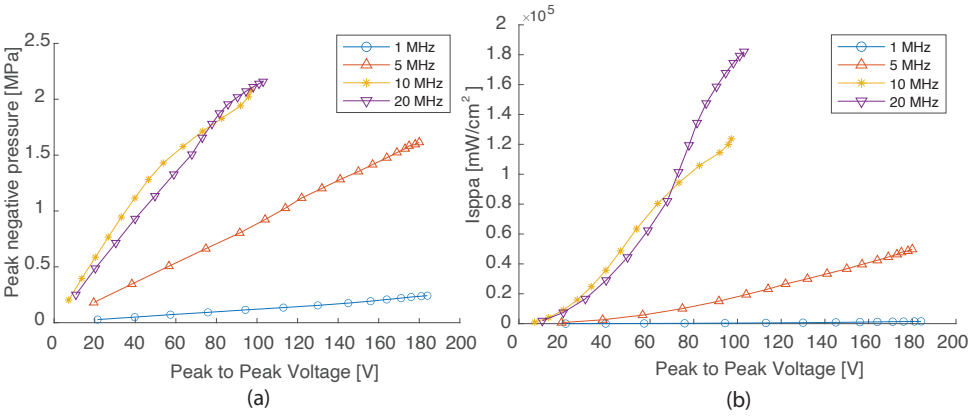

Figure 5.10: Acoustic pressure measurement of the PZT transducer probe.(a) Peak negative pressure and (b) Isppa with respect to the applied voltage to the probe.

5.3. PART 2 : IN-VIVO EXPERIMENT

5.3.1. ANATOMY OF THE SCIATIC NERVE OF A RAT

In this section the in-vivo validation of the concept was attempted with the sciatic nerve of a rat to test stimulation specificity. This was because the sciatic nerve was selected because it is the largest nerve within the rat and it is similar to the size of a human vagus nerve. The sciatic nerve contains three major nerve bundles, which are the tibial nerve, the sural nerve and the commmon peroneal nerve (see Fig. 5.11). Selective stim-

ulation strategies are often tested with the sciatic nerve of a rat because of this simple hierarchical organization. The stimulation selectivity at the proximal end of the nerve is analyzed either by hooking an electrical recording cuff along the three nerve bundles after the bifurcation of the nerve, or by observing the direction in which the leg flicks. Where the tibial nerve stimulation results in a plantar flexion and the common peroneal nerve stimulation leads to a dorsiflexion as shown in Fig. 5.11 (B).

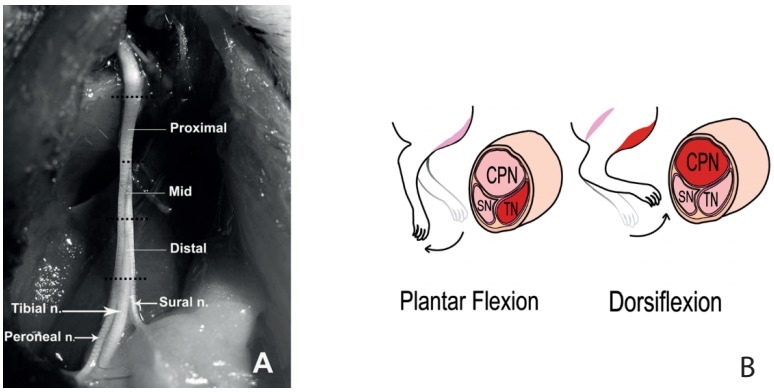

Figure 5.11: (A) Photograph of the rat sciatic nerve adopted from [16]. (B) Illustration of the direction in which the leg flick depending on where the stimulation occurs. Figure adopted from [17]

In this work, as spatially specific sciatic US nerve stimulation has never been applied in the past, we decided that being able to differentiate between three different nerve bundle should be our initial target. If additional selectivity is needed, more electrodes can be added at further distal bifurcation points or by using multipolar recording cuffs. In the following section the experimental setup is explained.

5.4. EXPERIMENTAL SETUP AND RESULT

The experiment was done at Vrije Universiteit Amsterdam with the help from Huub Maas's group. Fig. 5.12(a,b) shows the experimental setup with the CMUT ultrasound cuff and the PZT ultrasound probe. In both setups the sciatic nerve of a rat was exposed and the proximal end of the nerve was sectioned and positioned at the focal spot of the ultrasound stimulator. For the CMUT ultrasound cuff, the nerve was gently positioned on top of the cuff. The nerve was soft enough to deform into the shape of the ultrasound cuff. Considering the PZT probe, a 3D printed coupling cone was created to couple the ultrasound energy towards the nerve and to prevent the electrical noise to couple into the recording electronics. A thin PET foil or parafilm was glued on the tip of the coupling

cone to prevent the coupling medium to leak out. At 2 to 3 cm distance from the stimulator a hook electrode was positioned along the nerve at the distal side. The hook electrode was connected to an amplifier and then to a readout system. For the ultrasound stimulation experiment a vast amount of stimulation parameters are available (i.e. PRF, ultrasound frequency, amplitude, total time). To adjust this parameters on the fly during the experiment a GUI was made using the Python tkinter package. This software also stored the settings for each stimulation for offline analysis of the data. More detail on the ultrasound hardware and software used for the experiment can be found in Appendix C.

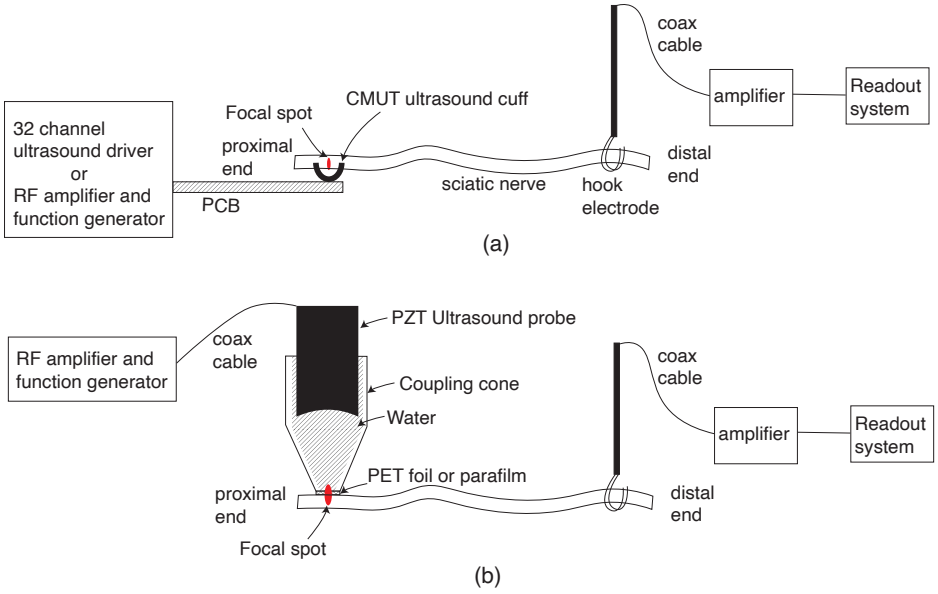

Figure 5.12: Schematic of the ultrasound stimulation setup. (a) CMUT ultrasound cuff and (b) PZT ultrasound probe.

Fig. 5.13(a) shows the experimental setup with the sciatic nerve positioned on top of the US cuff. A zoomed in photo of the setup can be seen in Fig. 5.13(b) with one end of the nerve being layed on the ultrasound cuff. With the same setup a reference experiment with PZT ultrasound probe was conducted as shown in Fig. 5.13(c). Unfortunately with this setup no stimulation of the sciatic nerve was observed. In the following section this outcome will be discussed in relation to what other researchers have done over the years.

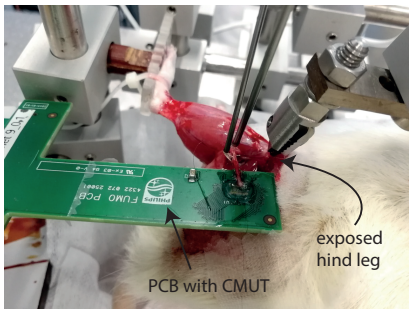

(a) CMUT ultrasound stimulation

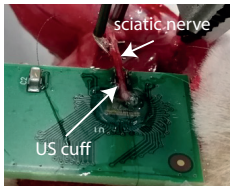

(b) CMUT ultrasound stimulation (zoom)

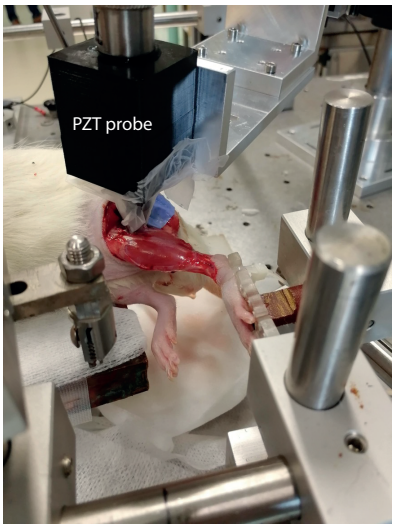

(c) PZT ultrasound stimulation

Figure 5.13: Pictures of ultrasound stimulation setup of the sciatic nerve of a rat. (a) US stimulation with a CMUT (b) zoomed in photo (c) US stimulation with a PZT probe.

5.5. CONCLUSION AND FUTURE WORK

In Section 5.2 of this work, the ultrasound cuff concept was introduced and the ultrasound cuff device was simulated, assembled and tested. From the simulations, the required number of ultrasound elements to achieve fascicle level stimulation at a specific frequency was derived. For example, if 48 ultrasound transducers are used, at least 12 MHz is needed to achieve fascicle level stimulation. The simulations also showed the requirements for fiber level stimulation which was to have 112 elements and frequencies beyond 30 MHz. Following the simulations, the ultrasound cuff device was assembled and the acoustic pressure was measured and beamforming capability was tested and verified using the schlieren system.

In Section 5.3 of this work, an ultrasound stimulation setup was prepared where the rat sciatic nerve was used to test the spatial specificity of the ultrasound cuff stimulator. The hind leg of the sciatic nerve of a rat was exposed and a ultrasound stimulation was applied either with CMUT or PZT which unfortunately ended in unsuccessful results. Table 5.2 summarizes the acoustic parameters that were used for these experiments. The bottom row of the table shows a result from Stephan et al [18], where they stimulated the sciatic nerve of a rat transcutaneously with a peak positive pressure of 22 MPa to 28 MPa at 4 MHz. This is 10 times higher pressure used in our work, which most likely explains

the unsuccessful results of our work. It should be noted that these results were only recently published in 2020 which also made it difficult to make the correct decisions in the experiment. Furthermore, the ultrasound stimulation parameter space is massive, and the parameters to stimulate the nerve may also be related to PRF or intensity, both of which were exhaustively investigated in this work. Therefore, our work has shown cleary that at frequencies between 10 MHz to 20 MHz the ultrasound pressure needs to be higher than what we used.

To achieve such high pressures, for future work, it would be better to use a commercial ultrasound probe with a high frequency with a high acoustic pressure to first confirm that ultrasound stimulation at these high frequencies is possible. Then it should be checked whether the power consumption of such a device is realistic for an implantable device with state-of-the-art ultrasound transducers. If the power consumption is too high, or if there isirreversible damage caused by the acoustic pressure, it does not make sense to create an ultrasound cuff device. Finally, if these results turn out to work, it would be the worthwhile to do another rerun of the work that was done in this chapter to realize an ultrasound cuff device to achieve fascicle level specificity.

Table 5.2: Comparison of sciatic nerve ultrasound nerve stimulation parameters.

Technology	Frequency [MHz]	Beam steering	PP	PRF	Stimulation?	Cited from
CMUT	14.3	Yes	1.1 MPa	1 kHz-90 kHz	No	Our work
CMUT	10 -20	No	2.5 MPa	1 kHz-90 kHz	No	Our work
PZT	1	No	0.25 MPa	1 kHz-90 kHz	No	Our work
PZT	5	No	1.63 MPa	1 kHz-90 kHz	No	Our work
PZT	10	No	2.1 MPa	1 kHz-90 kHz	No	Our work
PZT	20	No	2.2 MPa	1 kHz-90 kHz	No	Our work
PZT	4	No	22 MPa- 28 MPa	0.3 Hz	Yes	Stephan et al. [18]

BIBLIOGRAPHY

[1] S. Kawasaki, V. Giagka, M. De Haas, *et al.*, "Pressure measurement of geometrically curved ultrasound transducer array for spatially specific stimulation of the vagus nerve", in *International IEEE/EMBS Conference on Neural Engineering, NER*, vol. 2019-March, 2019, ISBN: 9781538679210. DOI: 10.1109/NER.2019.8717064.

[2] S. Kawasaki, E. Dijkema, M. Saccher, V. Giagka, J. Schleipen, and R. Dekker, "Schlieren visualization of focused ultrasound beam steering for spatially specific stimulation of the vagus nerve", in *International IEEE/EMBS Conference on Neural Engineering, NER*, vol. 2021-May, 2021, ISBN: 9781728143378. DOI: 10.1109/NER49283.2021.9441225.

[3] G. M. D. Ferrari, H. J. G. M. Crijns, M. Borggrefe, *et al.*, "Chronic vagus nerve stimulation : a new and promising therapeutic approach for chronic heart failure", *European Heart Journal*, pp. 847–855, 2011. DOI: 10.1093/eurheartj/ehq391.

[4] K. Famm, B. Litt, K. J. Tracey, E. S. Boyden, and M. Slaoui, "A jump-start for electroceuticals", *Nature*, vol. 496, no. 7444, pp. 159–161, 2013, ISSN: 0028-0836. DOI: 10.1038/496159a.

[5] V. A. Pavlov, S. S. Chavan, and K. J. Tracey, "Bioelectronic medicine: From preclinical studies on the inflammatory reflex to new approaches in disease diagnosis and treatment", *Cold Spring Harbor Perspectives in Medicine*, vol. 10, no. 3, pp. 1–16, 2020, ISSN: 21571422. DOI: 10.1101/cshperspect.a034140.

[6] T. Tsaava, T. Datta-Chaudhuri, M. E. Addorisio, *et al.*, "Specific vagus nerve stimulation parameters alter serum cytokine levels in the absence of inflammation", *Bioelectronic Medicine*, vol. 6, no. 1, 2020. DOI: 10.1186/s42234-020-00042-8.

[7] T. Boretius, J. Badia, A. Pascual-Font, *et al.*, "A transverse intrafascicular multichannel electrode (TIME) to interface with the peripheral nerve", *Biosensors and Bioelectronics*, vol. 26, no. 1, pp. 62–69, 2010, ISSN: 09565663. DOI: 10.1016/j.bios.2010.05.010. [Online]. Available: http://dx.doi.org/10.1016/j.bios.2010.05.010.

[8] K. Wang, C. L. Frewin, D. Esrafilzadeh, *et al.*, "High-Performance Graphene-Fiber-Based Neural Recording Microelectrodes", *Advanced Materials*, vol. 31, no. 15, pp. 1–10, 2019, ISSN: 15214095. DOI: 10.1002/adma.201805867.

[9] A. Ghazavi, M. A. González-González, M. I. Romero-Ortega, and S. F. Cogan, "Intraneural ultramicroelectrode arrays for function-specific interfacing to the vagus nerve", *Biosensors and Bioelectronics*, vol. 170, no. June, 2020, ISSN: 18734235. DOI: 10.1016/j.bios.2020.112608.

[10] H. A. Kamimura, A. Conti, N. Toschi, and E. E. Konofagou, "Ultrasound neuromodulation: Mechanisms and the potential of multimodal stimulation for neuronal function assessment", *Frontiers in Physics*, vol. 8, no. May, pp. 1–9, 2020, ISSN: 2296424X. DOI: 10.3389/fphy.2020.00150.

[11] S. S. Yoo, K. Yoon, P. Croce, A. Cammalleri, R. W. Margolin, and W. Lee, "Focused ultrasound brain stimulation to anesthetized rats induces long-term changes in somatosensory evoked potentials", *International Journal of Imaging Systems and Technology*, vol. 28, no. 2, pp. 106–112, 2018, ISSN: 10981098. DOI: 10.1002/ima.22262.

[12] M. D. Menz, O. Oralkan, P. T. Khuri-Yakub, and S. A. Baccus, "Precise Neural Stimulation in the Retina Using Focused Ultrasound", *Journal of Neuroscience*, vol. 33, no. 10, pp. 4550–4560, 2013, ISSN: 0270-6474. DOI: 10.1523/JNEUROSCI.3521-12.2013. [Online]. Available: http://www.jneurosci.org/cgi/doi/10.1523/JNEUROSCI.3521-12.2013.

[13] R. P. Zangabad, J. G. Bosch, F. Mastik, *et al.*, "Real-Time Coded Excitation Imaging Using a CMUT-Based Side Looking Array for Intravascular Ultrasound", *IEEE Transactions on Ultrasonics, Ferroelectrics, and Frequency Control*, vol. 68, no. 6, pp. 2048–2058, 2021, ISSN: 15258955. DOI: 10.1109/TUFFC.2021.3054971.

[14] B. Mimoun, V. Henneken, A. Van Der Horst, and R. Dekker, "Flex-to-rigid (F2R): A generic platform for the fabrication and assembly of flexible sensors for minimally invasive instruments", *IEEE Sensors Journal*, vol. 13, no. 10, pp. 3873–3882, 2013, ISSN: 1530437X. DOI: 10.1109/JSEN.2013.2252613.

[15] J. Blackmore, S. Shrivastava, J. Sallet, C. R. Butler, and R. O. Cleveland, "Ultrasound Neuromodulation: A Review of Results, Mechanisms and Safety", *Ultrasound in Medicine and Biology*, vol. 45, no. 7, pp. 1509–1536, 2019, ISSN: 1879291X. DOI: 10.1016/j.ultrasmedbio.2018.12.015.

[16] J. Badia, A. Pascual-Font, M. Vivó, E. Udina, and X. Navarro, "Topographical distribution of motor fascicles in the sciatic-tibial nerve of the rat", *Muscle and Nerve*, vol. 42, no. 2, pp. 192–201, 2010, ISSN: 10974598. DOI: 10.1002/mus.21652.

[17] M. A. González-gonzález, A. Kanneganti, A. Josh, *et al.*, "Thin Film Multi-Electrode Softening Cuffs for Selective Neuromodulation", pp. 1–15, 2018. DOI: 10.1038/s41598-018-34566-6.

[18] S. A. Lee, H. A. S. Kamimura, M. T. Burgess, and E. E. Konofagou, "Displacement imaging for focused ultrasound peripheral nerve neuromodulation", *IEEE Transactions on Medical Imaging*, vol. 39, no. 11, pp. 3391–3402, 2020. DOI: 10.1109/TMI.2020.2992498.

6

ACOUSTIC PARTICLE SORTING WITH A COLLAPSE-MODE CMUTS

You'll never find rainbows if you're looking down.

Charlie Chaplin

6.1. INTRODUCTION

Acoustic particle sorting is a biocompatible method to sort particles within a microchannel [1], [2].The technique is useful for manipulating micron-size cells or sub-micron size particles for clinical, biological, and chemical research [3]. The two most common methods to achieve acoustic particle sorting is either to use bulk acoustic waves (BAW) or surface acoustic waves (SAW). BAW-based sorting devices use a single lead zirconate titanate (PZT) element attached to a microfluidic device fabricated from a high acoustic impedance material, such as silicon or glass [4], [5]. The width of the microfluidic channel is designed to be an integer multiple of half of the acoustic wavelength, which creates a standing wave within the acoustic channel that can be used to sort particles. SAW-based sorting devices use an interdigitated transducer (IDT) fabricated through deposition and patterning of a thin piezoelectric layer. Due to this photopatternable fabrication process, the acoustic actuation area can be well controlled, therefore SAW-based devices

Parts of this chapter have been published in IEEE MEMS 2022 conference.

are often preferred when they are integrated with other functionalities. However, SAW-based devices have a low throughput because the acoustic signal is only weakly coupled into the microfluidic channel either through the top or bottom surface. Therefore, there is a need for a BAW-based sorting device which can allow for high throughput particle sorting, while maintaining high control over the acoustic actuation area [6].

Over the last two decades, in the field of ultrasound imaging, there has been great improvement in MEMS based ultrasonic transducers (i.e., piezoelectric micromachined ultrasonic transducers (PMUTs) and capacitive micromachined ultrasonic transducers (CMUTs)) [7]. These transducers are meant to couple ultrasound waves into the medium in contact with the transducers. However, during our preliminary investigations using CMUTs, it was noticed that acoustic energy can also couple into the silicon substrate and propagate laterally in-plane through the substrate. For ultrasound imaging, this will create unwanted imaging artifacts. On the other hand, for acoustic particle sorting, the in-plane ultrasound is another method to generate ultrasound within a microchannel on the same substrate. In addition, CMUTs are broadband devices which compared to PZT devices allows for an extra degree of freedom to manipulate particles within the microchannel. Furthermore, CMUT technology is highly compatible with silicon microfluidics; a growing field where silicon is used as the substrate to integrate complex functionalities such as cell manipulation, cancer detection, and DNA amplification [8], [9].

This paper is organized as follows. First, the concept of the microfluidic device with CMUTs combined with a silicon embedded microchannel is explained. Next, the sidewall acoustic pressure is measured from a CMUT die. Finally, the alignment of 10 µm particles is demonstrated both in static condition and also within a microfluidic flow.

6.2. DEVICE CONCEPT

The main components of a BAW-based microfluidic particle sorting device are the microfluidic channel and the CMUT. In this section, these two components will be explained.

6.2.1. CMUTS

A schematic cross-section of a CMUT is shown in Fig. 6.1. A CMUT consists of a top and bottom circular membrane, each fabricated from an aluminum electrode that is passivated by a isolating layer such as SiO_2 or Si_3N_4 [10]. In its non-biased state, the CMUT has a vacuum gap between its top and bottom membrane. The top membrane is brought into collapse-mode operation by applying a DC bias voltage beyond the pull-in

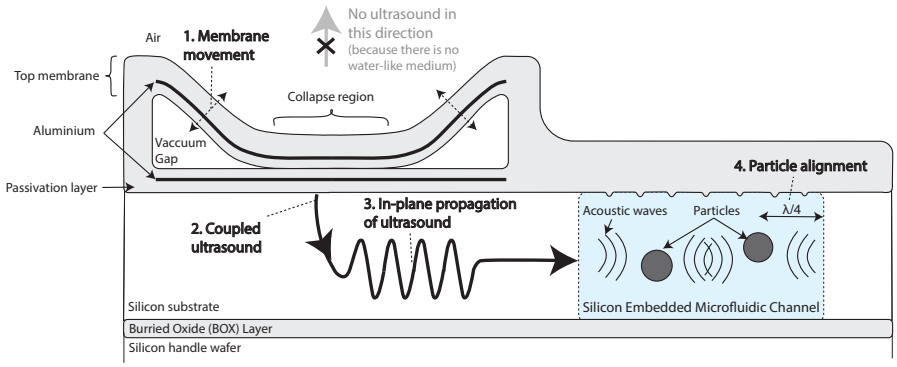

Figure 6.1: Conceptual diagram of the CMUT combined with silicon embedded microfluidic channels. The ultrasound is generated at the CMUT and some of the acoustic energy is coupled into the silicon substrate where it propagates through the silicon substrate in the in-plane direction. A silicon embedded microfluidic channel is fabricated on the same wafer to used the coupled ultrasound to sort particles. The figure is not drawn to scale.

voltage. Then an AC signal is superimposed to vibrate the donut-shaped region around the collapsed area. In conventional operation of the CMUT, a water-like medium is positioned above the membrane to transmit ultrasound into the medium perpendicular to the surface of the silicon. However, in this work the medium is removed and thus, the ultrasound generated from this vibration couples into the substrate through the collapsed region. Subsequently, the ultrasound signal propagates along the in-plane direction of the substrate.

6.2.2. SILICON EMBEDDED MICROFLUIDIC CHANNELS

To efficiently couple the ultrasound energy into a microfluidic channel, the channel must be fabricated on the same substrate, as shown in Fig. 6.1. In our prior work, we developed techniques to fabricate silicon embedded microchannels with vertical side walls through a standardized IC-based fabrication process [11]. Fig. 6.2 shows the fabrication process flow. The fabrication begins with an 8-inch Silicon on Insulator (SOI) wafer with a 40 µm device layer and a micrometer thick BOX layer (Fig. 6.2(a)). A 500 nm thick plasma-enhanced chemical vapor deposition (PECVD) SiO_2 is deposited on the device layer (Fig. 6.2(b)). Afterwards, positive photoresist is patterned on top with the channel design composed of small rectangular openings of 1 µm by 1 µm (Fig. 6.2(c)). Then this pattern is transferred to the SiO_2 layer that was previously deposited using dry etch (Fig. 6.2(d)). Using this as a hardmask the silicon substrate was etched using deep reactive ion etching (DRIE). This recipes is composed of two stages. First, the dry etch

is isotropic and it etches underneath and around the oxide mesh to merge it as a single microchannel (Fig. 6.2(e)). The second stage is an anisotropic etch, down to the BOX layer (FIg. 6.2(f)). Once the channel is etched it is closed by depositing 3 µm of PECVD SiO_2, thereby creating a Si embedded microchannel in the SOI wafer. For the microfluidic channels, a large opening is made at the inlet/outlet to let the fluid in and out.

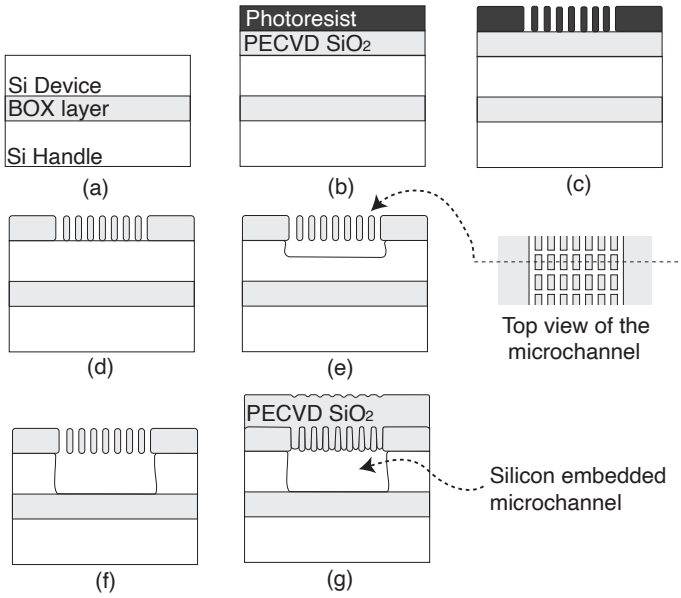

Figure 6.2: Fabrication process of the silicon embedded microchannel.

6.2.3. COMBINING THE TWO DEVICES

Conintegration of CMUTs with the microfluidic channel is not trivial and beyond the scope of this investigation. Therefore the two technologies were combined by gluing the two chips at the side using epoxy (Epotek 301) as shown in Fig. 6.3. Our hypothesis was that as long as the Epotek 301 is thin and hard enough, ultrasound can be coupled into the neighboring chip.

The channel design to test the acoustic particle sorting is shown in Fig. 6.4. The gray area is the chip, the blue area is the microfluidic channel and the ultrasound will be sent from the sidewall at the top of the figure. The microfluidic channel has a width of 375 µm at the center, which corresponds to a wavelength (λ) of 4 MHz. This frequency was chosen because the CMUT has a center frequency around 4 MHz to 5 MHz. In theory, if 2 MHz driving frequency is used, the particles will align at the center of the channel,

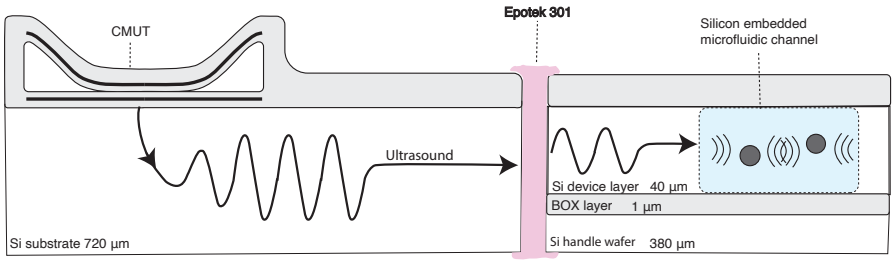

Figure 6.3: Combining the two devices with epoxy (Epotek 301)

while 4 MHz will align the particles along the two node which are quarter of a wavelength from the wall. In Fig. 6.4 the three branches near the inlet/outlet are designed to sort the particles based on these two frequencies. The meander shape near the inlet/outlet was designed so that the fluid velocity was equivalent for all three channels . The design was fine-tuned using COMSOL simulations. The chip at first glance looks empty with only one microfluidic channel at the center, but this was to ensure that there is enough space to create a reliable microfluidic connection.

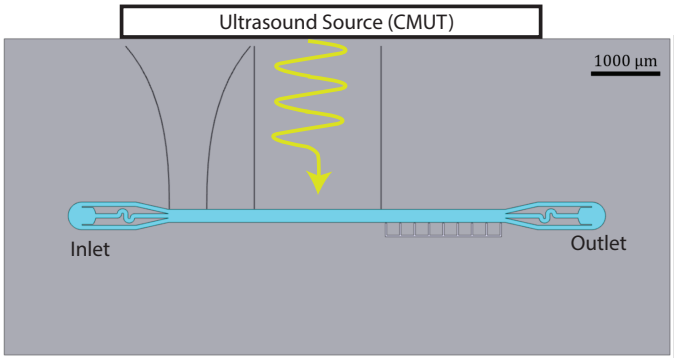

Figure 6.4: The layout of the microfluidic device. The blue area is the microchannel and the gray area is chip.

6.3. RESULTS AND DISCUSSION

In this section, first the acoustic pressure from the side of a CMUT was measured using a hydrophone. Secondly, to further increase the acoustic pressure a phase alignment

method is introduced and tested. Next, particle alignment is demonstrated in a water droplet that contains small latex beads. Finally, the fabrication results of the microfluidic device is shown and particle sorting is demonstrated in a microfluidic flow.

6.3.1. SINGLE ELEMENT ACOUSTIC PRESSURE MEASUREMENT

Fig. 6.5(a) shows an overview of the measurement setup. A droplet of water was placed adjacent to the CMUT die, so that the surface tension kept the water in place. The image taken from the USB microscope above the CMUT is shown in Fig. 6.5(b). The acoustic pressure coupled from the sidewall of the CMUT die was measured with a fiber optic hydrophone (Precision Acoustics, UK) with a tip size of 10 µm diameter. The hydrophone was carefully positioned with a motorized 3D axis stage. The output pressure was relatively insensitive to the vertical position of the hydrophone. Thus, the hydrophone was positioned near half the height of the CMUT die. The diameter of the CMUT membrane used in this work was 355 µm. Each row of CMUTs in Fig. 6.5(b) is referred to as a CMUT element, and has a length of 12 mm, with 33 CMUT devices in each element. These CMUT elements were fabricated with a pitch of 315 µm along the 2 cm height of the die. The element at the very edge of the die is a dummy element and cannot be used. The thickness of the silicon die was 720 µm. The distance between the hydrophone and the silicon sidewall was approximately 0.9 mm.

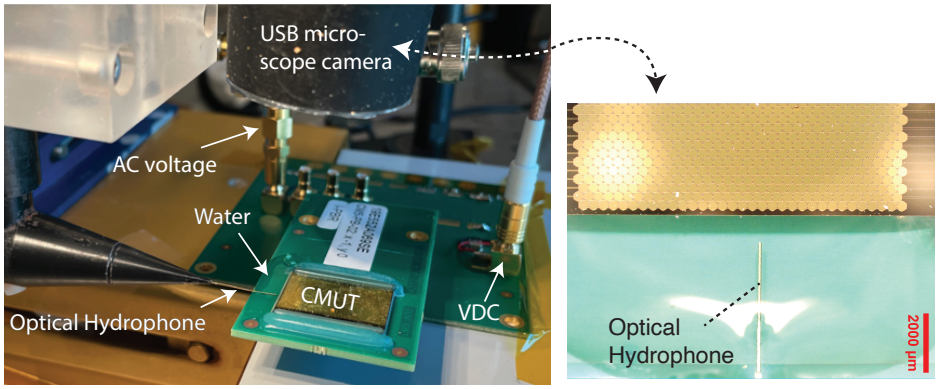

(a) Hydrophone measurement setup (b) USB Microscope image

Figure 6.5: (a) Overview of the acoustic measurement setup to measure the ultrasound generated from the side of CMUT die. (b) Image taken from the USB microscope camera positioned above the CMUT.

Fig. 6.6 shows the driving circuit used for this setup. An AC voltage is generated from a function generator which is amplified with the RF amplifier. The output of the amplifier is connected to the top electrode of the CMUT via a coax cable and the -5dB attenu-

ator. Due to the high frequency and large impedance mismatch between the CMUT and the RF amplifier this becomes a large source of reflection. Thus, the -5dB attenuator, reduces reflections from the CMUT back to the RF amplifier and the 50 Ω load connected immediately after the attenuator is used for impedance matching. The resistive voltage divider of 4.9 kΩ and 50 Ω attenuates the AC voltage to a readable level that can be observed with an oscilloscope. Finally, on the very right side of the figure is a DC bias voltage connected to the bottom electrode of the CMUT through a current limiting resistor of 100 kΩ. The 47 nF capacitors in the circuit are chosen to be orders of magnitude larger than the CMUT capacitor to be used as a decoupling capacitors.

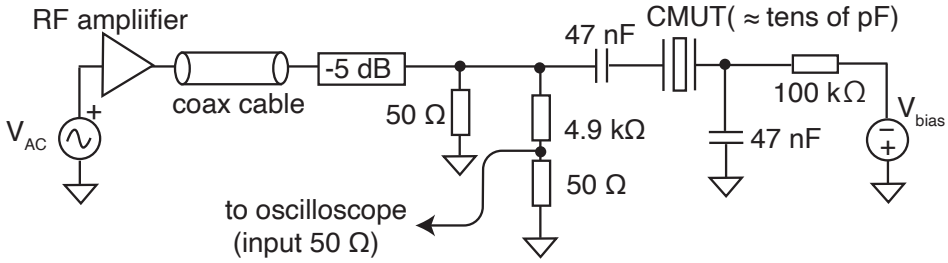

Figure 6.6: Driving circuit of the CMUT for acoustic sidewall pressure measurement.

In order to find the optimal driving frequency and bias voltage, a single CMUT element near the edge of the die was driven with f = *2.5-4.5 MHz*, V_{bias} = *120-150* V_{DC}, V_{ac} = *15* V_{amp}, *waveform = sine, cycle = 1, PRF = 1 kHz.* The measurement was conducted for two CMUT samples and the results were averaged. Figure 6.7 shows the result when (a) the 4th element, (b) the 3rd element and (c) the 2nd element was tested.

In all cases, the output pressure increased at higher frequencies because this is closer to the center frequency of the CMUT. We also see that at higher frequencies the output pressure increases as the bias voltage is increased for all elements. This is a common behavior in immersed ultrasound transducers because the electrical field strength increases. However in this work, it is likely that the large collapse area increased the coupled ultrasound into the substrate. Interestingly, there are opposite behaviours seen at lower frequencies. For example, for the 2nd element (Fig. 6.7(c)), at lower frequencies the output pressure decreases as the bias voltage is increased. This is because a higher pressure is propagating through the silicon in SAW mode. For our current work we focused on the highest pressure that could be generated which occurs at a higher fre-

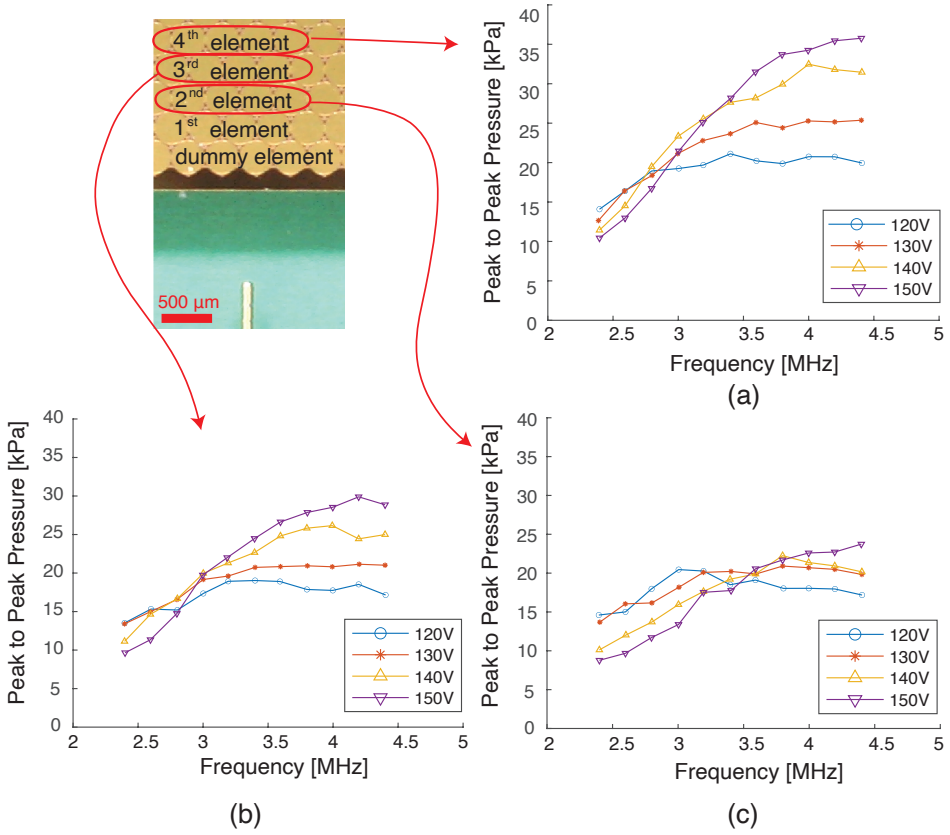

Figure 6.7: The peak to peak pressure seen on the optical hydrophone when (a) the 4th element, (b) the 3rd element and (c) the 2nd element was driven with the following driving conditions : f = 2.5-4.5 MHz, V_{bias} = 120-150 V_{DC}, V_{ac} = 15 V_{amp}, wacefor = sine, polarity = bipolar, cycle = 1, PRF = 1 kHz

quency and higher bias voltage. A typical example of how the transient waveform looks like for these higher pressure parameters is shown in Fig. 6.8. In this figure, the 2nd CMUT element was driven with f = 4.5 MHz, V_{bias} = 150 V_{DC}, V_{ac} = 15 V_{amp}, waveform = sine, , polarity = bipolar, cycle = 1, PRF = 1 kHz. The response showed a ringing behavior because the CMUT membrane has an underdamped response in air.

6.3.2. PHASE DELAY AMPLIFICATION

The maximum pressure generated in the previous measurement went up to a peak value of 40 kPa. In our work we wanted to increase the pressure even further by applying, phase delay amplification. To explain this, in Fig. 6.9 phase delay amplification is achieved by

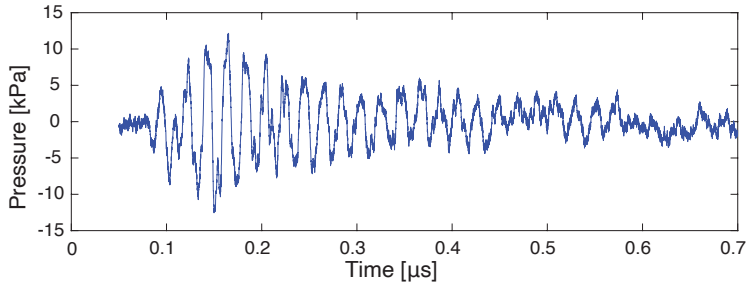

Figure 6.8: Transient waveform of the pressure from the sidewall of the CMUT die.

incrementally delaying the same driving signal for each CMUT element with Δt, such that the ultrasound signal traveling through the substrate is added in phase. In this way, a higher output pressure can theoretically be achieved. The ultrasound waves will add in phase if the following equation is satisfied,

$$v = \frac{D}{\Delta t} \tag{6.1}$$

where D is the pitch between each element and v is the velocity of sound through the substrate. For silicon, v is dependent on the crystal orientation and the vibrational modes that are present. The CMUT devices used in this work have the <110> orientation perpendicular and parallel to the CMUT element. The vibrational mode is not clear and multiple vibrational modes could simultaneously exist. Therefore, in this work, Δt was swept to find the best phase delay amplification condition.

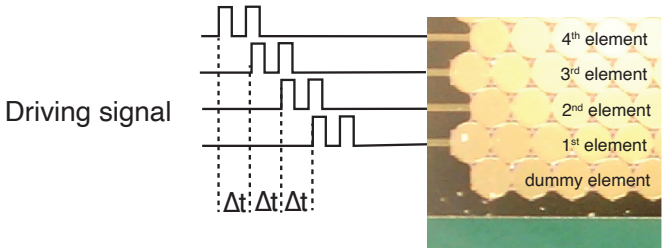

Figure 6.9: The phase delay amplification method.

The 32 CMUT elements closest to the water droplet was driven with the in-house-built ultrasound driver system based on the HV7351 pulser chips (Microchip Technology, USA). The driving signal was *f = 4.5 MHz, V_{bias} = 150 V_{DC}, V_{ac} = 15 V_{amp}, waveform = square, polarity = unipolar/positive, cycle = 15, PRF = 1 kHz.* The acoustic pressure was

measured when Δt was increased from 5 ns to 150 ns in 5 ns steps. From Fig. 6.10, the output pressure constructively interfered when Δt = 40 ns and 65 ns. This corresponds to a sound velocity within silicon at 7875 m/s and 4846 m/s respectively based on equation 6.1. This matches reasonably well with longitudinal velocity (9138 m/s) and transversal velocity (4675 m/s) that has been reported in literature [12]. The maximum peak-to-peak pressure was 0.9 MPa. For comparison, the output pressure of 32 CMUT elements without phase delay amplification is shown in Fig. 6.10 with a dashed line (Δt = 0 ns). The peak-to-peak output pressure was 140 kPa which was 6.4 times lower than when phase delay amplification was applied.

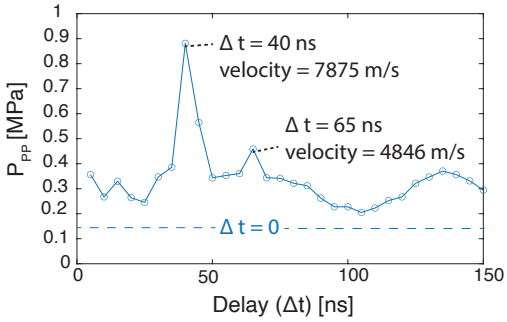

Figure 6.10: Peak-to-peak pressure when phase delay amplification was applied with a time delay from Δt = 5 ns to 150 ns in 5 ns steps. Δt = 0 ns is the peak-to-peak pressure without phase delay amplification.

6.3.3. PARTICLE SORTING IN A STATIC CONDITION

Fig. 6.11(a), is the microscope view of the experimental setup used to demonstrate particle sorting. A droplet of water with 10 µm latex beads was positioned next to the CMUT with a glass reflector at a 4 mm distance from the sidewall of the CMUT. To increase the contrast of the latex beads a thin silicon wafer was positioned beneath the water droplet. In the beginning, the particles were mixed, and there were no distinct patterns. The ultrasound was then turned on for a few seconds, using the same beam steering conditions found to generate the maximum output pressure ($f = 4.5\ MHz$, $V_{bias} = 150\ V_{DC}$, $V_{ac} = 15\ V_{amp}$, *waveform = square, polarity = unipolar/positive, cycle = 15, PRF = 5 kHz*). The PRF was increased to 5 kHz for a slightly higher output power resulting in a duty cycle of 1.7 %. The effect of the ultrasound field on the particles is shown in Fig. 6.11(b). The particles aligned in stripes of 166 µm pitch, which corresponds to half of the wavelength of 4.5 MHz ultrasound in water. The video recording of particle alignment can be seen in this link[1]. The video is not fast-forwarded. In the video, interesting streaming effects are

[1] Acoustic particle sorting : https://youtu.be/NknlrxfTna8

also visible, but the study of this phenomenon was beyond the scope of this work.

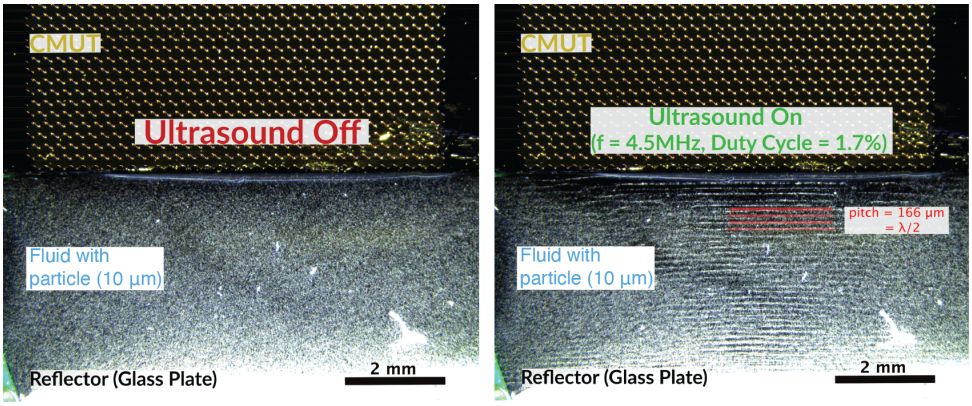

Figure 6.11: Ultrasound 10 µm latex beads sorting, (a) before the ultrasound and (b) after the ultrasound. The ultrasound parameter used: f = 4.5 MHz, PRF = 5 kHz, Vp = 15 V, Vbias = 150 V, Duty Cycle = 1.7 %, Δt = 40 ns, 32 elements, and cycle number = 15.

6.3.4. FABRICATION OF THE MICROFLUIDIC DEVICE

Fig. 6.12(a) is an intermediate fabrication result of the microfluidic channel on a test Si wafer. This figure shows the cross section of the microfluidic channel made immediately after the DRIE step in Fig. 6.2(f). The vertical sidewall guarantees that the ultrasound transmitted from one sidewall would form a standing wave within the channel. The cross section of the top membrane after closure is shown in Fig. 6.12(b). A clean closure of the membrane can be seen, as well as scallops on the sidewall which are by-products of the DRIE process. The size of the scallops in the order of several microns will not have an influence on the result since the ultrasound signal has a much larger wavelength (>375 µm) both in silicon and in water.

6.3.5. PARTICLE SORTING IN A MICROFLUIDIC FLOW

The microfluidic device and the CMUT was assembled together with epoxy as shown in Fig. 6.13. The top figure shows the overview of the assembly and the bottom figure shows the zoomed in image of the microfluidic device. Fig. 6.14 is the setup with the peripheral equipment connected to the microfluidic device. In this setup the ultrasound driver is controlled by the laptop and the syringe pump pushes the water containing 10 µm latex beads at 1 µL/min through the microfluidic device, which is collected in the beaker. The particle behaviour was observed through the microscope while the ultrasound sig-

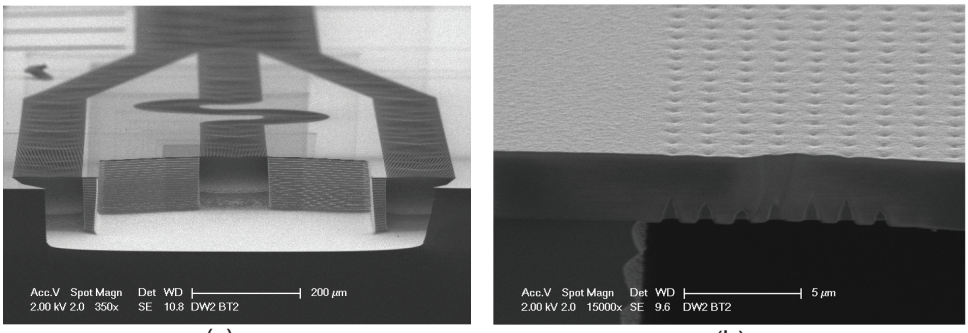

(a) (b)

Figure 6.12: (a) SEM picture 3 branch inlet. (b) SEM picture of the closed membrane.

nal was turned on with the following parameters; f = 2 MHz or 4 MHz, V_{bias} = 150 V_{DC}, V_{ac} = 20 V_{amp}, waveform = square, polarity = unipolar/positive, cycle = 15, PRF = 15 kHz, Δt = 40 ns. Two frequencies (2 MHz and 4 MHz) were tested where it was expected that the sorting will occur at different nodes. Unfortunately particle sorting was not observed for 2 MHz, likely due to the lower acoustic pressure (see Fig. 6.7). However, for 4 MHz, particle sorting was clearly observed. Fig. 6.15 shows the particle sorting after 3 seconds of sorting observed midway in the microchannel for a low particle density. The image on the top is what was recorded on the microscope. This image was post-processed by filtering the background to achieve the figure at the bottom and by averaging the gray value along the length of the channel to obtain the normalized intensity profile. As indicated in the figure, the particle aligned at quarter of wavelength from the side. The other node was not visible for this sample due to imperfect assembly using glue. In contrast, Fig. 6.16 shows the result when the particle density was increased. In this case the particle position has a broader distribution but the peaks are positioned exactly at the correct nodes.

6.4. CONCLUSION

In this work a novel CMUT-based acoustic microfluidic device was proposed, assembled and tested. The maximum output peak-to-peak pressure of 0.9 MPa achieved in this work is substantially higher compared to other works on acoustofluidic separation [4]. This was accomplished through a phase delay amplification technique which aligned the ultrasound signal to add in phase within the Si substrate. This improved the output pressure by 6.4 times compared to when no phase delay amplification was used. Using this tecnique a particle sorting experiment was conducted both in a static condition

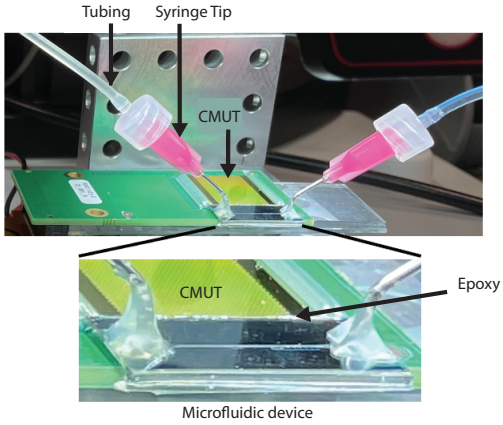

Figure 6.13: The microfluidic device and the CMUT assembled together.

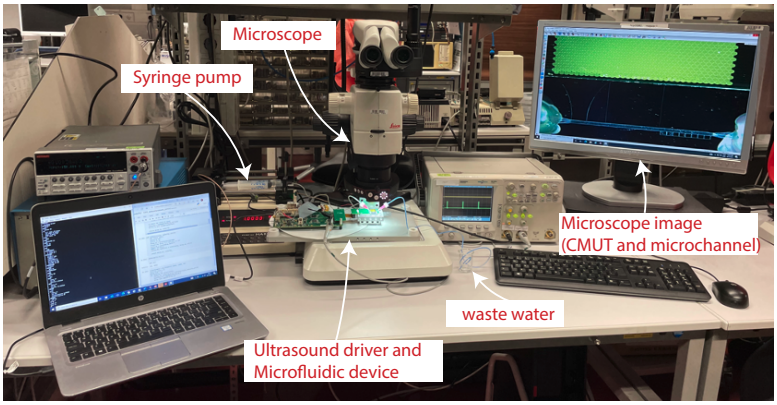

Figure 6.14: Setup to measure the acoustic focusing of the ultrasound driver

and also in a microfluidic flow. In both conditions the particle aligned happened within seconds. In conclusion, this CMUT-based sorting method has great potential as a particle sorting technique in lab-on-a-chip systems. The ability to selectively excite different CMUT elements with the possibility of extra pressure with phase alignment, the broad bandwidth, batch fabrication, and IC integration are the main advantages of the current device over existing acoustic sorting devices. For future research, it is recommended to integrate the CMUTs on the same die, which will significantly improve the performance compared to what has been reported in this work.

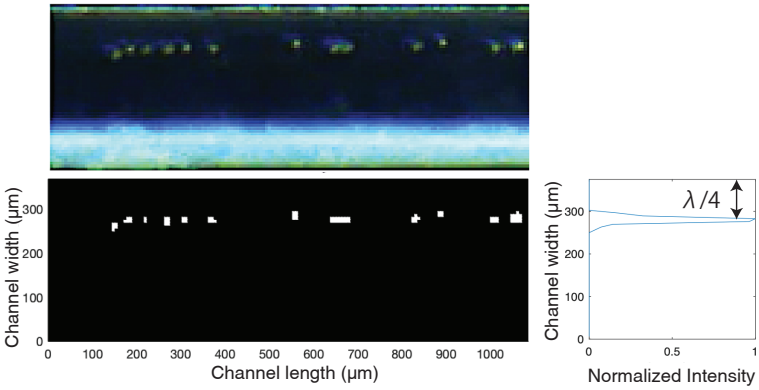

Figure 6.15: Low density particle sorting along the microfluidic channel

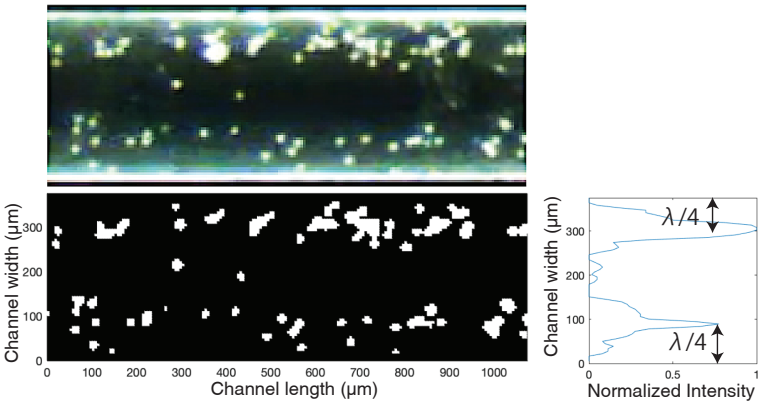

Figure 6.16: High density particle sorting along the microfluidic channel

BIBLIOGRAPHY

[1] L. Ren, Y. Chen, P. Li, *et al.*, "A high-throughput acoustic cell sorter", *Lab on a Chip*, vol. 15, no. 19, pp. 3870–3879, Aug. 2015, ISSN: 14730189. DOI: 10.1039/c5lc00706b.

[2] S. J. Lo and D. J. Yao, *Get to understand more from single-cells: Current studies of microfluidic-based techniques for single-cell analysis*, Jul. 2015. DOI: 10.3390/ijms160816763.

[3] E. Jacob-Lopes, R. Gaspar Bastos, L. Regestein, *et al.*, "Microfluidics for Biotechnology: Bridging Gaps to Foster Microfluidic Applications", 2020. DOI: 10.3389/fbioe.2020.589074. [Online]. Available: www.frontiersin.org.

[4] Y. Gao, M. Wu, and Y. Lin, "Acoustic Microfluidic Separation Techniques and Bioapplications : A Review", 2020.

[5] G. P. Gautam, T. Burger, A. Wilcox, M. J. Cumbo, S. W. Graves, and M. E. Piyasena, "Simple and inexpensive micromachined aluminum microfluidic devices for acoustic focusing of particles and cells", *Analytical and Bioanalytical Chemistry*, vol. 410, no. 14, pp. 3385–3394, May 2018, ISSN: 16182650. DOI: 10.1007/s00216-018-1034-6.

[6] M. Wu, A. Ozcelik, J. Rufo, Z. Wang, R. Fang, and T. Jun Huang, "Acoustofluidic separation of cells and particles", *Microsystems and Nanoengineering*, vol. 5, no. 1, 2019, ISSN: 20557434. DOI: 10.1038/s41378-019-0064-3.

[7] J. Joseph, B. Ma, and B. T. Khuri-Yakub, "Applications of Capacitive Micromachined Ultrasonic Transducers: A Comprehensive Review", *IEEE Transactions on Ultrasonics, Ferroelectrics, and Frequency Control*, vol. 69, no. 2, pp. 456–467, Feb. 2022, ISSN: 0885-3010. DOI: 10.1109/TUFFC.2021.3112917.

[8] H. M. Ji, V. Samper, and Y. Chen, "Silicon-based microfilters for whole blood cell separation", pp. 251–257, 2008. DOI: 10.1007/s10544-007-9131-x.

[9] K. De Wijs, C. Liu, A. Dusa, *et al.*, "Micro vapor bubble jet flow for safe and high-rate fluorescence-activated cell sorting", *Lab on a Chip*, vol. 17, no. 7, pp. 1287–1296, 2017, ISSN: 14730189. DOI: 10.1039/c6lc01560c.

[10] M. Pekař, S. H. van Nispen, R. H. Fey, S. Shulepov, N. Mihajlović, and H. Nijmeijer, "A fluid-coupled transmitting CMUT operated in collapse mode: Semi-analytic modeling and experiments", *Sensors and Actuators, A: Physical*, vol. 267, no. 2017, pp. 474–484, 2017, ISSN: 09244247. DOI: 10.1016/j.sna.2017.09.055. [Online]. Available: http://dx.doi.org/10.1016/j.sna.2017.09.055.

[11] M. Kluba, A. Arslan, R. Stoute, J. Muganda, and R. Dekker, "Single-Step CMOS Compatible Fabrication of High Aspect Ratio Microchannels Embedded in Silicon", *Proceedings*, vol. 1, no. 10, p. 291, 2017, ISSN: 2504-3900. DOI: 10.3390/proceedings1040291.

[12] M. K. Song and K. Y. Jhang, "Crack detection in single-crystalline silicon wafer using laser generated Lamb Wave", *Advances in Materials Science and Engineering*, vol. 2013, 2013, ISSN: 16878434. DOI: 10.1155/2013/950791.

7

CONCLUSION AND FUTURE WORK

7.1. CONCLUSION

The main motivation of this work was to find novel application areas for the collapse-mode CMUTs which cannot be addressed with conventional bulk PZT technology. Here we briefly review the key contributions from this work.

CHAPTER 2

The semi-analytical reduced order model of a collapse-mode CMUT was extended with a built-in charge layer. The experimental data was compared to the model showing that the dominant charge mechanism is a dipole within the CMUT. This is caused by the oxygen vacancies within the Al_2O_3 layer repositioned by the electrons that tunnel into the Al_2O_3 layer.

CHAPTER 3

The pre-charged collapse-mode CMUT was characterized showing in both transmission and in reception. The -6 dB bandwidth of pre-charged collapse-mode CMUT device was 113 % with a center frequency of 5.1 MHz. The transmit sensitivity and the receive sensitivity was 0.88 MPa/100 V and 10 V/MPa respectively. When the CMUT was optimally loaded with a matching inductor and a resistor, the power conversion efficiency measured from the surface of the CMUT to the resistive load was 42 % to 47 % which is better than other ultrsound transducer technology.

CHAPTER 4

The pre-charged collapsed-mode CMUT was shown that it could communicate with an external ultrasound source by means of backscattering. In the first part of this chapter a backscattering scheme with on-off keying was implemented to communicate the amount of power to the external ultrasound source. In the second part of this chapter a time-reversal beam forming technique based on the backscattered signal was implemented to instantaneously locate the implant.

CHAPTER 5

Ultrasound nerve stimulation with an ultrasound cuff device was tested. In this work the ultrasound cuff device was assembled, characterized and the beam forming capabilities were verified. Afterwards ultrasound neurostimulation was tested on the sciatic nerve of a rat, which unfortunately ended in failure. A spatial peak acoustic pressure of nearly 2 MPa amplitude at a center frequency of 14.3 MHz was not sufficient to illicit an action potential. The reason could be due to the thick myelin sheath that is protecting the nerve.

CHAPTER 6

The CMUT device was tested in air to see whether the ultrasound energy could be coupled to the sidewalls of the die where it could be used for particle sorting application for lab on a chip devices. It was shown that nearly 1 MPa of pressure can be generated if multiple CMUT elements was operated in-phase.

7.2. FUTURE WORK

The future work is split in to three main categories; i) Pre-charged collapse-mode CMUTs, ii) Ultrasound nerve stimulation and iii) Acoustic particle sorting.

PRE-CHARGED COLLAPSE-MODE CMUTS

1. The bandwidth and sensitivity of the pre-charge collapse-mode CMUT drifts as the built-in charges redistribute within the charge storage layer. Therefore, a charge storage layer which can increase the charge retention time should be investigated.

2. The matching inductor that is required to tune off the electrical capacitance of the CMUT should be removed or minimized in order to save space, especially for power receiving applications. One potential idea would be to divide the bottom electrode of the CMUT into two parts. One part should be a circular plate beneath the collapse-region and the other part should be a donut-shaped ring region corresponding to the area beneath non-collapsed region. This will remove the large

dead capacitance that is under the collapse-region and would allow higher receive sensitivity for the device because less capacitance is loading the circuit. Consequently, if the electrical capacitance of a CMUT has a high impedance, the matching inductor could be removed because most of the current will flow to the resistive load with a lower impedance.

3. Finally, one should create a B-mode image with the pre-charged collapse-mode CMUT. The high sensitivity and broad bandwidth that was obtained in this work shows ample evidence that this should work, however a clear demonstration is worth a thousand words.

ULTRASOUND NERVE STIMULATION

1. The ultrasound parameters to stimulate the sciatic nerve or the vagus nerve should be investigated with high intensity focused ultrasund transducers that are commercially available at frequencies above 10 MHz.

2. Once the parameter to achieve ultrasound stimulation is found, acoustic simulation should be used to determine whether the ultrasound cuff concept is theoretically feasible in terms of its energy consumption, heat dissipation and safety as an implantable device.

3. The device should be fabricated and tested in-vivo as it was done in this work.

ACOUSTIC PARTICLE SORTING

1. The CMUT should be combined with a microchannel which is located on the same substrate. This will maximize the amount of pressure coupled into the microchannel.

2. To maximized the beam forming and amplification effect of the CMUT, one could use a fan shaped layout of the CMUT as was shown for SAW based acoustic sorting devices.

ACKNOWLEDGEMENTS

The first acknowledgement goes to Ronald. It was an honor to work at your lab with the tools and expertise that you provided. Working next to someone like you with so many brilliant ideas made my PhD into a roller coaster journey in which I was able to touch upon tremendous number of different topics. I also have to thank you for my current job at TNO Holst Center where you connected me with Jeroen van den Brand which was an excellent life decision for me. Since I will still be working on ultrasound I am looking forward to future collaborations with you.

The second acknowledgement goes to Marta Saccher. You were my first master student and then became a PhD colleague afterwards. When I think of you I remember all of the nice trips that we had together. In the beginning we went to Rotterdam and we did experiments with rat brain slices. Then we went to do experiments together at Amsterdam and Darmstadt with rat sciatic nerves. Meanwhile we also went to Brugge for a conference which was probably one of the nicest conference experience (not virtual!!). I admire the drive that you have inside of you, and I must thank you for the effort that you are putting into the co-authored paper. I hope we still have topics that overlap in the future in which we could work together.

Then I would like to thank, Jian Li who I have known for such a long time now (more than 8 years) and whom I have shared my office with for the last 4 years. Funnily enough, most of our conversation was never about science and it was always about gossips about others. Such conversations were fun to have with you and I miss having you as my office mate. I also would like to thank you for the hospitality and kindness that you brought to the group by hosting hotpot events at your place and bringing nice sweets to the office.

Enormous thanks to Lambert Bergers. When we were sharing the office, I enjoyed your company because I could always rely on you to bounce off ideas that I had which were not so clear. You were always patient in listening to my explanation that often comes out as mumbo-jumbo and you always found some eloquent way to clarify my thoughts. Currently, you are my landlord, ex-colleague, and sometimes my bouldering buddy. Thank you so much.

Also thanks to Shivani Joshi, Angel Savov and Ronald Stoute who helped me at the beginning of my PhD and introduced me to the PhD group in Philips.

I was lucky to supervise a lot (and I mean a lot!!) of master students during my PhD. In my second year in my PhD I supervised Youri Westhoek, Eric Dijkema and Sevda Malek Kani. Youri surprised me with his excellence in designing 3D structures and his precision during ultrasound experiments. His designs were so nice that I used it over and over even after he finished his degree. Thank you so much. Eric had one of the most challenging projects for a master student but he managed to work it through with his strong perseverance. I think most students will not be able to do achieve anything close to what he did and therefore, I would like to thank him for his hard work. Sevda perhaps surprised me the most with her ability to get others involved. She was able to independently figure out what she needed and involve other when she needed help. I also had two master students in my third year whom I would like to thank; Indu and Jia-Jun. Indu was helpful because she pushed me to write a paper and she was always enthusiastic about her work which gave me energy. Jia-Jun was excellent in research, being both practical and theoretical. But above all she persuaded me to run in the high tech campus run (10 km) which I must thank her for pushing my boundaries. On my fourth year I had the chance to partially supervise Sai. Sai was a great writer and a researcher and he was especially a fast learner and was up in running very early in his work and I enjoyed working with him.

I was fortunate to work with people in Philips and to work with great minds. First thanks goes to Chris van Heesch. You were probably one of the first person that I got to know at Philips and I spent most of my time with you prior to Covid and learned a lot about new setups and how they work (i.e. hydrophone setup, verasonics, wup system, impedance analyzer, and etc.) Secondly, I would like to thanks Eugene. I think it is quite difficult to tolerate someone like me who makes a mess everywhere in the lab. But you were patient and let me freely use the lab. Thirdly, I would like to thank, Peter Dirksen and Sergei Shupelov. The two master mind behind everything related to ultrasound. Both of you taught me a great deal about ultrasound. Then I would like to thanks Peter Loebl. I think I learned alot from you about the characterization method of CMUT devices but it was also a lot of fun to work with you on the schlieren setup together. I also would like to thanks Rob van Schaijk and Johan Klootwijk. The work we did together on the topic of pre-charged CMUTs was extremely interesting and I am confident that this will be used in the future. Also many thanks to Peter Blanken. I really admired your ability to reduce ultrasound physics to electrical circuits and it opened up my mind. Above all, I must thank Hans Huibert for letting me work in his group during my PhD.

Finally, I would like to thank my family. My mom Arisa and dad Kenichi for bringing me up until now and being patient with me living abroad doing my studies in such a far

away place. My sister Kurenai for her exciting energy that she brings to the family. My brother-in-law Saiichi for his hardworking attitude and fun vibe that is infectious and inspires me a lot. My nephew, Tsuzumi and Amane for their cuteness that they bring to the family.

A

DERIVATION OF THE CMUT MODEL

A.1. ELECTRIC FIELD CALCULATION

Referring to G. M. Sessler[1] eq. 16 and eq. 19 the electric field through the equivalent dielectric stack is as follows,

$$\begin{aligned} sE_1 &= V - V_{eff} && x_1 \le x < 0 \\ sE_2(x) &= \frac{V - V_{eff}}{\varepsilon_{SiO_2}} + \frac{\sigma_1 + \hat{\rho}_m x}{\varepsilon_0 \varepsilon_{SiO_2}} && 0 \le x < \hat{t}_3 \\ sE_2 &= \frac{V - V_{eff}}{\varepsilon_{SiO_2}} + \frac{\hat{\rho}_m \hat{t}_3}{\varepsilon_0 \varepsilon_{SiO_2}} && \hat{t}_3 \le x < x_2 \end{aligned} \tag{A.1}$$

where $s = \sum x_i/\varepsilon_i$, $V_{eff} = \frac{x_2 \hat{\sigma}_1}{\varepsilon_0 \varepsilon_{SiO_2}}$ where $\hat{\sigma}_1$ is defined according to eq. 2.9. Using this result, by correcting the electric field for the original dielectric constants, the electric field between the top to bottom layer is shown in Fig. A.1. The induced charge on the top and bottom electrode, σ_{top} andσ_{bottom} are respectively,

$$\sigma_{top} = \varepsilon_0 \frac{V - V_{eff}}{s} \tag{A.2}$$

[1] G. M. Sessler, "Electric Fields and Forces due to Charged Dielectrics," Journal of applied physics, vol. 43, no. November 2003, pp. 405–408, 1972. DOI: 10.1063/1. 1661128.

A

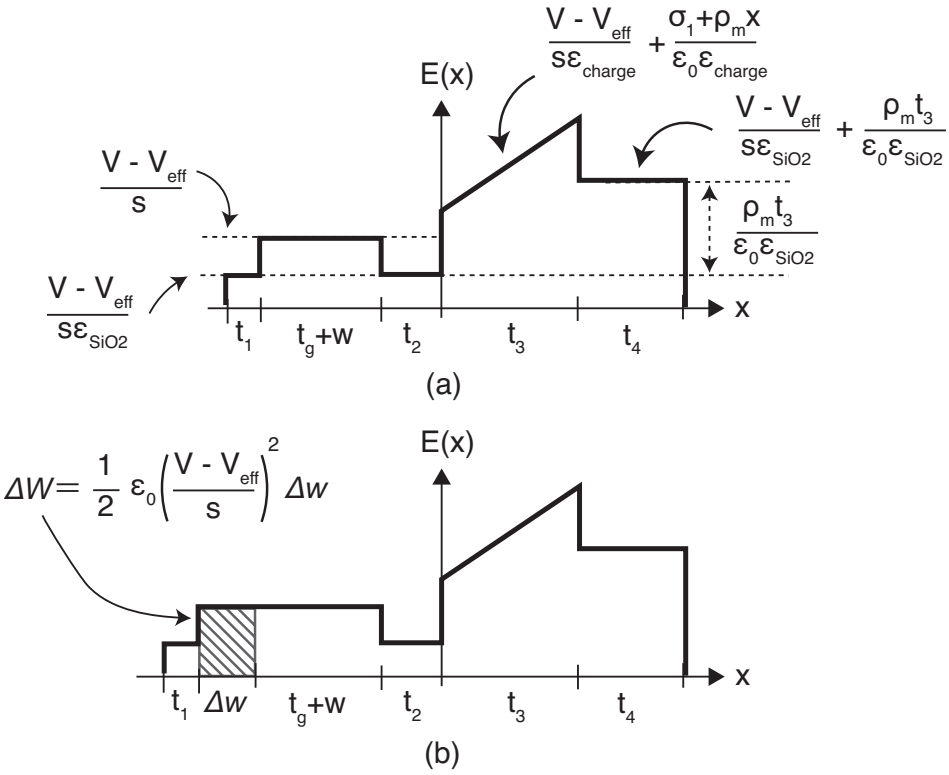

Figure A.1: electric field

$$\sigma_{bottom} = -\varepsilon_0 \frac{V - V_{eff}}{s} - \rho_m t_3 = -\sigma_{top} - \rho_m t_3 \tag{A.3}$$

The total energy W that within this layer stack is expressed with the following integral,

$$W = \int \frac{1}{2} \varepsilon_0 \varepsilon_r(x) E(x)^2 \, dx \tag{A.4}$$

However, without calculating the integral, the electrostatic pressure acting on the membrane can be solved because the change in electric field only occurs at the vacuum gap. In other words the force acting on the top membrane is the ratio between the change in total energy ΔW and the change in displacement Δw.

$$P = -\frac{\partial W}{\partial w} = -\frac{\Delta W}{\Delta w} \tag{A.5}$$

Fig. A.1(b) shows the distance between the top and bottom plate increased by Δw

and the additional energy stored by increasing the gap size is the contribution of the shadowed region which is,

$$\Delta W = \frac{1}{2}\varepsilon_0 \left(\frac{(V - V_{eff})}{s}\right)^2 \Delta w \tag{A.6}$$

Including this into eq. A.5 the pressure acting on the top plate is,

$$P = -\frac{1}{2}\varepsilon_0 \left(\frac{(V - V_{eff})}{s}\right)^2 \tag{A.7}$$

which is acting on the opposite direction of the displacement shown by the negative symbol.

A.2. SOLVING THE MEMBRANE DYNAMICS

Eq. 2.10 is non-dimensionalized as follows,

$$\begin{aligned}\frac{\partial^2 \hat{w}(\hat{r},\hat{t})}{\partial \hat{t}^2} + \nabla^4_{\hat{r}}\hat{w}(\hat{r},\hat{t}) = &-\frac{\hat{V}^2(\hat{t})}{2(1+\hat{w}(\hat{r},\hat{t}))^2} - \frac{\hat{V}^2_{eff}(\hat{r},\hat{h})}{2(1+\hat{w}(\hat{r},\hat{t}))^2} \\ &+ \hat{\mathrm{H}}_{\mathrm{ab}}\mathrm{erfc}\left(\frac{\hat{t_g} + \hat{w}(\hat{r},\hat{t})}{\hat{\sigma}}\right) + \frac{\hat{\tau}}{\hat{r}}\frac{\partial}{\partial \hat{r}}\hat{r}\frac{\partial \hat{w}(\hat{r},\hat{t})}{\partial \hat{r}}\end{aligned} \tag{A.8}$$

The "∧" symbol denotes that the values are nondimensionalized. The detailed process can be followed in the works by M. Pekar et al.[2]. To solve for the transversal displacement $\hat{w}$, the solution is approximated with a linear combination of n independent basis function $\phi_i(r)$

$$\hat{w}(\hat{r},\hat{t}) \approx \sum_{i=1}^{n} q_i(\hat{t})\phi_i(\hat{r}) \tag{A.9}$$

By this conversion the partial differential equation (eq. A.8) could be converted to n sets of ordinary differential equation where the coefficients q_i for i = 1 to n can be solved using the Galerkin approach. The basis function $\phi_i(\hat{r})$ are chosen to be the undamped axisymmetric eigenmodes of a circular plate determined by,

$$\phi_i(\hat{r}) = \frac{J_0(\hat{r}\sqrt{\Omega_i})}{J_0(\sqrt{(\Omega_i)})} - \frac{I_0(\hat{r}\sqrt{\Omega_i})}{I_0(\sqrt{(\Omega_i)})} \tag{A.10}$$

[2] M. Peka˘r, S. H. van Nispen, R. H. Fey, S. Shulepov, N. Mihajlovi c, and H. Nijmeijer, "A fluid-coupled transmitting CMUT operated in collapse mode: Semi-analytic modeling and experiments," Sensors and Actuators, A: Physical, vol. 267, no. 2017, pp. 474–484, 2017, ISSN: 09244247. DOI: 10.1016/j.sna.2017.09.055. [Online]. Available: http://dx.doi.org/10.1016/j.sna.2017.09.055.

where J_0 and I_0 are the Bessel function of the first kind and the modified Bessel function of the first kind respectively. Ω_i is the i the non dimensional natural angular frequency. The non-dimensional natural frequency are based on A. W. Leissa [3].

This way of choosing the basis function allows us to simplify the biharmonic operator as,

$$\nabla_r^4 \phi_i(r) = \Omega_i^2 \phi_i \tag{A.11}$$

$$\int_0^1 \phi_i(r)\phi_j(r) r dr = \delta_{ij} \tag{A.12}$$

where δ_{ij} is the Kronecker delta.

[3] A. W. Leissa, "Vibration of plates," Tech. Rep. Special Publication (SP), 1969, pp. 1– 413.

B

Neural Engineering Conference 2019 and 2022

Pressure measurement of geometrically curved ultrasound transducer array for spatially specific stimulation of the vagus nerve

S. Kawasaki, V. Giagka, M. de Haas, M. Louwerse, V. Henneken, C. van Heesch, and R. Dekker

***Abstract*— Vagus nerve stimulators currently on the market can treat epilepsy and depression. Recent clinical trials show the potential for vagus nerve stimulation (VNS) to treat epilepsy, autoimmune disease, and traumatic brain injury. As we explore the benefits of VNS, it is expected that more possibilities for a new treatment will emerge in the future. However, existing VNS relies on electrical stimulation, whose limited selectivity (due to its poor spatial resolution) does not allow for any control over which therapeutic effect to induce. We hypothesize that by localizing the stimulation to fascicular level within the vagus nerve with focused ultrasound (US), it is possible to induce selective therapeutic effects with less side effects.**

A geometrically curve US transducer array that is small enough to wrap around the vagus nerve was fabricated. An experiment was conducted in water, with 48 US elements curved in a 1 mm radius and excited at 15 MHz to test the focusing capabilities of the device. The results show that the geometrical curvature focused the US to an area with a width and height of 110 µm and 550 µm. This will be equivalent to only 2.1% of the cross section of the vagus nerve, showing the potential of focused US to stimulate individual neuronal fibers within the vagus nerve selectively.

I. Introduction

Currently marketed vagus nerve stimulators are used to treat epilepsy and depression [1] by stimulating the vagus nerve. Vagus nerve stimulation (VNS) works by implanting a cuff electrode directly onto the vagus nerve located at the neck. Since the vagus nerve is a bundle of nerves that includes efferent nerves connecting to many organs other than the brain (i.e. heart, lung, spleen, stomach etc.) recent clinical trials have begun to explore VNS as a method to modulate these other organs for therapeutic benefits. Some examples of these clinical trials target chronic heart failure [2] or autoimmune diseases [3] such as Crohn's disease or rheumatoid arthritis. However, the side effects of these therapies still remain; these include neck pain, coughing, voice alteration, and dyspnea [4]. Therefore, the goal of this paper is to explore a new stimulation technique, which has the potential to induce therapeutic effect that targets only one of the previously mentioned diseases, while reducing the side effects by localizing the stimulation to individual fascicles within the nerve.

One option that was explored by T. Stieglitz et al. was to mechanically pierce through a peripheral nerve and distribute highly selective electrode contacts over the cross section of the nerve, which can create localized activation at the fascicular level [5]. This method was proven to work for motor nerves. Nonetheless, to our knowledge this concept has not been applied to the vagus nerve, most likely because the vagus nerve has vital functions and is too risky to penetrate with such a device. Another option investigated was to use multiple electrodes along the inner walls of a cuff that can be excited independently (i.e. multi-contact electrode [4], [6]). For this method, additional advancement must be made to increase the number of electrodes to achieve better spatial resolution.

As an alternative approach, we propose focused ultrasound (US) to stimulate individual fascicles within the vagus nerve. It has already been shown that US can stimulate neurons [7]. The stimulation mechanism remains to be unclear, but one possible explanation is that the acoustic force from the US deforms the cell membrane and stimulates the mechano-sensitive ion channels [8]. Transcranial US neurostimulation has been studied extensively over the past decade due to its compelling characteristic to stimulate certain regions deep within the brain but without invasively penetrating the brain [9]. Similarly, we hypothesize that if US transducers are wrapped around the vagus nerve, individual fascicles within the vagus nerve can be stimulated without penetrating the nerve.

For transcranial applications, the US frequency is commonly below 5 MHz, as higher frequency US will not penetrate through the skull. This limits the spatial resolution of the therapy to several millimeters. Unfortunately, this is already too coarse for VNS, as the vagus nerve has a diameter of about 2 to 4 mm at the site of stimulation. However, this resolution can be increased if higher frequencies and a larger number of US transducers are employed. Luckily, operating at higher frequencies is not a limitation for our proposed solution, as the US transducers will be wrapped directly around the vagus nerve.

Only a handful of researchers have conducted in-vivo tests at these frequencies. M. Menz et al. stimulated retinal ganglion cells with US at a frequency of 43 MHz for retinal prosthetic application [10]. This was possible because the retinal cells are directly accessible through the surface of the eye without penetrating the skull. These results indicate that neurons can indeed be activated at higher US frequencies, strengthening our hypothesis that stimulation of neurons within the vagus nerve with such high frequencies should be feasible.

In the past, creating a cuff with US transducers so small that could be wrapped around the vagus nerve would be

*Research supported by ULIMPIA

S. Kawasaki and V. Giagka are with the Microelectronics Department, Delft University of Technology, Delft, The Netherlands (corresponding author e-mail: shinnosuke.kawasaki@philips.com). V. Giagka is also with Fraunhofer Institute for Reliability and Microintegration IZM, Berlin, Germany. M. Louwerse, V.Henneken, C.van Heesch, R. Dekker is with Philips Research, Eindhoven, The Netherlands. M. de Haas is with Philips Innovation Services, Eindhoven, The Netherlands.

unthinkable. Due to the advent of mechanical and electrical micro systems (MEMS) it is now possible to fabricate thousands of US transducers in a few millimeter square area. This allows for a high-resolution US cuff at a size comparable to conventional VNS cuff electrodes.

In this paper, we propose a new high-resolution vagus nerve stimulator. A flexible array of US transducers that can be wrapped around the vagus nerve. This device will have the potential to achieve single fascicle stimulation along with the ability to control the stimulation region by applying a phase delay to each US transducer. Finally, the concept can be extended to all peripheral nerves. Thinner nerves can also be targeted if a suitable spacer with an acoustic impedance similar to water is used between the nerve and the US transducers because US will propagate through the spacer.

The rest of this paper illustrates the focusing capabilities of such a proof-of-concept high-resolution cuff, in a proof-of-concept experiment. A device with 48 US transducer elements (each element consisting of 24 US transducers) was fabricated and positioned in a half-cylinder with 1 mm radius inside the water medium. The array of transducers were excited and the pressure profile in the volume within and above the half-cylinder (where the nerve would be positioned) was measured. To verify measured results, simulations of the US pressure field were also conducted, using the same geometry.

II. Material and Method

A. Sample preparation

Capacitive Micromachined Ultrasonic Transducers (CMUTs) consist of two circular parallel plates with the bottom plate on the silicon substrate and the top plate suspended over the bottom one, with an insulating layer and a vacuum gap in between. By applying an AC signal to the two plates, the distance between them changes generating US. An additional DC voltage can be applied either to tune the center frequency or to increase the amplitude of the US [11].

The CMUT devices were fabricated through MEMS microfabrication. Each features with a diameter of 25 µm and 24 of them were aligned on a single silicon island with 2 µm spacing between two adjacent CMUT devices. This silicon island will be referred to as a CMUT element. On the same wafer, 112 of these CMUT elements were aligned next to each other with 2 µm spacing. The Flex-to-rigid process [12], [13] was employed to use polyimide as a flexible layer that connects all elements, thus creating a flexible device which can curve.

The array of CMUT elements was fixed in a curvature along the inner wall of a half-cylinder with an inner radius of 1 mm. This was placed on top of a PCB and was wire bonded to connect to external connectors. Subsequently, the device was coated with 20 µm of PDMS and 5 µm of Parylene. The PDMS served as an acoustic matching layer between the CMUT and water. The parylene on top of it prevented PDMS from absorbing water and avoided short circuits at the electrical connectors. Fig. 1a shows an overview of the prepared sample before it was coated with PDMS and Parylene. Fig. 1b is a close up image of the CMUTs.

B. Experimental setup

Fig. 2a shows the experimental circuit. A 5 V DC bias was connected to all of the CMUTs through a 100 kΩ resistor. The 48 CMUT elements at the center of the device were connected in parallel and were excited simultaneously. An US tone burst of 15 MHz at a pulse repetition frequency (PRF) of 1 kHz with 30 cycle was generated with a function generator (Keysight Model 3621A). This signal was amplified through an amplifier up to 17 V peak-to-peak voltage to excite the CMUT elements via a decoupling capacitor (47 nF). This input RF signal was measured across a 100:1 voltage divider. The acoustic pressure was measured with an optical fiber pressure sensor along with the fiber optic hydrophone (Precision Acoustics).

Fig. 2b is a side view of the CMUT immersed inside water during the measurement. The optical fiber pressure sensor with a tip diameter of 0.1 mm was positioned from the top. Water was used as the acoustic medium to mimic the acoustic property of a nerve, since sound velocity is relatively similar for water (1500 m/s) and nerve (1630 m/s). Using water also confirms that the device is watertight and can be extended to in-vitro experiments in the future.

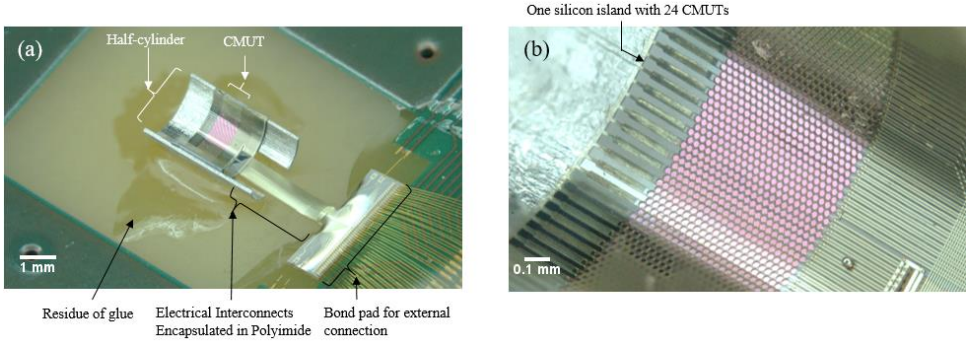

Figure 1. (a) Overview of curved CMUT wire bonded to a PCB before coating of PDMS and Parylene. The CMUT elements were glued to the half-cylinder which was then glued to the PCB. The electrical interconnects are encapsulated in polyimide which is further connected to the bondpad for external connection. (b) a close up image of the CMUTs with 24 CMUTs in one column and 112 CMUT elements (not shown entirely) in a row. The transparent yellow film encapsulating the islands is the polyimide.

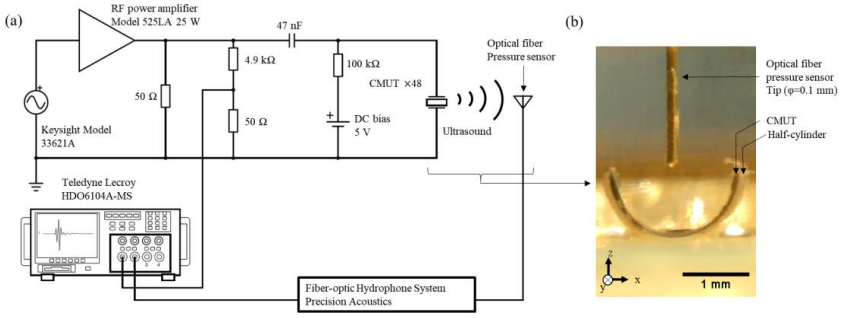

Figure 2. (a) An overview of the experimental circuit. A sine wave with 30 cycles, a center frequency of 15 MHz, and a peak to peak voltage of 17 V at a pulse repetition frequency of 1 kHz, was applied to 48 CMUT connected in parallel via an RF power amplifier and a decoupling capacitance 47 nF. The DC bias voltage was supplied through a 100 kΩ resistor. (b) The sideview of the measurement setup. The CMUT is aligned in a curvature along the half-cylinder and the optical fiber pressure sensor is positioned within the curvature.

The tip of the optical fiber was moved with a motor controlled micromanipulator in 20 µm steps in the x and z direction shown in Fig. 2b. The y-position was adjusted at the x-z plane with maximum pressure by moving the optical fiber tip in the y-direction (in/ out of plane in Fig. 2b).

C. Simulation of the US pressure field

The US pressure field from the CMUT was simulated with an open source software from Michigan State University, Fast Object-Oriented C++ US Simulator (FOCUS) [14]–[16]. In FOCUS, the US field can be simulated by describing the geometry of the US transducer and the medium in which the US propagates. The US transducer geometry was constructed by aligning 48 rectangular transducer elements into a curvature with a radius of 1 mm. Each rectangular element represents a single CMUT element. The width and height of the rectangle element was 25 µm and 0.65 mm respectively. The spacing between each transducer was 2 µm.

The simulation was done in a continuous wave mode and the medium used for the simulation was water. The pressure was simulated on the x-z plane at y = 0, which is the center of the US transducer element.

III. Results

Fig. 3a is the measured pressure field. The instantaneous spatial peak pressure (P_{peak}) was 310 kPa. The width and length of the focal area defined by the -3dB level (shown with a black contour) was 110 µm and 570 µm respectively. The experimentally scanned area is relatively small compared to the size of the half-cylinder. This was because a larger measurement area requires a quadratic increase in the experimental time.

To put this result in perspective, Fig. 3b is the simulation result of a larger US field and Fig. 3c is the close up view where the measurement was conducted. The white circle has a radius of 1 mm and represents the vagus nerve. The red dot are where the 48 CMUTs were positioned.

From both the simulations and the experiments, the focal area is elongated in the vertical direction because the 48 CMUT transducers were aligned at the bottom of the half-cylinder. An interference pattern can also be seen, radiating outwards from the US transducer. This is because the US transducers were stimulated at the same amplitude. The focal area size from the experiment was 6.50×10^4 µm^2. Assuming that the vagus nerve has a diameter of 2 mm, the ratio between the focal area to the cross section of the vagus nerve was 2.1 % from the experiment. This was larger than the simulation result as can be seen by comparing Fig. 3a and Fig. 3c. One possible reason for this is that the measured sample was tilted.

The spatial peak pulse average intensity (I_{SPPA}) of US can be calculated by the following equation,

$$I_{SPPA} = \frac{P_{peak}^2}{2Z_0}$$

where, Z_0 is the acoustic impedance of the medium ($Z_0 \approx 1.5\times10^6$ kg/m^2/s for water). Based on this equation, I_{SPPA} was 3.2 W/cm^2. The mechanical index (MI) is a figure of merit that describes the acoustic force of the US [17]. This value increases as the pressure increases and decreases with frequency. In this research, MI was 0.078.

IV. Discussion

To our knowledge, in-vivo experiments that uses an acoustic frequency of 15 MHz to stimulate a neuron has not yet been conducted. Furthermore, it is not clear at which intensity or amplitude is required to stimulate a nerve at this frequency. Nonetheless, G. F. Li et al. stimulated a mouse brain at 5 MHz with an intensity of 210 mW/cm^2 [18] and M. Menz et al. stimulated the retinal ganglion cell of a salamander at 43 MHz with an intensity of 20 W/cm^2 [10]. Extrapolating from these results it is expected that an intensity of several W/cm^2 will be required at 15 MHz. Thus, the intensity from this research (3.2 W/cm^2) will likely to be sufficient. This must be verified with additional in-vivo experiments.

Considering the safety of US stimulation, the U.S. Food and Drug Administration (FDA) allows I_{SPPA} < 190 W/cm^2 for diagnostic US imaging [17]. This threshold intensity is relatively high and is higher than what was observed during our experiment. Meanwhile, the average intensity needs to be limited to 720 mW/cm^2; also defined by the FDA, to avoid temperature induced tissue damage. Both conditions can be met by using an US waveform with an appropriate duty cycle. Another mechanism that may cause damage is cavitation. Cavitation is a phenomenon when the US forms a gaseous

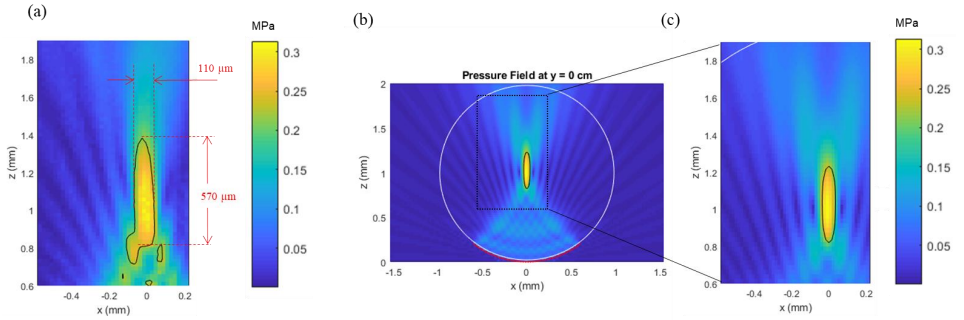

Figure3. Comparison of the experiment and the simulation. (a) The pressure profile measured using an optical fiber needle. (b) The simulation result of the pressure profile. The white line shows the contour of the vagus nerve (φ = 2 mm) and the black contour line represents the -3 dB level. The color bar shows the positive peak value of the pressure profile. The red dots represent the position of each CMUT element. (c) A close up image of (b) also corresponding to the same location in (a).

body within the tissue and then collapses, creating a shock wave that damages the surrounding tissues. FDA defines that the MI should be less than 1.9 to avoid this effect. The MI observed in this research was 0.078, which is much lower than the safety limit. For the safe application of US nerve stimulation, the amplitude and the intensity of the US that was observed in this research should not be dangerous.

Considering the encapsulation of the device, an US stimulator has a clear advantage over an electrical stimulator. An US stimulator can be entirely encapsulated with a coating, while an electrical stimulator have electrodes that need to be exposed to the body fluid. This creates a complex interface near the electrode that is prone to failure. However, this advantage for an US stimulator has a disadvantage that an US stimulator cannot record any electrical activity from the nerve. Therefore, these devices should complement each other.

Finally, we simplified a nerve by representing it with water. The sound velocity of a nerve is slightly higher than water so we can expect the focal area to become slightly larger. That being said, in reality the nerve will have capillary blood vessels, myelin sheath and other structures which will create multiple boundaries with different acoustic properties, hence, overall a more complex response is expected. This will be investigated in the next step.

ACKNOWLEDGMENT

The authors acknowledge the contribution of researchers working at Philips Research such as S. Shulepov and P. Dirksen for their precious input on CMUTs and the simulation result. This project is funded by ULIMPIA. ULIMPIA is labelled as a PENTA project endorsed by EUREKA under PENTA cluster number E!9911.

REFERENCES

[1] R. L. Johnson and C. G. Wilson, “A review of vagus nerve stimulation as a therapeutic intervention,” *J. Inflamm. Res.*, pp. 203–213, 2018.

[2] G. M. De Ferrari *et al.*, “Chronic vagus nerve stimulation : a new and promising therapeutic approach for chronic heart failure,” *Eur. Heart J.*, pp. 847–855, 2011.

[3] F. A. Koopman *et al.*, “Autonomic Dysfunction Precedes Development of Rheumatoid Arthritis: A Prospective Cohort Study,” *EBioMedicine*, vol. 6, pp. 231–237, 2016.

[4] M. Dali *et al.*, “Model based optimal multipolar stimulation without a priori knowledge of nerve structure: Application to vagus nerve stimulation,” *J. Neural Eng.*, vol. 15, no. 4, 2018.

[5] W. Jensen *et al.*, “Transverse Intrafascicular Multichannel Electrode (TIME) System for Treatment of Phantom Limb Pain in Amputees,” *ISEK’10 XVIII Congr. Int. Soc. Electrophysiol. Kinesiol.*, pp. 4–7, 2010.

[6] S. C. M. A. Ordelman, L. Kornet, R. Cornelussen, H. P. J. Buschman, and P. H. Veltink, “Selectivity for specific cardiovascular effects of vagal nerve stimulation with a multi-contact electrode cuff,” *IEEE Trans. Neural Syst. Rehabil. Eng.*, vol. 21, no. 1, pp. 32–36, 2013.

[7] H. E. Newton, “The Effect of high frequency Sound Waves on Heart Muscle and other irritable tissues,” *Am. J. Physiol.*, vol. 91, p. 284, 1929.

[8] W. J. Tyler, S. W. Lani, and G. M. Hwang, “Ultrasonic modulation of neural circuit activity,” *Curr. Opin. Neurobiol.*, vol. 50, pp. 222–231, 2018.

[9] A. Bystritsky *et al.*, “A review of low-intensity focused ultrasound pulsation,” *Brain Stimul.*, vol. 4, no. 3, pp. 125–136, 2011.

[10] M. D. Menz, O. Oralkan, P. T. Khuri-Yakub, and S. A. Baccus, “Precise Neural Stimulation in the Retina Using Focused Ultrasound,” *J. Neurosci.*, vol. 33, no. 10, pp. 4550–4560, 2013.

[11] M. Pekař, W. U. Dittmer, N. Mihajlović, G. van Soest, and N. de Jong, “Frequency Tuning of Collapse-Mode Capacitive Micromachined Ultrasonic Transducer,” *Ultrasonics*, vol. 74, pp. 144–152, 2017.

[12] B. Mimoun, V. Henneken, A. Van Der Horst, and R. Dekker, “Flex-to-rigid (F2R): A generic platform for the fabrication and assembly of flexible sensors for minimally invasive instruments,” *IEEE Sens. J.*, vol. 13, no. 10, pp. 3873–3882, 2013.

[13] “INCITE project, funded by ENIAC joint undertaking under grant number 621278-2.” .

[14] R. J. McGough, “Rapid calculations of time-harmonic nearfield pressures produced by rectangular pistons.,” *J. Acoust. Soc. Am.*, vol. 115, no. 5 Pt 1, pp. 1934–41, 2004.

[15] D. Chen, J. F. Kelly, and R. J. McGough, “A fast near-field method for calculations of time-harmonic and transient pressures produced by triangular pistons.,” *J. Acoust. Soc. Am.*, vol. 120, pp. 2450–2459, 2006.

[16] “FOCUS | Michigan State University.” [Online]. Available: https://www.egr.msu.edu/~fultras-web/index.php. [Accessed: 02-Oct-2018].

[17] H. Baek, K. J. Pahk, and H. Kim, “A review of low-intensity focused ultrasound for neuromodulation,” *Biomed. Eng. Lett.*, vol. 7, no. 2, pp. 135–142, 2017.

[18] G. F. Li *et al.*, “Improved Anatomical Specificity of Non-invasive Neuro-stimulation by High Frequency (5 MHz) Ultrasound,” *Sci. Rep.*, vol. 6, no. April, pp. 1–11, 2016.

Schlieren visualization of focused ultrasound beam steering for spatially specific stimulation of the vagus nerve

S. Kawasaki, E. Dijkema, M. Saccher, V. Giagka, J.J.H.B. Schleipen and R. Dekker

Abstract— **In the bioelectronic medicine field, vagus nerve stimulation (VNS) is a promising technique that is expected to treat numerous inflammatory conditions, in addition to the currently FDA approved treatment for epilepsy, depression and obesity [1]. However, current VNS techniques are still limited in the spatial resolution that they can achieve, which limits its therapeutic effect and induces side effects such as coughing, headache and throat pain.**

In our prior work, we presented a curved ultrasound (US) transducer array with a diameter of 2 mm and with 112 miniature US transducer elements, small enough to be wrapped around the vagus nerve for precise ultrasound nerve stimulation [2]**. Due to the curved alignment of the US transducers with 48 of the elements simultaneously excited, the emitted US was naturally focused at the center of the curvature. Building on this work, we employ a beam steering technique to move the focal spot to arbitrary locations within the focal plane of the transducer array. The beam steering was controlled through an in-house built US driver system and was visualized using a pulsed laser schlieren system. The propagation of the US pulse in water was imaged and recorded. This method was found to be a rapid and effective means of visualizing the US propagation.**

I. Introduction

Vagus nerve is the tenth cranial nerve and has projections to many of the visceral organs. It serves as a bidirectional link between the brain and the body. Currently FDA approved vagus nerve stimulators are used to treat depression, epilepsy, cluster headache and obesity. Recent developments in the bioelectronic medicine field have shown that vagus nerve stimulation (VNS) is also effective in treating inflammatory related diseases such as rheumatoid arthritis, and inflammatory bowel disease by decreasing the production of pro-inflammatory cytokines such as TNFα [1]. However, VNS suffers from side effects such as coughing, headache and throat pain due to its off-target stimulation. Thus, a stimulation technique with higher specificity is needed [3].

From a device fabrication perspective, researchers have worked on cuff electrodes with multiple channels to accurately localize the electrical current to achieve higher specificity [4]. However, this remains to be a challenge since the thicker myelinated A fibers tend to be stimulated an order of magnitude more easily than the thinner unmyelinated C fibers. To further increase the stimulation specificity, A. Ghazavi et al. created 20 µm wide shank-structures which have multiple electrodes on the surface that can be pierced into the nerve to provide localized electrical stimulation [5]. Although this was successful in rodent models, it is still an open question whether such an invasive technique can be safely used for human vagus nerve stimulation in the long run.

By taking into account the anatomy of the vagus nerve, some researchers stimulated the vagus nerve at locations near the end organ where it is expected that the off-target effect can be reduced [6]. Unfortunately, at these deeper locations the implantation of devices is more difficult due to its limited space and lack of suitable anchor points. For a less invasive approach, V. Cotero et al. used ultrasound (US) stimulation to achieve stimulation of these nerves near the end organ. In their work, they applied transcutaneous low intensity US (290.4 mW/cm^2) at the vagus nerve innervation within the spleen and modulated the anti-inflammatory pathway [7]. Furthermore, they showed that it is possible to achieve selectivity by stimulating the vagus nerve innervation within the liver to modulate the hepatic pathway. However, the direct consequence of stimulating the vagus nerve near the end organ, either electrically or ultrasonically, is that the simultaneous access to other vagus nerve branches becomes limited. For example, in case of electrical stimulators targeting different nerves, multiple implants are required, and for US stimulation, the US transducer outside of the body must be manually repositioned each time the targeted nerve is changed. Therefore, there is still a competing interest to keep the stimulus at the cervical level where all the nerve fibers are accessible.

In our prior work, we presented a highly miniaturized US cuff device [2]. This US cuff device is made of an array of 112 MEMS US transducer elements that is curved into a 2 mm diameter half cylinder. The acoustic frequency was 15 MHz to achieve high spatial resolution, and the US cuff was able to transmit a spatial peak average intensity (I_{SPPA}) of 3.2 W/cm^2. We hypothesized that such a device wrapped around the cervical vagus nerve can stimulate it at the neuronal to fascicular level.

In this paper, we demonstrate the US beam steering by using a custom-built 32-channel US driver system. For verifying the US field, an optical setup called the pulsed laser schlieren system was built to visualize the US propagation [8]. Schlieren optics is a useful tool to visualize the change in the refractive index in a transparent medium upon US propagation. This schlieren imaging technology has found a variety of applications for ballistics, air flows and acoustic waves visualizations, and this is the first time it is used in the US neuromodulation field. The advantage of using schlieren techniques in comparison to a hydrophone is that the US field

*Research supported by ULIMPIA and Moore4Medical.

S. Kawasaki, E. Dijkema, M. Saccher and V. Giagka are with the Microelectronics Department, Delft University of Technology, Delft, The Netherlands (corresponding author e-mail: shinnosuke.kawasaki@philips.com). V. Giagka is also with Fraunhofer Institute for Reliability and Microintegration IZM, Berlin, Germany. J.J.H.B. Schleipen and R. Dekker are with Philips Research, Eindhoven.

can be imaged simultaneously along with the US cuff device. Furthermore, the US field will not be altered by the hydrophone tip. Finally, it may allow opportunities to combine fluorescent imaging of action potentials with simultaneous US imaging.

II. Materials and Methods

In this work, a Capacitive Micromachined Ultrasonic Transducer (CMUT) was used to generate the US. The CMUT device is a capacitor cell which consists of two circular flat electrodes separated by a vacuum gap. One of the electrodes is a fixed bottom membrane on a silicon substrate and the other electrode is a movable top membrane that is facing the medium. By applying an AC voltage at US frequencies, the electrical field actuates the top membrane and US is transmitted into the medium. The CMUT devices used in this research have a diameter of 25 µm, and 24 CMUT devices were connected in parallel to form a single line which will be referred to as a CMUT element. Figure 1 shows the US cuff assembled on a PCB. The US cuff has 112 CMUT elements aligned in a 2 mm diameter half circle. The CMUT elements are connected to the bondpad via aluminum interconnects encapsulated in polyimide. The bondpad region is connected to a PCB via wirebonding.

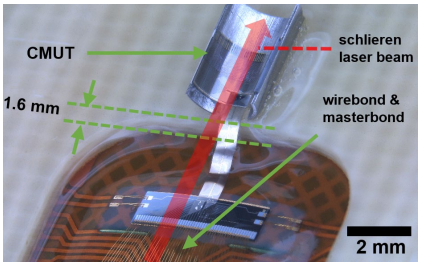

Fig. 1. CMUT sample that was used for the experiment. In order to have a clear optical path through the US field, the position of the bond pad was designed to be 1.6 mm lower than the position of the CMUT. This kept the added height of the wirebond and the masterbond to be slightly lower than the CMUT array.

A. Pulsed laser Schlieren System

Figure 2 shows the pulsed laser schlieren system. The light of a red laser diode (SANYO DL-6147-240) is focused onto a 20 µm diameter pinhole using a microscope lens for spatial filtering and subsequent aberration reduction. The diverging laser beam is collimated using a collimating lens with a focal length of 200 mm. Next, the parallel beam travels through the water tank, after which it is focused by a 200 mm focusing lens onto a 10 µm diameter chromium mirror, blocking the main non-aberrated laser beam. Therefore, in the initial state, the camera (uEYE), that is positioned behind the mirrorstop, will capture a pitch-black image. The combination of a camera objective lens and laser focusing lens provides a sharp image of the plane of US propagation onto the camera image sensor.

When a CMUT array is positioned within the water tank, the US field results in a modulation of the refractive index of water and diffracts part of the light to go beyond the obstructing mirror, which will subsequently be captured by the camera. An US signal with an acoustic frequency of 14.3 MHz was generated in bursts of 15 cycles at a pulse repetition frequency of 3 kHz. For each generated US burst, a waveform generator (Agilent 3295A) was triggered to generate a 100 ns pulse to drive the laser diode. The delay time between the US burst and the laser pulse was incrementally increased from 0 µs to 3.35 µs in 100 ns steps. Due to the stroboscopic effect, the camera visualizes the US as slowly moving waves through the water. The US and laser/imaging setup have been synchronized and controlled using Labview software. During the actual measurements the ambient room light was turned off.

To focus the US to a certain point within the curvature, beam steering was used. The appropriate time delay for each element was calculated as follows. The coordinate where we would like to focus is defined as **x**. The distance from each transducer element to the **x** is D_i :

$$D_i = |\mathbf{x} - \mathbf{q_i}|, \qquad i \in [1, 32]$$

where, $\mathbf{q_i}$ is the coordinate of the individual 32 US transducer elements. The time delay (T_i) applied to each element is given by,

$$T_i = \frac{D_i - \min(D_i)}{v}, \qquad i \in [1, 32]$$

where, v is the speed of US in water. The calculated value is rounded to an integer multiple of 5 ns, which is the resolution of the US driver system. The US driver used for this work was an in-house built US driver system that is based on the HV7351 chips (Microchips).

B. Simulation with FOCUS

The experiment was simulated with the Fast Object-Oriented C++ US Simulator (FOCUS) [9]. In this simulation, 32 rectangular US transducer elements with a width of 25 µm and a length of 0.65 mm were arranged in a curved array like the experiment. The medium used for the simulation was water with a sound velocity of 1500 m/s. The US frequency was 14.3 MHz, the number of cycles was 15, and the velocity at which the US element vibrates was set to 1 m/s. The US field was simulated using frequency domain simulation assuming continuous wave of US with a phase delay. The intensity of the US field was given by, $I = P^2/Z_0$ where, I is the intensity of the US field, P is the acoustic pressure and Z_0

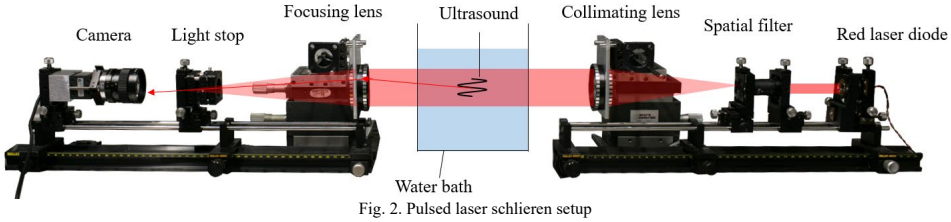

Fig. 2. Pulsed laser schlieren setup

is the characteristic acoustic impedance of water which is 1.5 MRayl. All simulation results were normalized by dividing the US intensity by the maximum intensity within the same figure.

C. *Hydrophone measurement*

A fiber optic hydrophone (Precision Acoustics) was used to measure the US field. The tip of the hydrophone was scanned horizontally for 1.6 mm and vertically for 1 mm from the focal point. In total, 2091 measurements were taken for obtaining a single US field profile. Since each measurement at a certain coordinate took 6 seconds, the total time it took for obtaining a single image was 3.5 hours. The amplitude of the US signal used to drive the transducer elements had 35 V DC bias voltage and an additional 25 V amplitude square wave at 14.3 MHz.

III. Result

Figure 3 shows several raw images obtained from the camera. The semi-circular shape (red bold line) is where the US cuff was positioned. The triangular shadow on both sides of the US cuff is the epoxy that was used to glue the US cuff to the PCB. The 32 CMUT elements that were actively driven are circled with a dotted line. In the figure the US propagates upwards focusing in the center of the US cuff. When the active US elements were located near the center of the US cuff (top row in figure 3), the US field focused in an elongated shape with two prominent sidelobes. Meanwhile, when the active elements were located near the edge of the US cuff (bottom row in figure 3), the US field showed a clear interference pattern. In this case, the distance between two neighboring high intensity peaks at the center was measured to be 66 µm. This is nearly half the US wavelength of 52 µm, in correspondence with what is expected for an interfering wave. The small increase is due to the fact the US signals are slightly tilted upwards.

The advantage of using the schlieren method is the fast image acquisition speed. To demonstrate this, the focus location was varied to 100 locations and a video was taken sequentially one after another without any pause[1]. The total duration to take the video was only 5 minutes. It is possible to see that the video was taken in real time because particles floating in the liquid are moving continuously throughout the video.

In figure 4, a single frame from the schlieren image at 2.01 µs was converted to a heat map and was compared to the US field measured with a hydrophone. In the schlieren image to ignore excess noise floor, the normalized intensity beneath 0.7 was removed. In both the schlieren image and the hydrophone measurement we see that the intensity of the left sidelobe is slightly higher than the intensity of the right sidelobe. This is due to the imperfect alignment of the transducers array during the assembly process. Even with this rough image quality the similarity between the hydrophone measurement and the US visualization confirms that schlieren imaging can be successfully used for fast US visualization.

To improve the image quality, another video was taken with 34 ns time intervals between each image. The increased number of frames helped to decrease the noise from dust particles. A background subtraction technique was used to remove the static parts of the image, such as scratches, and shadows from the glue and the US cuff. Next, the intensity profile of the US field was extracted by integrating it over the entire US propagation. Figure 5 shows the result of the simulation on the left and the integrated schlieren image on the right. In order to facilitate the comparison between these images, the images were cropped to the same size and aspect ratio. In all images the US cuff is represented by a white line. Clearly the direction of the US matches very well the simulated results. We also see that as the US focus is further from the US transducers, the US lobe size increases which is consistent with the simulation result.

The peak negative acoustic pressure measured at the center of the focus was 1.7 MPa. The spatial peak temporal average intensity that could currently be achieved with the US driver system was 6.5 W/cm^2 with 90 kHz pulse repetition frequency and 15 cycles per each burst. The mechanical index was 1.4 which is lower than the limit defined for US imaging applications by the FDA (<1.9). At the moment, we believe that this intensity should be sufficient to stimulate the nerve according to prior work [7]. However, it is still not clear since the higher acoustic frequency will likely have a higher stimulation threshold levels to stimulate the neurons.

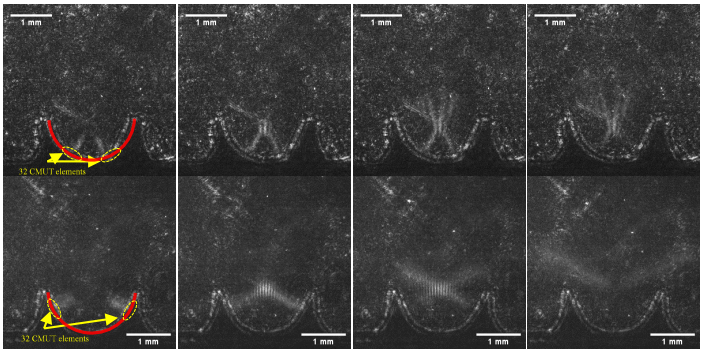

Fig. 3. Snap shots of the US schlieren movie from left to right with the 32 US elements near the center (top row) and 32 US transducers near the edge (bottom row)

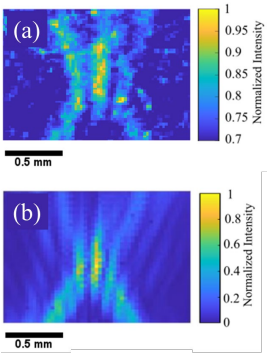

Fig. 4. (a) Schlieren image intensity profile and (b) hydrophone measured intensity profile

[1] URL link to beam steering videos: https://doi.org/10.34894/Y4FILA

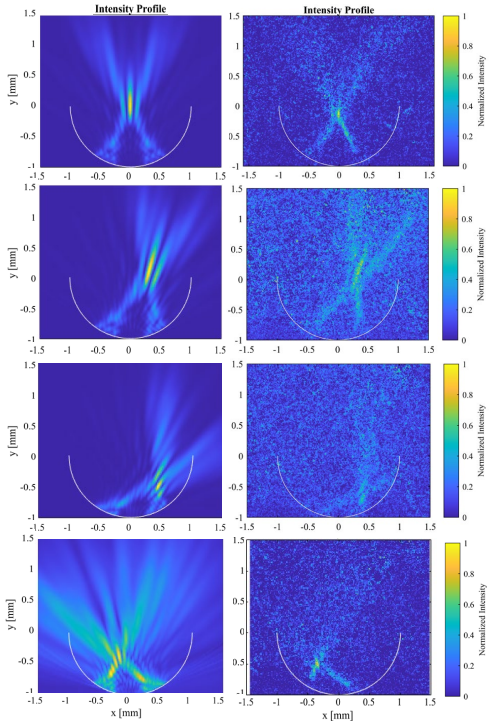

Fig. 5. US field comparison between simulation (left) and schlieren (right)

IV. Discussion and Conclusion

In this work, beam steering of the ultrasonic field produced by an US cuff was demonstrated using the pulsed laser schlieren setup. Schlieren imaging allowed faster US visualization (few minutes) compared to hydrophone measurement (few hours). In addition, once the system is up and running it took less time to observe the US field even compared to simulating it with FOCUS where it took tens of seconds to simulate a single frame with enough resolution.

However, schlieren imaging does not produce an absolute measurement of the US field, so it should be used as a complementary technique to hydrophone measurements. Yet it is possible to calibrate the system for a limited range of pressures [10]. For calibration, the key parameters that need to be determined are the exposure time, the pulse repetition frequency and the laser intensity. Although a wide range of US intensity could be visualized, the dynamic range for a specifically calibrated range, spans to only one order of magnitude as shown in the linear scale used in Figure 4 and 5. Finally, due to the optics that it requires, it would not be feasible to integrate this technology for in-vivo experiments. Meanwhile, experiment which are done in an ex-vivo setup may allow for the schlieren setup to be integrated.

In conclusion, further miniaturized US transducers with varying size and shapes will be available in the future. This will increase the complexity of the ultrasound field that will be used for US neuromodulation. Thus, visualizing the relative intensity of the US field with a schlieren setup would give an intuitive feedback to check if the US system is working properly. This would clarify a lot of the ambiguity within the works that are done in US neuromodulation and greatly facilitate the research in this field.

Acknowledgment

The authors acknowledge the contribution of researchers working at Philips research for their fabrication of the CMUTs. This project is funded by the ULIMPIA and Moore4Medical projects. ULIMPIA is labelled as a Penta Project Endorsed by Eureka under Penta cluster number E!9911 References. Moore4Medical receives funding from the ECSEL JU, under grant agreement H2020-ECSEL-2019-IA-876190.

References

[1] C. M. Noller, Y. A. Levine, T. M. Urakov, and J. P. Aronson, “Vagus Nerve Stimulation in Rodent Models : An Overview of Technical Considerations,” vol. 13, no. September, pp. 1–11, 2019, doi: 10.3389/fnins.2019.00911.

[2] S. Kawasaki *et al.*, “Pressure measurement of geometrically curved ultrasound transducer array for spatially specific stimulation of the vagus nerve,” *Int. IEEE/EMBS Conf. Neural Eng. NER*, vol. 2019-March, pp. 1239–1242, 2019, doi: 10.1109/NER.2019.8717064.

[3] V. Giagka and W. A. Serdijn, “Realizing flexible bioelectronic medicines for accessing the peripheral nerves – technology considerations,” *Bioelectron. Med.*, vol. 4, no. 1, pp. 1–10, 2018, doi: 10.1186/s42234-018-0010-y.

[4] M. Dali *et al.*, “Model based optimal multipolar stimulation without a priori knowledge of nerve structure: Application to vagus nerve stimulation,” *J. Neural Eng.*, vol. 15, no. 4, 2018, doi: 10.1088/1741-2552/aabeb9.

[5] M. I. Romero-ortega, A. Ghazavi, M. A. Gonz, and S. F. Cogan, “Intraneural ultramicroelectrode arrays for function-specific interfacing to the vagus nerve,” vol. 170, no. September, 2020.

[6] S. C. Payne *et al.*, “Anti-inflammatory effects of abdominal vagus nerve stimulation on experimental intestinal inflammation,” *Front. Neurosci.*, vol. 13, no. MAY, pp. 1–15, 2019, doi: 10.3389/fnins.2019.00418.

[7] V. Cotero *et al.*, “Noninvasive sub-organ ultrasound stimulation for targeted neuromodulation,” *Nat. Commun.*, no. 2019, pp. 1–12, doi: 10.1038/s41467-019-08750-9.

[8] T. Neumann and H. Ermert, “A New designed Schlieren System for the Visualization of Ultrasonic Pulsed Wave Fields with High Spatial and Temporal Resolution,” *2006 IEEE Ultrason. Symp.*, pp. 244–247, 2006, doi: 10.1109/ULTSYM.2006.74.

[9] D. Chen, J. F. Kelly, and R. J. McGough, “A fast near-field method for calculations of time-harmonic and transient pressures produced by triangular pistons,” *J. Acoust. Soc. Am.*, vol. 120, no. 5, pp. 2450–2459, 2006, doi: 10.1121/1.2356839.

[10] H. A and C. I. Zanelli, “Quantitative real-time pulsed schlieren imaging,” *Ultrason. Symp.*, pp. 1223–1228, 1991.

C

Ultrasound Hardware and Software

C.1. PZT

The PZT devices used in this work were immersion transducers ordered from Olympus. Four frequencies (1 MHz (V303-SU-F0.6IN-PTF), 5 MHz(V310=N-SU-F-0.45-IN-PTFImmTr), 10 MHz(V312-SU-F0.5IN-PTF) and 20 MHz(V317-SU-F0..50IN-PTF)) were used which all had a focal distance of 15 mm. These PZT devices are typically more robust than CMUTs and were used as a backup in case the CMUT did not work. These devices were driven using an RF amplifier controlled by a signal generator.

C.2. 32 CHANNEL ULTRASOUND DRIVER

The 32 channel ultrasound drier is an in-house built ultrasound driver system. They have been built based on the HV7351 chips (Microchip). It can generate a phase-controlled ultrasound signal with a 5 ns resolution. Fig. C.1 is the circuit diagram to drive a single CMUT element in the WUP system. To drive the CMUT, a MOSFET is connected to either the Vpos, Vneg or GND. For a simplified representation, the MOSFET is replaced with a switch in the figure. By alternating between one of the three states, a voltage is applied to the CMUT. A current limiting resistor of 32 Ω is used to deal with unwanted short circuits and a decoupling capacitor of 47 nF is used to block the bias voltage. Since CMUTs require a bias voltage, this can either be supplied to the CMUT via a 1 MΩ resistor through

the WUP system or through an external connection. With this circuit, most of the power is consumed by the inverter's large gate capacitance that needs to be charged and discharged for switching on and off and thus this circuit it self is not so efficient but will be fine for this work.

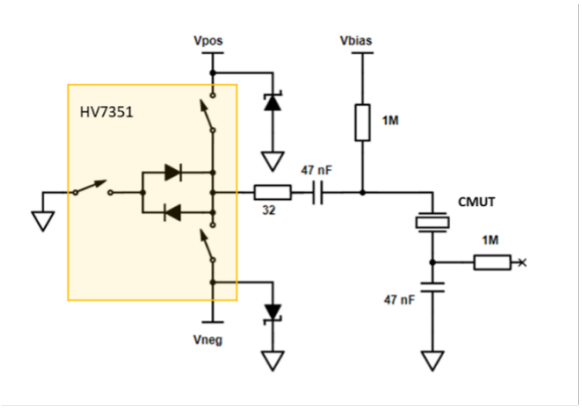

Figure C.1: WUP system circuit diagram for a single channel

A picture of the board from above is shown in Fig. C.2. The main functionality of the board is highlighted and is indicated with an arrow. The teensy 3.6 microcontroller is used to define the ultrasound parameters; ultrasound frequency, phase delay, polarity, amplitude, bias voltage, cycle number, burst rate, triggering condition(external or internal). If the trigger is set to external, the SMA connector to the left of the board can be used as the trigger signal input. The positive and negative rail voltage and the bias voltage is generated on this board through the buck boost converter circuitry at the bottom left of the figure. The internally generated voltage is available at the box header connector as Vpos internal, Vneg internal, and Vbias internal. The voltage then can be connected to four US driver chips on the right of the figure by shunting some pins on the box header using a shunt pin. Thus, this allows full control of the ultrasound parameters. However, later it was found that the buck boost converter creates considerable ripple noise that can be detected in the electrical recording setup. Therefore, this internal voltage generator was usually turned off and an external voltage was used for the experiment which had a much lower ripple. Finally, since the flexible CMUTs used for the experiment has 48 independently controllable ultrasound transducer elements if the output pressure is not sufficient with 32-channels, two WUP systems could be connected in parallel by triggering both boards through the external trigger signal (dual WUP board).

there is a hard limit on the maximum frequency that could be generated determined

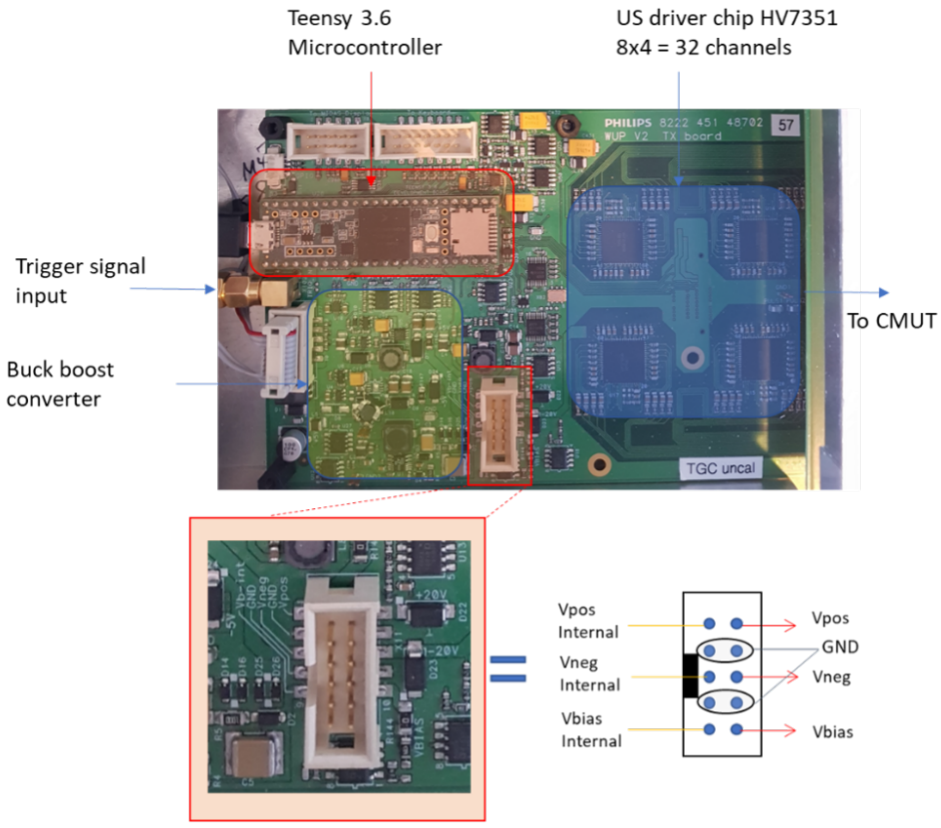

Figure C.2: WUP board seen from above.

by the cable length from the ultrasound transducer to the transmitter chip. A rough calculation can be made as follows. Assuming that a typical CMUT element has a capacitance of about 80 pF, and the track inductance is 1 µH/m (typical for a coax), the resonance frequency between the track inductance of 30 cm (nominal length of the PCB tracks) and the CMUT will be,

$$f_{res} = \frac{1}{2\pi\sqrt{80\,\text{pF}\cdot 1\,\mu\text{H/m}\cdot 30\,\text{cm}}} = 32\,\text{MHz} \tag{C.1}$$

This implies that the cable and the CMUT will resonate at this frequency. In reality, the applied signal will begin to see overshoot and considerable ringing could be seen already at 15 MHz Ideally an ASIC should be assembled close enough to the CMUT so that the effect of cable inductance could be neglected. However, this was not possible for the scope of this work for two reason. First there was no suitable ASIC to drive the

CMUT and second the ultrasound driver kit does not allow higher frequencies than 15 MHz.

C.3. SOFTWARE

Fig. C.3 is a screenshot of the developed GUI. The three peripheral components could be controlled through this interface which are the ultrasound stimulator, the electrical stimulator and the recording setup. The GUI was all created using the python tkinter package[1]. On the upper left panel is where the system parameters are defined. This includes basic information such as where and which CMUT, WUP board, PZT is being used. To the right of this panel is the mode selection. In this section the setup could choose between 5 different modes; 1) ultrasound stimulation with PZT, 2) ultrasound stimulation with CMUT, 3) simultaneous electrical and PZT ultrasound stimulation 4) simultaneous electrical and CMUT ultrasound stimulation 5) electrical stimulation. The bottom part is divided to the control of the CMUT ultrasound parameter on the left side and the control of the electrical stimulation parameter on the right top and and the control of the PZT ultrasound stimulation on the right bottom side. The bar graph beneath it shows the delays which are applied to the 48 elements and the red color and the yellow color identifies which WUP board is used to drive each elements. Since it is important to know what the acoustic pressure is being outputted, a calibration curve is taken for each tranducer and is referred to when the appropriate transducer is selected from the GUI interface. Finally, after each stimulation a pop up window (see Fig. C.4) shows up asking the users comment about how the stimulation went.

There are two ways of interacting with the software, either by clicking through the desired parameters manually using the controller bar, or by defining preset stimulation patterns and by running through each parameter automatically during the experiment. The latter is preferred because it provides the possibility of evaluating a broader range of parameters in different combinations without the interference of the human. Moreover, for the experiments where excised nerves are used, these have to be conducted during a limited amount of time, during which the viability of the nerve is still present. Therefore, it was preferred to think of a list of parameters before the experiment.

[1] Lundh, F. (1999). An introduction to tkinter. URL: Www. Pythonware. Com/Library/Tkinter/Introduction/Index. Htm.

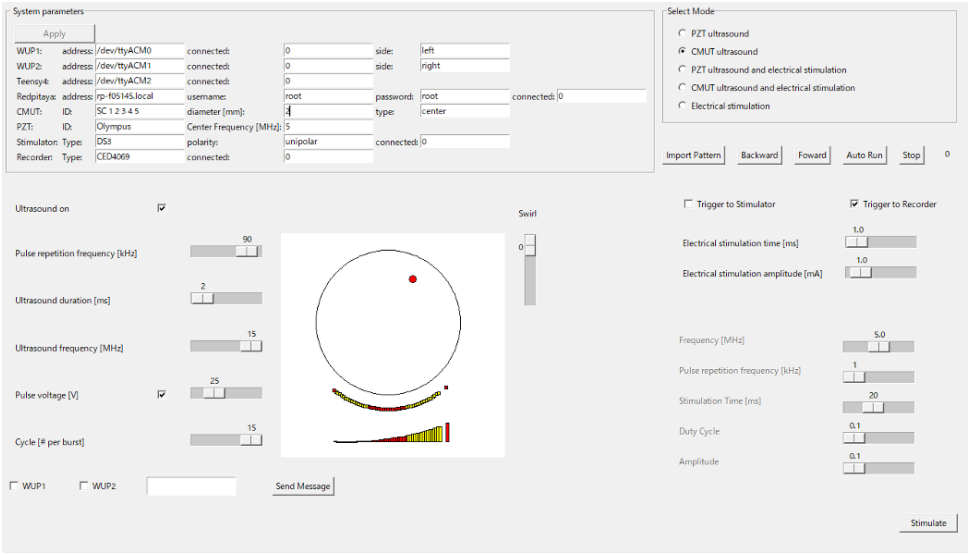

Figure C.3: GUI for controlling the ultrasound and electrical stimulator.

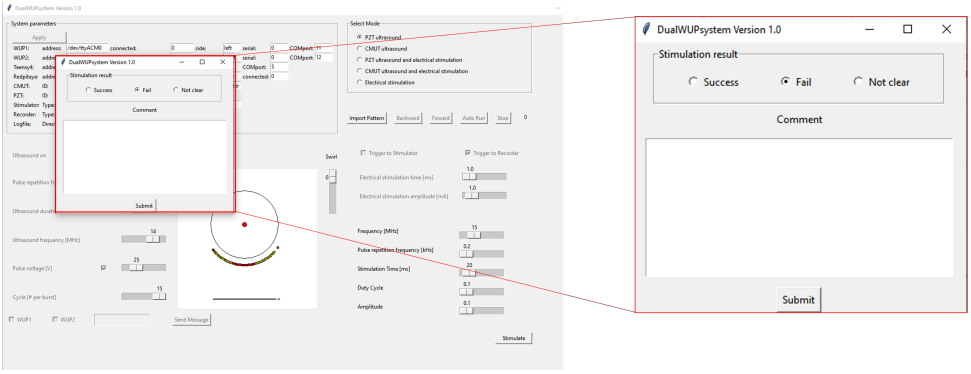

Figure C.4: Pop up screen to ask for additional input for each stimulation.

CURRICULUM VITÆ

31-03-1993 Born in Kanagawa, Japan.

EDUCATION

2011–2016 Undergraduate in Electrical Engineering
Tokyo Institute of Technology

2016–2017 Masters in Microelectronics
Delft University of Technology

2018 – 2022 PhD. Electrical Engineering
Delft University of Technology
Guest researcher at Philips

Thesis: Revitalizing CMUT
Promotor: Prof. dr. ir. Ronald Dekker

2022 – Wearable ultrasound researcher
TNO Holst Center

List of Publications

8. **S. Kawasaki**, J. Yeh, M. Saccher, J. Li, and R. Dekker, Bulk acoustic wave based mocrfluidic particle sorting with Capacitive Micromachined Ultrasonic transducers," 2022IEEE MEMS (WPTC), 2021, submission accepted.

7. **S. Kawasaki**, I. Subramaniam, M. Saccher and R. Dekker, "A microwatt telemetry protocol for targeting deep implants," 2021 IEEE International Ultrasonics Symposium (IUS), 2021, pp. 1-4, doi: 10.1109/IUS52206.2021.9593603.

6. M. Saccher, **S. Kawasaki** and R. Dekker, "The long-term reliability of pre-charged CMUTs for the powering of deep implanted devices," 2021 IEEE International Ultrasonics Symposium (IUS), 2021, pp. 1-4, doi: 10.1109/IUS52206.2021.9593683.

5. M. Saccher,**S. Kawasaki**, M. Proietti Onori, G. van Woerden, V. Giagka, R. Dekker "Focused Ultrasound Neuromodulation On A Multiwell MEA," 2021 Bioelectronic Medicine, doi: 10.21203/rs.3.rs-1023856/v1

4. **S. Kawasaki**, Y. Westhoek, I. Subramaniam, M. Saccher and R. Dekker, "Pre-charged collapse-mode capacitive micromachined ultrasonic transducer (CMUT) for broadband ultrasound power transfer," 2021 IEEE Wireless Power Transfer Conference (WPTC), 2021, pp. 1-4, doi: 10.1109/WPTC51349.2021.9458104.

3. **S. Kawasaki**, E. Dijkema, M. Saccher, V. Giagka, J. J. H. B. Schleipen and R. Dekker, "Schlieren visualization of focused ultrasound beam steering for spatially specific stimulation of the vagus nerve," 2021 10th International IEEE/EMBS Conference on Neural Engineering (NER), 2021, pp. 1113-1116, doi: 10.1109/NER49283.2021.9441225.

2. **S. Kawasaki** et al., "Pressure measurement of geometrically curved ultrasound transducer array for spatially specific stimulation of the vagus nerve," 2019 9th International IEEE/EMBS Conference on Neural Engineering (NER), 2019, pp. 1239-1242, doi: 10.1109/NER.2019.8717064.

1. R. Suganuma, **S. Kawasaki** and K. Yasuoka, "Disinfection by HO2 Radicals Generated by Negative Corona Discharge on Acidic Solution," in IEEE Transactions on Plasma Science, vol. 47, no. 1, pp. 346-349, Jan. 2019, doi: 10.1109/TPS.2018.2879384.